FAKULTÄT FÜR ELEKTROTECHNIK UND INFORMATIONSTECHNIK
Faculty of Electrical Engineering and Information Technology

Local stress measurement of thin films with wafer-level integrated test structures

DIPLOMA THESIS

submitted in partial fulfilment of the requirements for the degree of

Diplom-Ingenieur

in

Embedded Systems

by

Horia Andor
Registration Number 01346350

to the Faculty of Electrical Engineering and Information Technology

at the TU Wien

Advisor: Univ.Prof. Dipl.-Phys. Dr.rer.nat. Ulrich Schmid
Second advisor: Associate Prof. Dipl.-Phys. Dr.techn. Michael Schneider

Vienna, 20th March, 2024

Horia Andor	Ulrich Schmid

Technische Universität Wien
A-1040 Wien ▪ Karlsplatz 13 ▪ Tel. +43-1-58801-0 ▪ www.tuwien.ac.at

Erklärung zur Verfassung der Arbeit

Horia Andor
Burggasse 107, 1070 Wien

Hiermit erkläre ich, dass ich diese Arbeit selbständig verfasst habe, dass ich die verwendeten Quellen und Hilfsmittel vollständig angegeben habe und dass ich die Stellen der Arbeit – einschließlich Tabellen, Karten und Abbildungen –, die anderen Werken oder dem Internet im Wortlaut oder dem Sinn nach entnommen sind, auf jeden Fall unter Angabe der Quelle als Entlehnung kenntlich gemacht habe.

Wien, 20. März 2024

Horia Andor

Acknowledgements

I would like to express a sense of thanks and gratitude to all the persons who had guided, helped, and encouraged me through the course of this project.

Foremost, I would like to express my gratitude to my two supervisors, Mr. Univ.Prof. Dipl.-Phys. Dr.rer.nat. Ulrich Schmid and Mr. Associate Prof. Dipl.-Phys. Dr.techn. Michael Schneider. Thank you for allowing me to be part of your research group and giving me professional support. I am extremely thankful to Mr. Associate Prof. Dipl.-Phys. Dr.techn. Michael Schneider for his willingness to help, expertise, guidance, and flexibility.

I would like to thank Patrick Meyer for his support, patience, and insightful details regarding the fabrication process of the designed rotating arm test structures.

As ever, I am indebted to my family for providing unconditional support and a loving environment throughout my entire study.

I would like to thank Ali, Boro, Aleksandar, Sonja, Radu, Matei, Ibo, Said, David, Amer, Furkan, Logo, and Maruan for learning camaraderie during my Bachelor studies. Further, a huge "thank you" to Berni, Jasmina, Mohammed, Aleksei, and Masa for learning camaraderie during my Master's studies.

Lastly, I owe my deepest gratitude to Carmen. I thank her for her unconditional support, enormous empathy, and love.

Abstract

Residual stress remains in a material or structure after manufacturing and processing in the absence of external forces or temperature difference. Further, these residual stresses are one of the most common bottlenecks in the case of the fabrication of novel microelectromechanical systems (MEMS). As stress characterisation techniques utilised at the macroscale are not suitable for measuring the local stress on MEMS devices, various MEMS-applicable alternatives have been researched in recent years. The goal of this work was to find such an alternative with an optical detection scheme. First, a brief overview of the macroscale stress measurement techniques is followed by a comprehensive overview of the existing MEMS residual stress characterisation approaches. Next, an adapted version of the rotating arm test structure described in the first chapter was simulated in COMSOL Multiphysics to find the best design for achieving the targeted measurement range: from -1 GPa to 1 GPa. The optimised design parameters served as the basis for the lithography mask designs presented in the third chapter of this diploma thesis. These designs include measures implemented to reduce the out-of-plane deflection and to ensure easy readability of the measurement results, as well as a successful fabrication of the test structure. Moreover, the detailed dimensions of both a smaller and a larger rotating arm test structure are included, followed by a brief description of their fabrication process. To check if the fabricated rotating arm test structure fulfils its purpose successfully, several a-SiC:H, Pt and AlN, and Cr thin films with different mechanical stress levels and thicknesses were deposited by using PECVD, sputtering, and evaporation, respectively, on top of the rotating arm test structures. The verification measurements confirmed that both larger rotating arm test structures covered with 375 nm thick, PECVD-deposited a-SiC:H thin films function correctly but only reach 57 and 60 % of the simulated displacement. These values are significantly smaller than the 95.9 % reached by the best-performing rotating arm test structure presented in this diploma thesis: the larger device rotated by 45°, coated with a 250 nm thick, evaporated Cr thin film. On the other side, out-of-plane deflection is still observable for this best-performing test structure. Reducing this out-of-plane deflection may be achieved by depositing the stressed thin films only on specific parts of the rotating arm test structure and an increase of the measured vs expected x-displacement ratio may be achieved by making several design adjustments on the central part of the fabricated rotating arm test structure. Thus, further research is needed to verify if the proposed improvement measures will be able to lead to a better-performing rotating arm test structure design.

Contents

CHAPTER 1

Introduction

Stress components that remain in a material or structure after manufacturing and processing, in the absence of external forces or temperature difference, are called residual stresses [1]. In the case of fabrication of novel microelectromechanical systems (MEMS), which requires the integration/stacking of distinctly different materials, these residual stress are one of the most common issues, causing undesired static mechanical deflections and changes in mechanical key parameters such as resonance frequency shifts [2].
Due to the mechanical nature of MEMS devices, their performance, reliability as well as long-term performance may be significantly reduced by these residual stresses [1][2]. As enhanced performance and reduced failures would be the consequence of a better understanding and control of film stress, an accurate stress analysis is of particular importance [3][4]. Such an analysis could help identify whether the fabricated microstructures will meet the design expectations by investigating the local distribution and evolution of residual stress [5][4].
Therefore, various techniques of localised stress assessment for MEMS thin film materials were being researched in recent years, as new methods must be developed, due to the fact that many well-established residual stress characterisation techniques utilized at macroscale cannot be applied [4][1].
As the negative effect of residual stresses is even more pronounced in the case of MEMS devices made out of piezoelectric materials due to the stacking of several layers for transducer realisation, the estimation and minimisation of residual stress are vital to assess the functioning of such modern-day piezoelectric MEMS devices [4][2].

1.1 Types of residual stresses and their causes

As different reasons may lead to the formation of residual stress, a simple way to categorise the different types of residual stresses is after their nature, into intrinsic and extrinsic stresses [2]. For the extrinsic stresses, thermally generated residual stress will follow,

while the three types of intrinsic stresses to be further described in this work are general intrinsic stress, lattice mismatch stress, and plastically induced stress [2].

1.1.1 Extrinsic stress

Nonuniform cooling or heating are the cause of **thermally generated residual stresses** on a macroscopic level, where large internal stresses and severe thermal gradients occur due to these thermal nonuniformities [2][1][3]. Further, the mismatch of thermal expansion coefficients (CTE) between different MEMS constituents (two adjoining materials, for example a film and a substrate) are the main cause on a microscopic level [2][1][3]. Thus, sample temperature changes taking place during processing and fabrication result in different thermal strains in the substrate and in the film [1][3]. For example, sputter deposition involves plasma exposure, which heats up the sample [3]. Further, the sample cools down after the growth is finished and the resulting change in temperature is capable of leading to large thermal stress [3]. Additional thermal stresses may be generated in the case of samples subjected to laser processing, as such fabrication processes cause phase transformations such as melting and resolidification [1].
The resulting thermal stress is proportional to the difference between the CTE of the substrate (α_s) and the one of the film (α_f), as well as to the change in temperature ΔT, and the biaxial modulus of the film M_f [3]:

$$\Delta\sigma_{thermal} = M_f\varepsilon = M_f(\alpha_s - \alpha_f)\Delta T$$

The main reason for this proportionality is the fact that a thin film is constrained to remain bonded to the much thicker substrate [3].
To sum up, thermally generated residual stress is predominantly biaxial, as it acts on the x-y plane of MEMS structures [2][3].

1.1.2 Intrinsic stress

1.1.2.1 Stress induced due to microstructure imperfections

The first main mechanism through which intrinsic residual stress is generated is the elastic deformation of grain boundaries [2]. This deformation occurs as a consequence of the imperfections in the microstructure and of the deviation of the lattice structure from its equilibrium state [2]. Further, such imperfections in the microstructure, like grain boundaries or boundaries between the columns voids (or point defects or dislocations in a crystalline lattice at atomic level), occur because of the impurities present on the depositing surface during the growth process and due to non-equilibrium growth conditions [2].
The main consequence of these stresses induced due to microstructure imperfections is the bending of the MEMS structure, as these stresses generally vary along with the thickness of the film [2]. Further, freestanding microstructures fabricated from the deposited film may warp, buckle up, or bend down, showing signs of mechanical instability if critical

values of internal stress are exceeded [6][7]. Such instability may lead to delamination or rupture of the deposited films [6][7].

1.1.2.2 Lattice parameter mismatch stress

As film layers and the substrate or underlayer, on which they are grown on, may have different lattice parameters, a strain could arise in the interface between the film and the substrate [2][3]. This strain leads to lattice parameter mismatch stress, but may also lead to stress relaxation through the generation of different types of defects (for example, cracks, dislocations, or voids) in the film [2].
The lattice mismatch Δ can be written as:

$$\Delta = \frac{\mid a_A - a_B \mid}{a_B}$$

where a_A is the lattice constant of the film (A), while a_B is the lattice constant of the substrate (B) [2]. This formula indicates that the condition for growing good-quality epitaxial films is not having a considerable mismatch of the film-substrate lattice constants [2]. Further, the critical thickness t_c represents the maximum allowed epitaxial layer thickness to which a film may be grown, without risking to introduce dislocations at the film-substrate interface and can be related to the lattice mismatch as follows [2]:

$$t_C \approx \frac{a_A}{2\Delta} \approx \frac{a_A^2}{2 \mid a_A - a_B \mid}$$

In consequence, due to the fact that stretching or buckling of the MEMS structure may arise due to large lattice mismatch stresses and piezoelectric materials are anisotropic, special attention should be payed in order to reach the desired fabrication quality [2].

1.1.2.3 Plastically induced stress

The main cause which lies behind plastically induced stress are the incompatibilities in plastic straining between constituent matrix and reinforcement materials of the composite, such as metal nanoparticles embedded in the polymer matrix or the ductile metal matrix embedded in the ceramic [2]. These incompatibilities result in the formation of shape misfit [2].
This kind of residual, intrinsic stress is most prominent in the multiphase-alloy or composite films [2].

According to [8], another way to categorise the residual stress is into compressive and tensile stress [8].

1.1.3 Compressive stress

Capillary forces, which act at early growth stages in the surface plane of small islands rigidly bonded to the substrate, are the usual trigger for the appearance of compressive stress [8]. An additional compressive stress-producing mechanism, present in the case of sputter-deposited films, is energetic particle bombardment during deposition process [8]. Further, the entrapment of impurity atoms of a size different from the growing crystal produces lattice distortion, which also causes compressive stress [8].
Compressive stress can lead to undesired buckling, bending of released micromachined structures or even delamination [3][9]. Further consequences of compressive stress are higher yield stress, lower fatigue resistance, and higher hardness in the affected material [2].

1.1.4 Tensile stress

Attractive forces at column boundaries in columnar films are one major cause of tensile stress [8]. Further, another mechanism capable of inducing tensile stress is the formation of a grain-boundary segment by neighboring islands [8]. Tensile stress generation may also be caused by phase transformations, annihilation of excess vacancies, or film densification resulting from grain growth [8].
The main consequences of too high tensile stresses are limited usable thickness of a layer, deformation, or even film cracking [2][8][3].

The last categorisation of residual stress presented in this work includes the following three origins of residual stress: thermal, mechanical and chemical [1]. While the residual stress with thermal origins was already described as a component of extrinsic stress, the mechanical component of residual stress is a result of the nonuniform plastic or elastic deformation, which may take place during the fabrication process [1].
On the other hand, volume changes associated with phase transformation, precipitation, chemical reactions, or oxidation may cause chemically generated stresses [1]. Further, the generation of substantial residual stress gradients in the surface layers of MEMS devices can be the consequence of chemical coatings and surface treatments [1].

1.2 Stress measurement methods on wafer level

The following subchapter includes an overview of some well established stress measurement methods, which are able to measure various parameters leading to the existing residual stress on wafer level.
It is important to note that residual stress is an intrinsic property and is not directly measurable [1]. Therefore, it must be deduced from other measurable properties, like force, deformation data, or strain, together with material parameters (Young's modulus, Poisson's ratio) and based on a specific model from theory of elasticity, mechanics of materials, or even photonics [1].

1.2.1 Wafer curvature

As a consequence of coating one type of material on different wafer substrates, residual stress may be generated, which may cause a change in the curvature of the wafer [2]. This bending induced by the stressed film will be measured during the wafer curvature measurement [3]. By using the Stoney equation, the residual stress σ resulted due to the deposition of a thin film can then be estimated as a function of the curvature of the wafer:

$$\sigma = \frac{E_{sub}}{1-\nu_{sub}} \frac{t_{sub}^2}{6t_{film}} \left(\frac{1}{R_1} - \frac{1}{R_0} \right)$$

where E_{sub} is the Young's modulus of the substrate and ν_{sub} its Poisson ratio, which both have to be known for the stress estimation [2]. Further, t_{sub} and t_{film} stand for the thickness of the substrate and of the film, respectively [2]. R_0 is the initial radius of curvature of the substrate (before the film deposition) and serves as a reference point, while R_1 is the radius of curvature of the substrate recorded after the deposition of the film [2]. This Stoney equation is valid only for the cases when the substrate is much thicker than the deposited film (thin-film regime) [2]. Further, if the deposited film is highly stressed or its stiffness cannot be neglected, the Stoney formula could result in significant errors [1].
Wafer curvature measurements can be performed easily in situ and in real-time, while also being nondestructive [3][8]. These characteristics enabled this method to gain popularity for quantifying residual stress in constrained, non-integrated structures, in particular thin films deposited on thick substrates [10]. This specific measurement, which is still dominating in industrial processes due to its relatively simple structure, has the major advantage of being able to measure the evolution of the curvature during the deposition of the film [1][3]. This ability can be used in order to determine the distribution of stress at different heights in the film, not just the average stress [3].
The curvature of the wafer can be measured either using methods without direct mechanical contact, like laser scanning, optical transmittance, reflectance, or X-ray reflectivity, or by using direct contact methods, like strain gauges or stylus profiler [2]. As next, laser scanning and multi beam optical stress system (MOSS) will be further described.

1.2.1.1 Laser scanning

In the case of laser scanning, the usual procedure used for calculating the stress is to measure the curvature of physical surface of the sample and then use continuum mechanics models for the transformation [11]. A setup of such a laser scanning device can be seen in the Figure 1.1.

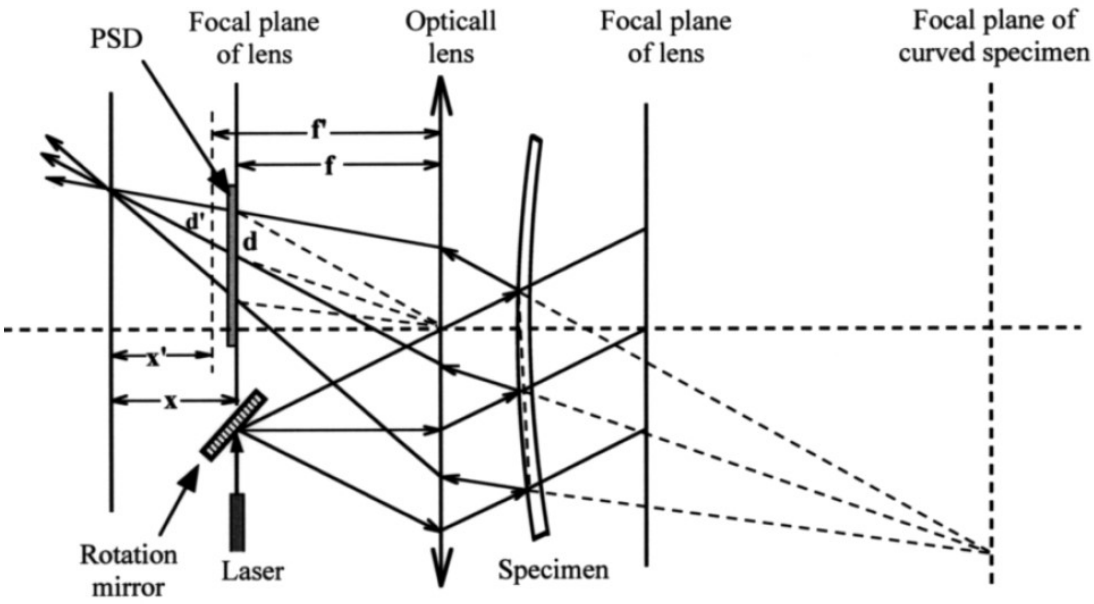

Figure 1.1: Functioning principle behind a laser scanning setup. From [11].

The depicted setup consists of a position sensitive detector (PSD), an optical lens with nominal focal length of 2000 mm, a micro-scanner driven by a galvanometer and a 0.5 mW laser generator [11]. Parallel beams, which scan perpendicularly over the specimen surface, are produced by the rotation of the rotation mirror, due to its placement at the focal plane of the optical lens [11]. In the case of a flat specimen, the reflected beams would be focused into a single point at the focal plane, as they would be parallel [11]. Thus, no deflection of the reflected beams would be sensed during the scanning by the PSD [11]. However, if the specimen has a radius of curvature R, the reflected beams can not be focused into a single point, as they are no longer parallel.
Some simple geometrical considerations lead to the following equation for the curvature of the physical surface of the sample k:

$$k = \frac{1}{R} = \frac{d}{2Df}$$

where d is the displacement distance of the reflected beam on the PSD, D is the scanning

distance on specimen, and f is the focal length of the optical lens [11].

1.2.1.2 Multi beam optical stress system (MOSS)

The next optical method may be successfully used for in situ measurements in growth chambers, where a large amount of mechanical vibration is induced by the vacuum pumps [8]. The reason for this reduced sensitivity to sample vibrations is its working principle: in this case, not the absolute position of the beam, but the spacing between the different reflected beams is used to determine the curvature of the sample [3][8]. Thus, the direction of the reflected beams may be changed by sample vibrations or motion, but by the same amount for all of them [8]. Therefore, the relative spacing between the beams remains unaltered and the overall resolution is not limited by the mechanical stability of the sample during the measurement [8][3]. A setup of such a MOSS device can be seen in the Figure 1.2.

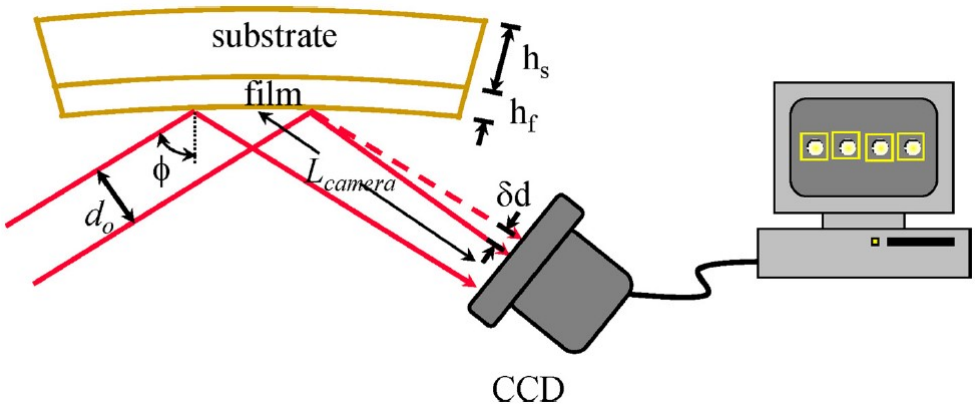

Figure 1.2: Schematic of multi beam optical stress system (MOSS). From [3].

First, an array of parallel laser beams directed towards the sample surface is created by using an optical element [3]. A CCD camera is used to measure the spacing between the reflected beams, while a frame grabber is used for digitizing [3]. In order to achieve small spot sizes with a spacing on the order of several mm, the lens focuses the beams on the detector [3].
Further, the following equation shows the relationship between the change in sample curvature κ and the change in beam spacing δd :

$$\kappa = \kappa_0 + \frac{\delta d}{d_0} \frac{cos(\phi)}{2L_{camera}}$$

where κ_0 is the initial curvature in the sample, d_0 is the initial spacing of the beam reflections, ϕ is the angle between the sample normal and the incident beam, while L_{camera} is the distance from the camera to the sample [3].

1.2.1.3 Capacitive measuring methods

With this measuring method, the change in capacitance, induced by changing the spacing between a fixed reference electrode and the sample, is measured [12]. Although this approach has high sensitivity, it assumes that the sample does not drift from his position or vibrate, actions which may lead to a capacitance change [12]. Thus, such capacitive measuring methods may be inaccurate in the presence of significant amount of mechanical noise [12].

1.2.2 X-ray diffraction (XRD)

Like the wafer curvature stress measurement method, X-ray diffraction enables a fine tuning and control of the stress level, as part of the design of functional coatings and novel nanostructured materials [8]. Thus, the durability of such coatings and materials will be extended, while their performance will be enhanced [8]. On the other side, this stress measurement method cannot measure residual stress in amorphous materials [2]. Due to grain boundaries or different defects induced by the deposition process itself, strain and stress fields are most often inhomogeneous [13]
By using XRD methods, the lattice deformation in different crystallographic directions is measured [13]. Then, by applying a constitutive equation in the form of the generalised Hooke's law and provided that the single-crystal elastic constants of the materials are known, the residual stress can be calculated from the measured x-ray elastic strains, ϵ, which can be written as follows [13][8][2]:

$$\epsilon = \frac{d_{(hkl)} - d_{0(hkl)}}{d_{0(hkl)}}$$

In this formula, $d_{0(hkl)}$ and $d_{(hkl)}$ represent the d-spacing of the (hkl) plane under no strain and strain conditions, respectively [2].
Some traditional theoretical X-ray diffraction methods are the $sin^2\Psi$ one, as well as the grazing incidence X-ray diffraction geometry (GIXRD) [11]. Further, the double crystal diffraction topography (DCDT) will be also described.
The $sin^2\Psi$ *method* is the most common procedure [8] and implies that X-rays with wavelength λ are irradiated onto the sample at different incident angles [14]. In this way, the slope M of the diffraction angle to $sin^2\Psi$ can be obtained and the residual stress σ can be written as:

$$\sigma = KM$$

where Ψ is the angle between the normal of the diffractive crystal surface and the normal of the sample surface, while K is the stress constant [14]. In addition to this formula, the relationship between the interplanar spacing d and the diffraction angles 2φ is included in the following Bragg equation:

$$2dsin\varphi = n\lambda$$

with the order of the reflection n [14].

In order to overcome the difficulties faced by XRD stress analysis in thin layers, GIXRD has evolved as an alternative measuring method [13]. The depth to which diffraction information is collected is realised by employing angles of the incident and diffracted x-ray beam with respect to the top sample surface close to the critical angle for total external reflection [8]. The following equation can be stated for the residual stress in the case of GIXRD measurements:

$$\sigma_R = \frac{E_{sub}}{(1+\nu)sin^2\Psi}\frac{d_{(hkl)} - d_{0(hkl)}}{d_{0(hkl)}}$$

where ν is the Poisons ratio, and E_{sub} is the Young's modulus of the thin-film material [2].

1.2.2.1 Double crystal diffraction topography (DCDT)

In the case of XRD, the usual procedure used for calculating the stress is to measure the curvature of crystal lattice planes and then use continuum mechanics models for the transformation [11]. A setup of a double crystal diffraction topography device can be seen in the Figure 1.3.

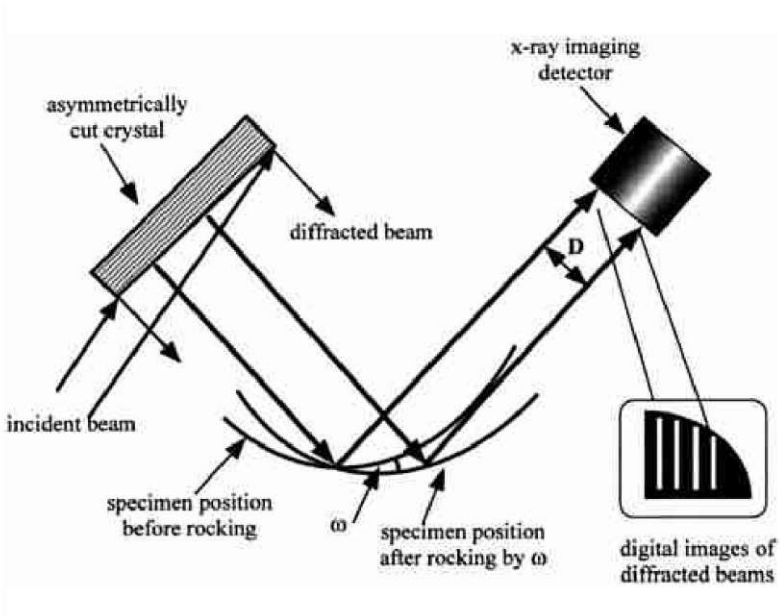

Figure 1.3: Functioning principle of curvature measurement by DCDT. From [11].

Starting from the left side, the depicted setup consists of an asymmetrically cut Si single crystal, with (4 0 0) as the reflection plane and cut such that its {1 0 0} lattice planes form a 33.2° with the crystal surface [11]. In order to enable the occurrence of the diffraction, the X-ray incident beam must form a grazing incidence angle, as the Bragg angle for Si (4 0 0) is 34.58° for Cu Kα [11]. Thus, a magnification factor $m = 39$ is obtained, where m is defined as the ratio between the width of the diffracted beam to that of the incident beam [11]. As next, the specimen, a coated Si (1 0 0) single crystal wafer, is entirely illuminated by the large diffracted cross-sectional beam and serves as a second crystal [11]. The Bragg condition is satisfied only at a narrow region of the specimen, when the lattice planes in the wafer have a radius of curvature R [11]. Thus, the diffraction condition is satisfied by the single vertical band (1st exposure) on the detector from the region, which is produced by the diffracted X-ray beam [11]. Further, a second vertical band corresponding to the 2nd exposure occurs as a result of the shift of the specimens region meeting the Bragg condition, caused by the rocking of the specimen by an angle ω [11].
Some simple geometrical considerations lead to the following equation for the lattice plane curvature k:

$$k = \frac{1}{R} = \frac{\omega sin(\theta)}{D}$$

where θ is the Bragg angle of the (4 0 0) reflection (34.58° for the Cu Kα radiation), D is the spacing of two vertical bands on the X-ray imaging detector, and Rω is the separation of the two bands where Bragg reflection occurs, before and after rocking [11]. In comparison with the laser scanning technique, double crystal diffraction topography is the better choice for measuring extremely small curvature changes for ultra-thin films [11]. The reason for this is the fact that it can be difficult to position the laser beam to exactly the same region of a specimen before and after deposition, especially if the substrate curvature of the specimen has large nonuniformities [11]. On the other hand, DCDT has other limitations: it can only be used for films deposited onto single crystal substrates, since it measures lattice curvature [11]. In such situations, which occur often in the case of protective coatings, the laser scanning technique can be readily applied [11].

1.2.3 Ultrasonic techniques

Ultrasonic techniques is another popular category of non-destructive methods used to measure the residual stress in MEMS structures [2]. It uses the fact that the propagation velocity of an ultrasonic wave in an isotropic elastic body is affected by the stress and its magnitude [14]. Therefore, it basically measures the residual stress-induced change in ultrasonic acoustic wave velocity in the material or structure [2]. Thus, the relationship between the acoustic velocity of the ultrasonic wave V_r and the residual stress σ_r can be used to measure the residual stress [14] as follows:

$$V_r = V_0 + K_{ae}\sigma_r$$

where V_0 is the acoustic velocity of the material not affected by residual stress, while K_{ae} is the acousto-elastic constant of the material [2].
The acousto-elastic constant has a strong dependence on the microstructural inhomogenities and anisotropic nature of materials, which makes it quite complicated to isolate the effect of multiaxial stress [2]. Despite this disadvantage, this method is able to provide information about macro-stresses over large areas of the material during MEMS fabrication, being at the same portable, cheap, and quick [2].

1.3 External stress measurement methods on wafer regions

1.3.1 Raman spectroscopy

The next presented method used to measure material parameters which lead to the residual stress, Raman spectroscopy, relies upon the inelastic scattering of photons due to the interaction with the phonons, molecule vibrations, or any other excitation in the material under test [2]. Beside its ability to yield information about the materials mechanical strain, it can also deliver data about crystal orientation and structure, electron-phonon interaction, or the impurity content [1].
In micro-Raman spectroscopy (μRS), a monochromatic radiation, for example a laser light, is focused on the tested sample to a spot size of ~ 1 μm by using a microscope [1]. As next, the scattered photon due to inelastic scattering is recorded in a spectrometer, serving as the Raman signal [2]. The intensity of the Raman signal is measured as a function of frequency by the spectrometer [1].
First, a reference spectrum is measured by recording the signal for the sample without stress or strain [2][1]. If the sample is placed in a stressed state, it exhibits a shift in frequency in the Raman spectrum with respect to the reference spectrum:

$$\Delta\omega = \frac{1}{\lambda_i} - \frac{1}{\lambda_s}$$

where λ_i and λ_s are the wavelengths of the incident and scattered radiation, respectively [1]. $\Delta\omega$ however is the Raman shift and has usually cm^{-1} as a measurement unit [1].
Further, the value of the local uniaxial stress can be determined from the change in the Raman shift [1]. The spot size of the monochromatic radiation determines the locality of the measurement [1]. Moreover, if the Raman shift is interpreted as a wavenumber shift, the tensile and compressive stresses may be identified in the following way: while the compressive stress induce a shift towards the higher wavenumber, the tensile stress yields a shift towards lower wavenumber [2].
In conclusion, Raman spectroscopy has proven to be a suitable nondestructive method for measuring nonuniform residual stresses in microstructures [14]. On the other side, it

is less sensitive to amorphous material and the Raman frequency shift can be affected by external factors, like laser thermal effects or focusing depth [2][14].

1.3.2 Ion Beam Layer Removal (ILR)

The following Ion Beam Layer Removal method (see Figure 1.4) is based on the standard Euler-Bernoulli beam theory, used for calculating deflection characteristics and load-carrying of beams [5]. Thus, ILR leads only indirectly to the residual stress, as the deflection of a cantilever is the consequence of the existence of residual stress inside the film [5]. Beside the residual stress, the deflection of the cantilever also depends on the Young's modulus of the involved materials, the momentum of inertia of the cantilever, as well as the film- and substrate thickness [5].
The Ion Beam Layer Removal method works as further described: a FIB workstation is used to fabricate a cantilever, which is initially fixed on both sides, out of the initial system, in the vicinity of the sample edge [5]. As next, the material, which is supporting the cantilever on one side, is removed [5]. Depending on the distribution of residual stress in the system, this action leads to a positive or negative deflection [5]. A scanning electron microscope is used to measure the first deflection at the free end of the cantilever (deflection area) [5]. The film thickness is gradually reduced in the rear part of the cantilever (ILR area) over a width of 10 - 15 μm, in order to determine the stress distribution across the coating [5]. Further, the measurement of the deflection changes during FIB milling are done by the rest of the cantilever, which remains unaltered and acts as a pointer [5]. Next, the stiffness of the system is reduced as a side effect of the gradual thinning of the cantilever, while the stress distribution is also affected [5]. Both of these side effects lead to a change in deflection, which is measured at the tip of the cantilever for every milling step [5]. The actual deflection, the dimensions of the cantilever, and the elastic properties of the system are the parameters which lead to the mean stress value from each removed layer [5]. Finally, by using the Euler-Bernoulli beam theory, together with the thicknesses of the sublayers as well as the measured deflections, the residual stresses in the sublayers are consequently determined.

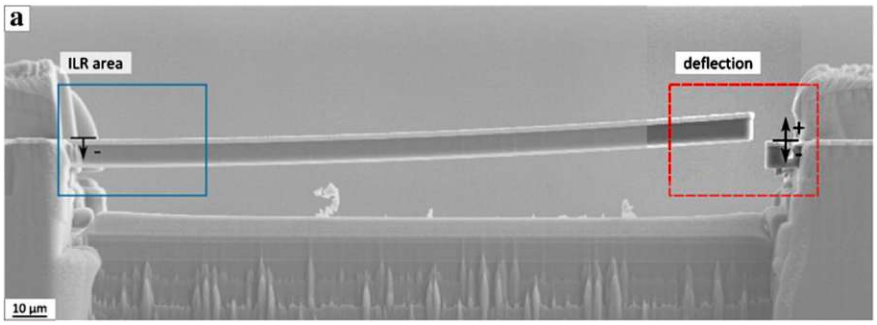

Figure 1.4: SEM image of a cantilever, which bends upwards due to the effect of the tensile residual stress. The red dashed square indicates the deflection area and the blue square indicates the ILR area. From [5].

1.3.3 Nanointendation

Nanointendation is a simple method, which is traditionally used to determine mechanical properties of materials, like toughness, fracture strength, micro hardness, or Young's modulus [2][1]. This measurement technique implies that an indentation tip of defined shape shape, like Berkovitch, Vickers, spherical, or cone types, is indented into the structure to be measured [2][1]. This interaction between the tip and the structure results in a F-h curve, where h, the depth of the penetration, is plotted as a function of the applied load, F [2]. The aforementioned mechanical properties can be extracted from the F-h plot, which is also altered by the presence of residual stress in the material as further described: if tensile residual stress is present in the material, the magnitude of shear stress is enhanced, which in turn enhances the indentation plasticity [2]. Therefore, a lower load is required to indent same depth, while the shape of the loading curve in F–h plot moves downward and exhibits a lower slope [2].
The other way round, if there is any compressive residual stress in the material, the unloading curve shifts towards the left [2]. Moreover, the compressive residual stress yields more elastic recovery, while the tensile one induces less elastic recovery, as the unloading process of the nanoindentation technique is purely elastic [2].
The contact between the tip and the structure to be measured results in another way of determining the level of residual stress in the material: through the examination of the shape of the pileup occurring at the edge of the contact circle [1]. Are there any deviations in shape to be observed, information about the level and sign of residual stress of the structure can be obtained [1]. Although the hardness or the Young's modulus of materials are not very affected by residual stress, the contact area between tip and the structure is very sensitive to residual stress [14]. Therefore, this method is able to provide information about the residual stress in localised areas of the wafer [2].

1.4 On-wafer stress indicators

For the past two decades, there has been a major research activity regarding novel MEMS structures, which enable the measurement of residual stress on wafer level [1]. Thus, there has been a rapid growth of such MEMS residual stress characterisation devices [1]. As next, some of them will be briefly presented.

1.4.1 Micromachining technique

Usually, test structures fabricated by micromachining technique used for residual stress measurement are released after removing the underlying sacrificial layer [10]. As a consequence of residual stress, the structure will increase or decrease its dimensions [10]. This deformation of the structure leads to the residual stress [10].

1.4.1.1 In-plane

1.4.1.1.1 Pointers Pointers are in-plane test structures that amplify small displacements induced by residual stress, by making use of geometric effects [10]. A linear relationship between the deflection of the pointer and in-plane stress can be observed for such structures [9].
The stress value deduced from the pointer structures is independent of the film thickness, in contrast to the buckling structures [9]. Further, no anti-sticking procedure are needed for pointers, as they may only stick in their relaxed position, in contrast to buckling structures, where sticking can develop into a critical issue [9]. In addition to the already presented advantages, such pointers structures can be successfully used for the whole stress range according to [9]. Only in the case of very high stress values, the geometric differences between the fabricated and the simulated structure may become important and hence cause significant deviations to the stress values determined by the wafer curvature technique [9]. Further, a possible problem for such high stress gradients may be the upward deflection of the indicator tips, which could hinder the readout of the indicator structure. On the other side, the Young's modulus is the main uncertainty in the case of low stress values [9].

A **rotating arm test structure**, as depicted in Figure 1.5, is composed of two layers deposited on a substrate [4]. The first layer is a sacrificial one, while the second one is the thin film under investigation [4]. The test structure [10] consists of two fixed parallel arms, marked with L_f, which have an offset h between them and play the role of test beams, and a freestanding rotating indicator beam marked as L_r [4][10]. The amplification effect of such a measurement structure can be enhanced by either increasing the length of the rotating indicator beam or by decreasing h [10]. One end of each test beam is connected to the rotating indicator beam, while the other one is anchored to the substrate [10]. After the sacrificial layer is removed, the test beams are no longer bound to the substrate and are therefore free to contract or elongate to relieve any residual stress, thus creating a rotating deflection of the indicator beam [15][10]. The direction of this deflection leads to the type of residual stress: in the case of tensile residual stress, the

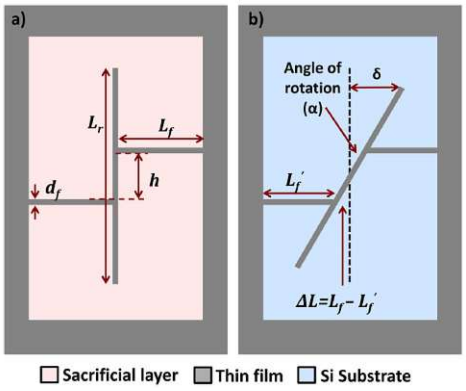

Figure 1.5: Schematic of a rotating arm test structure: a)before and b)after removing the sacrificial layer. Here, the situation of a thin film under tensile stress is depicted. From [4].

two parallel arms shorten and induce a clockwise rotation of the indicator beam, while in the case of compressive residual stress, a counterclockwise rotation of the indicator beams occurs due to the lengthening of the test beams [2][10][4]. This rotation of the rotating indicator beam leads to the residual stress in the test beams [4]. Starting with Hooke's law:

$$\sigma = E\epsilon$$

where E is the Young's modulus of the thin film and ϵ is the strain in the test beams, which can be further expressed as:

$$\epsilon = \frac{\Delta L}{L_f}$$

with ΔL the change in length of test beams, which is equal to:

$$\Delta L = \frac{h + d_f}{2} tan(\alpha)$$

where d_f is the width of the initially fixed parallel arms and α the angle of rotation of the indicator beam [4]. Finally, the angular displacement of the indicator beam δ is also represented in Figure 1.5 and is equal to [4]:

$$\delta = \frac{L_r}{2}\alpha$$

The deflection of the indicator beam can be read by using a vernier scale attached to the substrate at the end of the indicator and inspecting it with an optical microscope or

scanning electron microscopy (SEM) [10][9]. Further, if the strain over the entire surface has to be mapped, several structures have to be built on the wafer and their angle of rotation must be optically extracted [15]. This procedure can be done automatically by using a camera together with a software that is able to recognize the pattern of rotating beams and analyse their rotation angles [4].
In conclusion, this practical semi-automated wafer mapping technique is preferred to buckling-type devices as such in-plane strains can be easier detected and quantified optically [15]. However, the Young's modulus needed for calculating the residual stress is dependent on the deposition and related process conditions for thin films used in MEMS technologies [15].
An improvement of the rotating arm test structure is the **double indicator test structure** as shown in Figure 1.6. By using two symmetrical structures, it can increase the sensitivity of the measurement [10]. Further advantages of this structure are the elimination of technology variations and under-etching, while the double deflection can be measured [10].

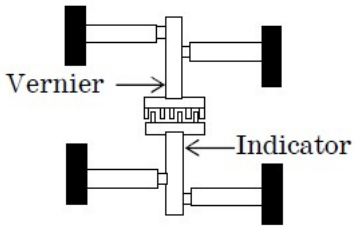

Figure 1.6: Schematic of a double indicator test structure. From [10].

1.4.1.1.2 Bent-beams Another test structure which takes advantage of geometric layout to amplify in-plane displacements induced by residual stress is the bent-beams test structure shown in Figure 1.7 [10]. These test structures are symmetric with respect to the x- and y-plane [7]. Further, they can measure tensile and compressive residual stress, indicating tension by an increase in the distance between the indicators and compression by a decrease, respectively [10].

The annotations from Figure 1.7 have the following meaning: M_a is the moment acting about the anchor located at the anchor, θ is the angle between the x-axis and the arm before its release, L_a is the actual length of the arm or half the overall device length, M is the moment in the arm at any position x, L_p is the projected length of the arm onto the x-axis, and F is the force required to deform the arm at point B [7]. Further, Δy is the displacement of the apex of the structure and is used to determine the residual in-plane stress of the film [7]. The test structure presented in [7] has a Vernier gauge attached to the center of the beam. The residual stress σ can be expressed as :

$$\sigma = E\frac{\Delta L}{x} + \frac{F}{wh}$$

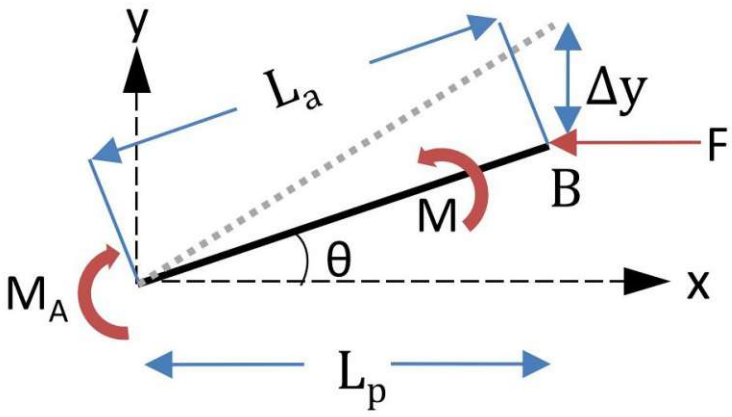

Figure 1.7: Free body diagram of a half of a bent beam and the forces acting on it. From [7].

where E is the Young's modulus, while w and h are the width and the height of the beam, respectively [7]. Further, ΔL is the change of length difference between the actual beam and its projected length on x-axis due to force F and is equal to [7]:

$$\Delta L = (L_a(0) - L_p(0)) - (L_a(F) - L_p(F))$$

In conclusion, bent beams allow for rapid and non-contacting measurements [10].

1.4.1.2 Out of plane: Buckling technique

The basic principle of the stress measurement by buckling technique is the extension or contraction of the released structure caused by stress in thin films [10].

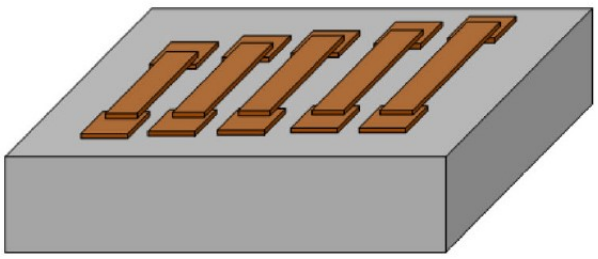

Figure 1.8: Schematic of an array of microbridges/fixed-fixed beams. From [2].

1.4.1.2.1 Microbridges/Fixed-fixed beams In this case, the typical device used is a micro bridge or fixed-fixed beam, which buckles after release and can only measure

compressive stress [10]. By using critical buckled bridge dimensions, the compressive stress σ can be expressed as:

$$\sigma = \frac{E}{1-\nu}\frac{\pi^2 h^2}{3L^2}$$

where E is the Young's modulus, ν is the Poisson's ratio, h is the thickness of the bridge while L is the length of the critical buckled bridge [10].
According to [9], the whole stress region from high tensile to high compressive stress may be covered with acceptable resolution by using a minimum of four different indicator geometries.

1.4.1.2.2 Microrings The following two test structures use also the buckling technique, but are also capable of detecting tensile residual stress [10].

Guckel rings, as depicted in Figure 1.9, are test structures, which can be used to

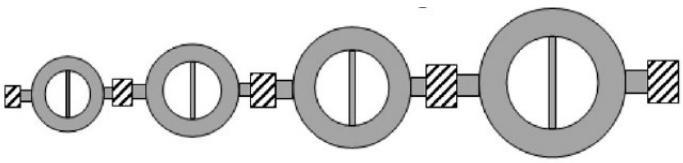

Figure 1.9: Schematic of an array of Guckel rings. From [2].

measure tensile stress only [10]. Under tensile stress, the ring of such a Guckel ring deforms to an oval after the freestanding structure is released [10]. This buckling process takes place only if the internal residual stress exceeds their corresponding specific critical value [1]. Further, the central beam of the structure becomes compressive [10]. Values of residual stress σ can be derived from the maximum displacement of the central beam of a Guckel ring as it follows:

$$\sigma = \frac{E}{1-\nu}\frac{0.515h^2}{R_c^2}$$

where E is the Young's modulus, ν is the Poisson's ratio, h is the film thickness, while R_c is the critical buckel radius [16].

As next, such a **diamond ring** test structure (see Figure 1.10) is able to measure both compressive and tensile stress, while still using the buckling technique [10]. First, the sacrificial layer has to be removed in order to enable either the middle beam to buckle, in the case of tensile residual stress, or the outside beams, in the case of compressive residual stress [10]. The mechanism behind can be described as follows: first, the tensile stress in the layer is converted into compressive stress in the middle beam by the diagonal beams, while the compressive stress is increased in the outside beams [10].
The goal of such test structures is to characterize the in situ residual stress generated

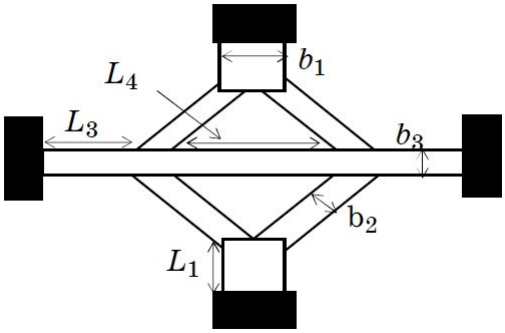

Figure 1.10: Schematic of a diamond ring. From [10].

during the entire fabrication process [1]. Unfortunately, only large stress values could be evaluated under an optical microscope, as the deflection must be greater than 10 μm [1][9]. Even in such cases it was difficult to distinguish between unbuckled and buckled beams, as the determined values were still generally too low [9]. In order to enhance this resolution, the number of beams has to be increased while their dimensions varied, which requires considerable wafer space [1][17]. Further, another reason for which such an array of test structures with systematically varied geometry parameters is needed is the fact that a single test structure is only capable to provide information whether the residual stress exceeds the critical stress or not [2][1]. The last disadvantage of such buckling test structures is given by their sensitivity to the boundary condition, which may affect the accurate determination of the strain [17].

1.4.2 Strain gauges

The reason for the fabrication of such on-wafer micro-machined strain gauges is the need to gauge more accurate values of residual stress, which originates from the MEMS device fabrication [2]. Further, such strain gauges are suitable for measuring planar biaxial stresses, as deflections could be observed in the x-y plane [2].

1.4.2.1 Micro strain gauge

The test structure depicted in Figure 1.11 is a mechanical micro strain gauge, which can be fabricated in situ with active devices [18]. Moreover, it is able to determine both tensile and compressive strain under optical microscopes with a resolution of 0.0001 % [18]. In this case, a single structure is used, which implies a significant reduction of the required wafer area in comparison to the fixed-fixed beams [1].
Such a mechanical micro strain gauge consists of three beams: a tip beam with the length L_{tb}, a slope beam with the length L_{sb}, and an indicator beam with the length L_{ib} [10]. The tip beam elongates, in the case of compressive residual strain, or shrinks, in the case of tensile residual strain, after the device is released in the sacrificial etch step [1][18]. Further, the movement of the tip beam is transferred to the slope beam and a maximum

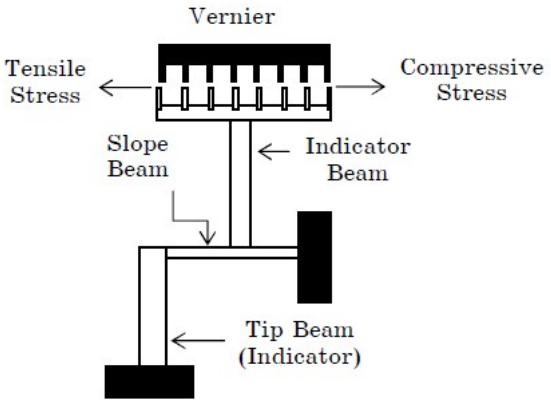

Figure 1.11: Micro strain gauge schematic. From [10].

is created at the tip beam side of the slope beam, which only produces a tiny rotation at the center of the slope beam, since its other end is a fixed anchor [18]. The indicator beam is placed at the center of the slope beam and magnifies this tiny rotation at the center of the slope beam [18]. Thus, a large displacement δ is generated at the Vernier side of the indicator beam, which enables the reading of the compressive or tensile strain under an optical microscope [18]. The residual stress σ is calculated by :

$$\sigma = \frac{2}{3}\frac{E}{1-\nu}\frac{L_{sb}}{L_{ib}L_{tb}}\delta$$

where E is the Young's modulus and ν is the Poisson's ratio [10]. Finally, such a micro strain gauge is resistant to out-of-plane gradients, while its accuracy profits from the independence of the micro strain gauge output of both the thickness of the microstructure cross-section and the thickness of the deposited thin film [18][1].

1.4.2.2 Long-short beam strain sensor

The next presented test structure is another variation of a strain sensor, which can measure both compressive and tensile stress: the long-short beam strain sensor [2][17]. As depicted in Figure 1.12, it consists of two cantilever test beams with different lengths, a short and a long test beam, connected by a short tip beam as an indicator [2][10]. Further, the two test beams will contract or extend due to the residual stress in the thin films, after the release of the freestanding part [10]. Thus, a deflection δ of the two test beams is caused by their difference with respect to contraction or elongation [17]. This deflection is magnified by the short tip beam used as an indicator and can be read out by using the vernier gauge attached at the free end of the indicator beam together with an optical microscope [17][10]. In this case, the residual stress σ can be expressed as:

$$\sigma = \frac{E}{1-\nu}\gamma\delta$$

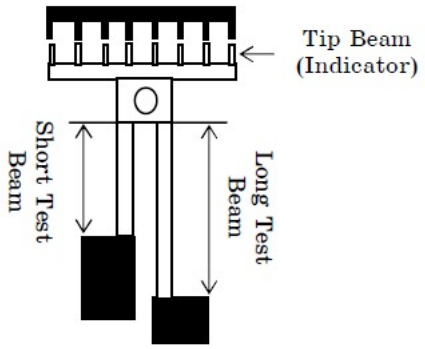

Figure 1.12: Schematic of a long-short beam strain sensor. From [10].

where E is the Young's modulus, ν is the Poisson's ratio, and γ is the conversion factor related to geometrical parameters of the structure [10].
Moreover, the accuracy of such a long-short beam strain sensor benefits from the independence of the displacement of both thickness of the film and Young's modulus, while the analytical model of the sensor is free from correction factors [17].

1.4.3 M-test method

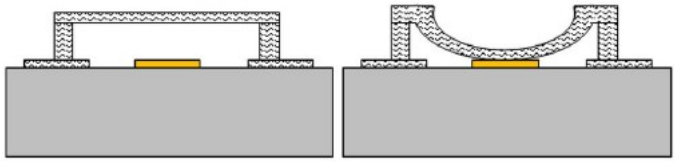

Figure 1.13: Depiction of the M-test method working principle. From [2].

The instability phenomenon of elastic structure subjected to electrostatic actuation named as pull-in has been recognized as a promising method for the characterisation of material properties [1]. Further, the M-test method is an electrostatic beam bending technique and represents a major milestone for the pull-in research [1][10]. Moreover, it can estimate the residual stress gradient along the thickness [2]. The M-test method can be used to measure residual stresses of integrated, free-standing, and thin structures, as well as the Young's modulus [10].
Such an M-test setup consists of an array of MEMS test structures (like cantilever beams, fixed-fixed beams, and clamped diaphragms) of different dimensions, which are all suspended above the fixed ground plane by a gap, as depicted in Figure 1.13 [1]. Further, a voltage is applied between the upper movable conductor and the ground plane, causing a downward deflection of the array of MEMS test structures towards the underlying fixed ground plane, as a consequence of the electrostatic actuation [1][2]. Thus, the upper movable conductor becomes first unstable and then spontaneously pulls in or collapses to

the ground plane, if the applied voltage reaches the critical pull-in value [1]. This pull-in voltage depends on the residual stress present in the MEMS test structures, as well as on mechanical characteristics, like Young's modulus and Poisson's ratio, of the MEMS test structures, or their geometry [2]. By using the electrostatic attraction, this method makes possible to test a batch of specimens simultaneously, as well as the rapid change of the loading state [1].
The beam stiffness of the M-test structure consists of two main components in the presence of residual stress: one caused by the stress component, while the other having the geometrical and mechanical properties as a main cause [2]. Therefore, the pull-in voltage $V_{pull-in}$ can be expressed as [2]:

$$V_{pull-in} = \sqrt{\frac{\gamma_{1n}}{\epsilon_0 L^2 D_n \left(1 + \gamma_{3n} \frac{g_0}{W}\right)}}$$

where

$$D_n = 1 + 2\frac{1 - cosh\left(\frac{\gamma_{2n} kL}{2}\right)}{\frac{\gamma_{2n} kL}{2} sinh\left(\frac{\gamma_{2n} kL}{2}\right)}$$

with

$$k = \sqrt{\frac{12S}{B}}$$

Further, the stress parameter S equals to :

$$S = \tilde{\sigma} t g_0^3$$

while the bending parameter B can be expressed as [2]:

$$B = \tilde{E} t^3 g_0^3$$

Moreover, the numerical constants γ_{1n}, γ_{2n}, and γ_{3n} represent numerical constants for the cantilever beams, fixed-fixed beams, and clamped diaphragms, respectively [1]. ϵ_0 is the vacuum permittivity, L is the beam length or radius of the diaphragm, g_0 is the gap between the ground plane and the test structure, $\tilde{\sigma}$ is the effective residual stress, t is the thickness of the film or diaphragm, and $\tilde{E}$ is the effective Young's modulus [2].
According to [10], the resolution of the M-test structure can reach up to 4 % for single-crystal silicon structures, under the ideal conditions described in [10]. Due to the fact that these conditions are violated by most of the surface-micromachined structures, the major problem of the M-test is revealed: the trade-off between accuracy and modeling complexity [1][10]. Thus, in reality, the modeling errors could further increase as a consequence of MEMS structures imperfections like built-in imposed bending moments due to stress gradients or compliant supports[1].

1.4.4 Bulge test

This last method used for measuring tensile residual stress requires a freestanding thin-film diaphragm [2]. Further, uniform pressure is exerted to one side of this diaphragm, causing it to bulge outward, as shown in Figure 1.14 [2]. In this way, a pressure difference is created between the top and the bottom of the membrane. Thus, the pressure (P) versus the deflection (d) characteristics of the diaphragm are used to extract the stress and strain of the thin film [2]. Therefore, the residual stress σ_R can be expressed in terms of the applied pressure P as follows for a circular diaphragm:

$$P = C_1 \frac{R^t}{a^2} d + C_2 \frac{E}{1-\nu} \frac{t}{a^4} d^3$$

while for a square diaphragm:

$$P = 3.393 \frac{\sigma_R t}{a^2} d + (1.996 - 0.613) \frac{E}{1-\nu} \frac{t}{a^4} d^3$$

where C_1 and C_2 are the geometry dependent shape factors, R is the radius of diaphragm, d is the deflection of the diaphragm, a is the characteristic length, E is the Young's modulus, ν is the Poisson's ratio, while t is the film thickness [2].
Although this method is particularly useful for measuring stress in low-elastic modulus materials, the presented generic formulas can only handle ideal situations due to modeling uncertainties and complexities [2][1]. Another drawback of the bulge test method is the fact that backside etching is needed.

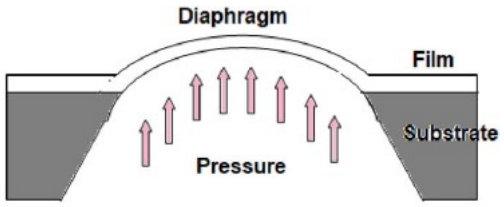

Figure 1.14: Bulge test schematic. From [2].

CHAPTER 2

Simulations of the rotating arm test structure

After analysing the MEMS residual stress characterisation devices described in the section 1.4, the rotating arm test structure was chosen as the test structure to be simulated by using the simulation tool COMSOL Multiphysics. The main reasons for the choice of this specific test structure were its intuitive functioning principle, together with the fact that the rotating arm structure is able to indicate both compressive and tensile stress through in-plane measurements [10].

Figure 2.1 depicts the rotating arm test structure, as simulated in COMSOL Multiphysics.

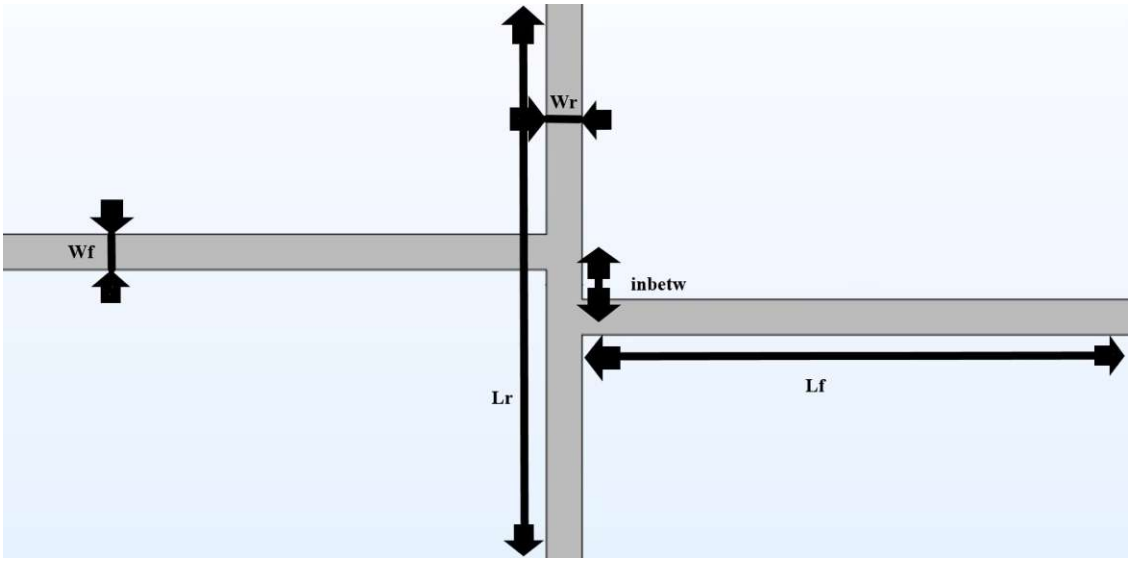

Figure 2.1: Schematic of the simulated rotating arm test structure - top view.

Similar to the test structure depicted in Figure 1.5, it consists of two fixed parallel beams, both L_f long and W_f wide, and a freestanding rotating indicator beam, whose length is equal to L_r, while its width is equal to W_r. Further, the two fixed parallel beams have an offset *inbetw* between them, which includes half the width of both fixed parallel beams.

To simulate a real use case of such a test structure as accurately as possible, the

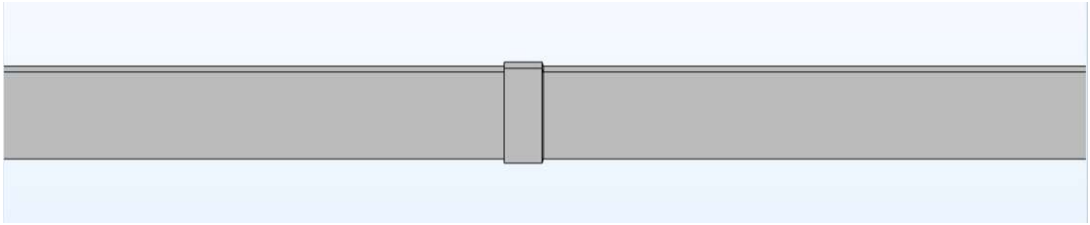

Figure 2.2: Schematic of the simulated rotating arm test structure - side view.

simulated structure is made out of two extruded work planes, united together to a single COMSOL component, as it can be seen in Figure 2.2. The base layer, which is 15 μm thick, contains the rotating arm test structure and has no stress applied. The stress, which has to be measured by the rotating arm test structure, is applied only on the thinner top layer, which is therefore only 1 μm thick. The stress was applied only in the x and y directions, in equal shares of 1000 MPa, in order to verify the extent to which the rotating arm structure will rotate in the x-y plane, as well as buckle out of the x-y plane. The applied stress values were chosen according to the targeted measurement range of the simulated test structure and were introduced in the initial stress matrix of COMSOL Linear Elastic Material model. For more clarity, Figure 2.3 depicts the simulated rotating arm test structure, together with the used x-y-z coordinates.

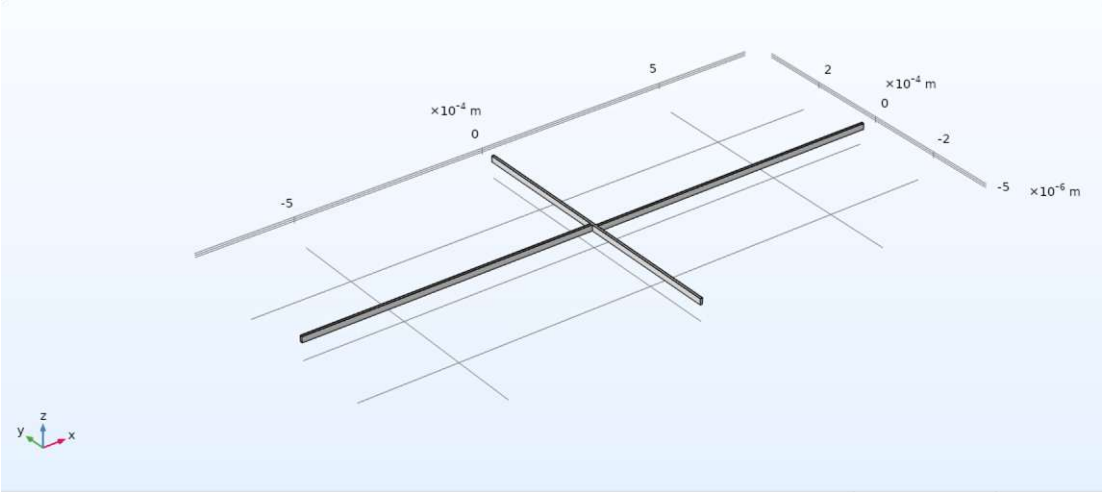

Figure 2.3: Schematic of the simulated rotating arm test structure - x-y-z coordinates.

Further, both the base and the top layer were simulated as being made out of single crystal, anisotropic Si. As depicted in Figure 1.5, only the rotating indicator beam should be free to rotate as a consequence of stress. Therefore, the only used constraint stated that both fixed beams should stay fixed at their ends, which were opposite to the rotating indicator beam, during the simulation. A Free Tetrahedral COMSOL Mesh was used, with the Mesh size *Finer*. The aforementioned Mesh settings were perceived as the optimal tradeoff between the needed accuracy of the simulation results and a reasonable computation time.
As next, two COMSOL studies were added: one Stationary and one Parametric Sweep. The Stationary Study was used for simulating the stationary state of the built test structure and also included geometric nonlinearities. On the other side, the goal of the Parametric sweep was to vary the values of the parameters W_r, W_f, and *inbetw*. The aforementioned parameters were chosen as they were expected to influence the rotation of the rotating indicator beam in a non-linear manner. In contrast, in the case of the length of the fixed beams L_f and of the length of the rotating indicator beam L_r, the measured deflection was predicted to react linearly to the growth of L_f and L_r. Therefore, the lengths of the beams were not systematically varied, which reduced the needed computation time. Thus, the dimensions of the similar structures presented in [15], [4], [16], and [19] were used as a starting point for defining four pairs of equal lengths for the fixed and rotating indicator beam, to which the four rotating arm test structures from Table 2.1 correspond:

Structure number	L_f	L_r
1	250 μm	250 μm
2	500 μm	500 μm
3	750 μm	750 μm
4	1000 μm	1000 μm

Table 2.1: Overview of the fixed and rotating indicator beam lengths for the four simulated rotating arm test structures.

The settings of the Parametric Sweep were also inspired by the dimensions of the similar structures used as starting points for the definition of L_f and L_r. Further, the same Parametric Sweep settings as listed in Table 2.2 were used for all the four simulated test structures from Table 2.1. The start value defines the lower limit of the range of values covered by the Parametric Sweep, while the stop value defines its upper limit. The step size represents the length difference between two consecutive values of the range covered by the Parametric Sweep.

Parameter name	start value	stop value	step size
W_r	6 μm	12 μm	6 μm
W_f	6 μm	24 μm	2 μm
inbetw	0 μm	20 μm	1 μm

Table 2.2: Settings of the Parametric Sweep study: overview.

A more straightforward approach for measuring the rotation of the indicator beam instead of recording its rotation degree is to monitor the displacement in the direction of the x-axis at the ends of the rotating indicator beam. Therefore, two COMSOL Point Evaluations were added at the ends of the rotating indicator beam: Point 20, as highlighted in red in Figure 2.4, at the lower end of the beam, while Point 28, as highlighted in red in Figure 2.5, at its upper end.

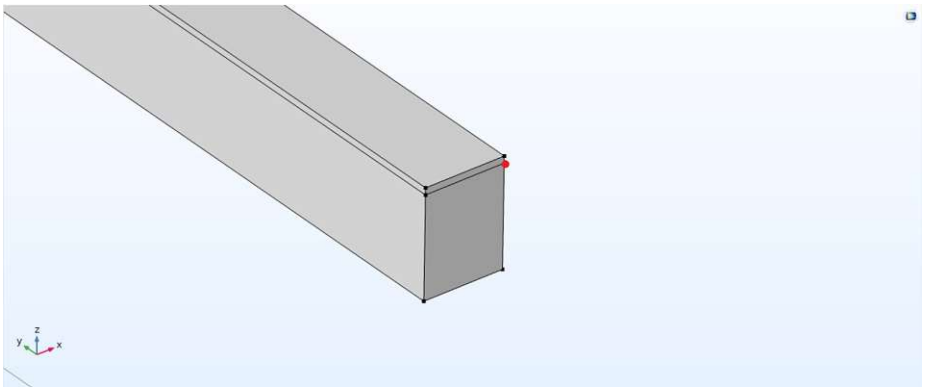

Figure 2.4: Position of Point 20 (highlighted red point).

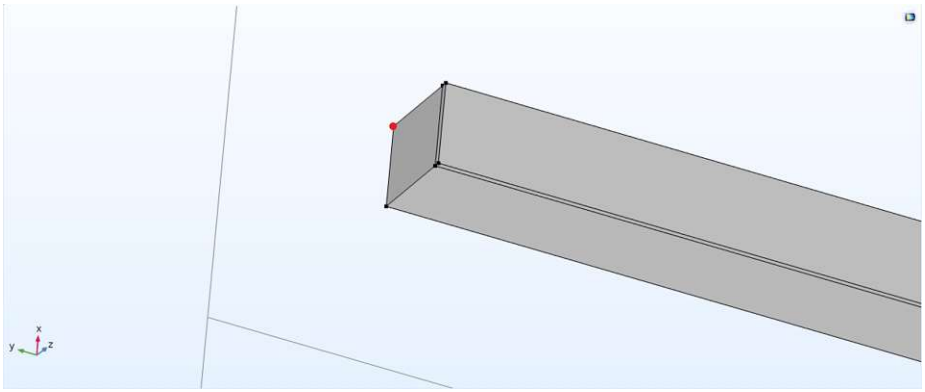

Figure 2.5: Position of Point 28 (highlighted red point).

The scope of the COMSOL simulations is to find the suitable parameters for fabricating a rotating arm test structure able to cover the desired measurement range: from -1 GPa to 1 GPa. Thus, the three parameters varied through the Parametric Sweep (W_r, W_f, and *inbetw*) were systematically kept one or two at a time constant at convenient values, while the other ones were varied. The resulted x-displacement values were evaluated in the form of COMSOL Tables. Further, these table values were displayed as 1D or 2D plots, which were finally analysed to discover the most suitable rotating arm test structure dimensions.
First, W_r, W_f, and *inbetw* were varied, and the resulting 3D plot revealed the first finding of the analysis: W_r does not have any influence on the measuring capability of the rotating arm test structure and can therefore be arbitrarily chosen. This property of W_r was to be anticipated and is characteristic to all four simulated test structures, as presented in Table 2.1. Since the target was to reach the desired measurement range with the minimal needed dimensions of the test structure, the smallest value assigned to W_r through the Parametric Sweep, 6 μm, was further used for the 2D and 1D plots.

2.1 2D plots

Managing to cover the entire measurement range means that the x-displacement registered at the Points 20 and 28, respectively, due to the 1000 MPa stress applied in the upper layer, has to be readable under the microscope. Thus, the x-displacement is displayed by using a colour scale, as depicted in Figure 2.6 for the first pair of dimensions of the simulated rotating arm test structure from Table 2.1: both L_r and L_f equal to 250 μm. For obtaining such a 2D plot, both W_f and *inbetw* were varied across the whole range of values covered by the Parametric Sweep, as stated in Table 2.2.

The main interest of the 2D plots was on the highest achieved x-displacement, highlighted in dark red. The optimal values for W_f and *inbetw* were assumed to be the ones which correspond to this point of maximum of the x-displacement. Thus, the optimal value of W_f can be read on the x-axis, while the optimal range of values of *inbetw* can be read on the y-axis. A similarity between the 2D plots is exemplified by using Figure 2.6: while the optimal value of W_f can be easily identified as equal to 6 μm, the optimal value of *inbetw* can not be read with the same accuracy. Thus, the 2D plot can only provide an optimal range: from 6 μm to 10 μm for this first simulated test structure (see Table 2.1). By following the same methodology, the optimal value of W_f and the optimal range of values for *inbetw* can be obtained for the second, third, and fourth simulated rotating arm test structures (as sorted in Table 2.1) by analysing Figure 2.7, Figure 2.8, and Figure 2.9, respectively.

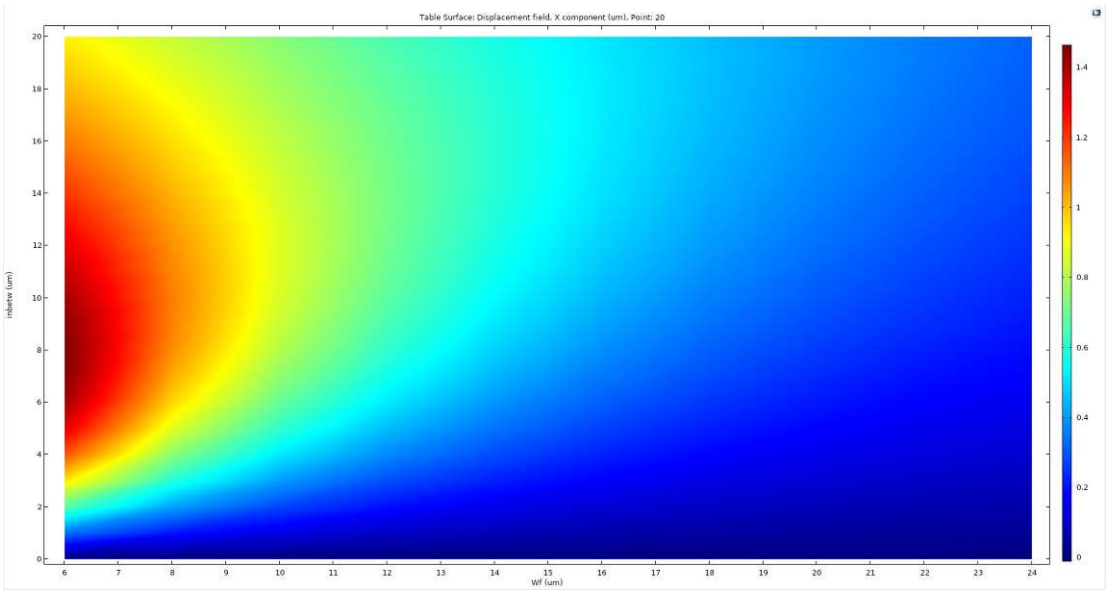

Figure 2.6: 2D plot for the first simulated rotating arm test structure ($L_f = L_r = 250$ μm) : ideal values of W_f (x-axis) and ideal range of values for *inbetw* (y-axis) for the highest x-displacement registered at Point 20 (highlighted in dark red in the colour scale).

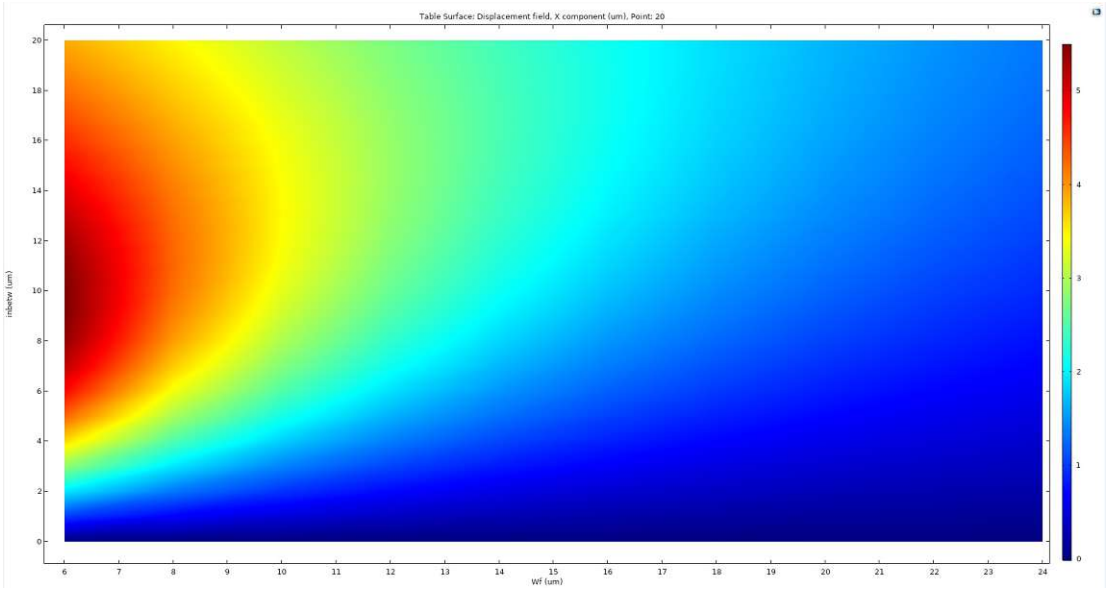

Figure 2.7: 2D plot for the second simulated rotating arm test structure ($L_f = L_r =$ 500 μm): ideal values of W_f (x-axis) and ideal range of values for *inbetw* (y-axis) for the highest x-displacement registered at Point 20 (highlighted in dark red in the colour scale).

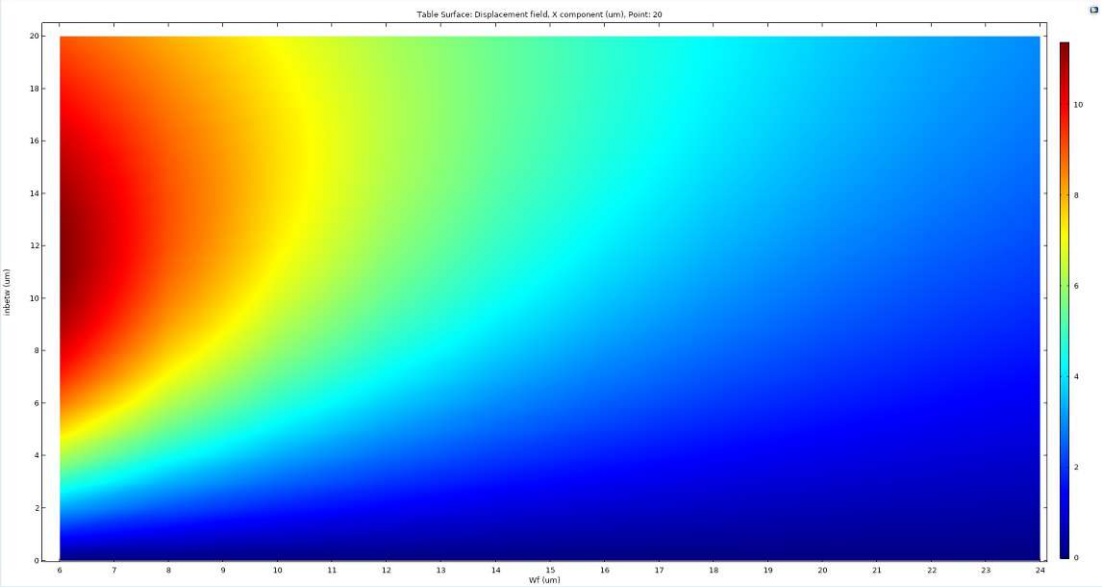

Figure 2.8: 2D plot for the third simulated rotating arm test structure ($L_f = L_r = 750$ μm): ideal values of W_f (x-axis) and ideal range of values for *inbetw* (y-axis) for the highest x-displacement registered at Point 20 (highlighted in dark red in the colour scale).

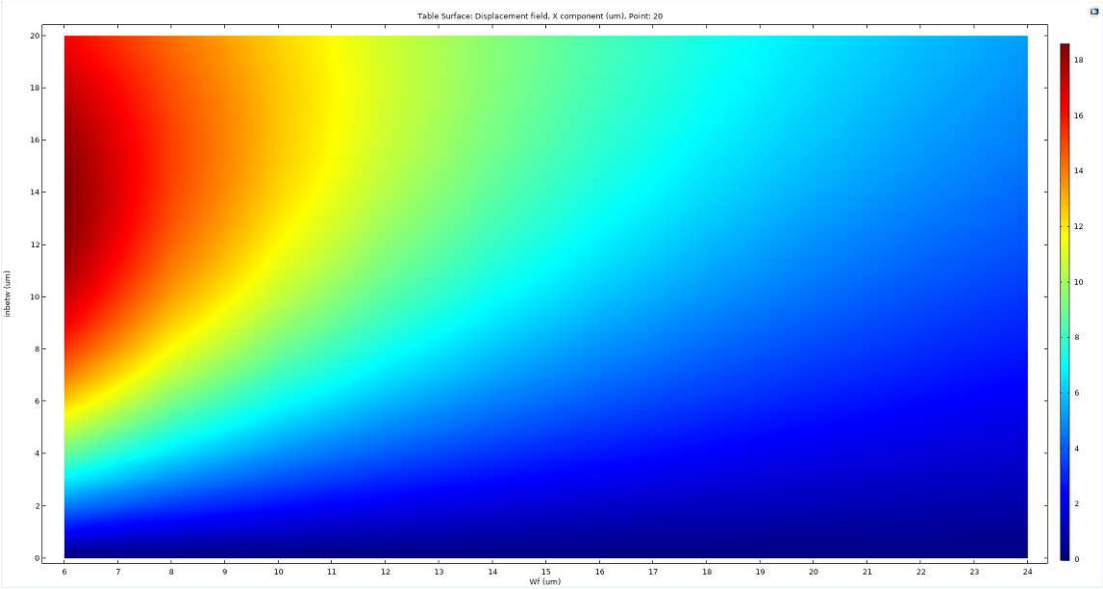

Figure 2.9: 2D plot for the fourth simulated rotating arm test structure ($L_f = L_r = 1000$ μm): ideal values of W_f (x-axis) and ideal range of values for *inbetw* (y-axis) for the highest x-displacement registered at Point 20 (highlighted in dark red in the colour scale).

Due to the position of Point 20, at the lower end of the rotating indicator beam (see Figure 2.4), and the position of Point 28, at the upper end of the rotating indicator beam (see Figure 2.5), it is to be anticipated that one of the points will register a positive x-displacement, while the other point will register a negative x-displacement.
The counterclockwise rotation of the rotating indicator beam, as a consequence of the applied stress, was observed for all simulated rotating arm test structures (as listed in Table 2.1) and is depicted for the rotating arm test structure with $L_f = L_r = 750$ μm in Figure 2.10.
Further, the 2D plots generated in the same manner as the ones for Point 20, depicted

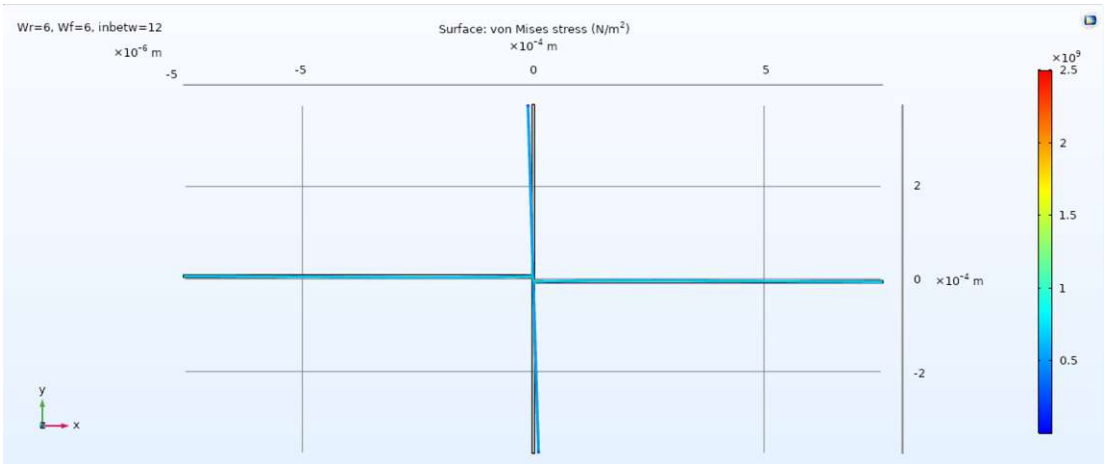

Figure 2.10: 2D plot showing the counterclockwise rotation of the rotating arm test structure with $L_f = L_r = 750$ μm. The colour scale depicts the stress values applied in the different regions of the rotating arm test structure.

in Figure 2.6 - 2.9, but for Point 28, confirmed the aforementioned anticipated behaviour. These 2D plots generated from Point Evaluation 28 did not provide any new data, they only displayed the data already obtained from Point Evaluation 20 mirrored. In this way, the correctness of the x-displacement, W_f, and *inbetw* was successfully verified. In consequence, the 2D plots generated for Point 28 are not part of this diploma thesis.

To sum up, the maximal x-displacements displayed by the colour scales of the 2D plots (see Figure 2.6 - 2.9) can be found in Table 2.3:

Structure number	L_f	L_r	maximal x-displacement
1	250 μm	250 μm	1.4 μm
2	500 μm	500 μm	5 μm
3	750 μm	750 μm	10 μm
4	1000 μm	1000 μm	18 μm

Table 2.3: Overview of the maximal x-displacements displayed by the colour scales of the 2D plots (see Figure 2.6 - 2.9).

The main criteria used to select the simulated rotating arm test structures to be fabricated was the readability of the device displacement under an optical microscope. Such readability can be assured for x-displacements of at least 5 μm. Thus, the third and the fourth structures from Table 2.3 were further considered as potential rotating arm structures to be fabricated.

2.2 1D plots

Next, an accurate value of the *inbetw* parameter was the missing piece of the puzzle for both structures with the dimensions $L_f = L_r = 1000$ μm and $L_f = L_r = 750$ μm. As the 2D plots were only able to deliver an optimal range of values for *inbetw*, 1D plots, like the one depicted in Figure 2.11, were created.

For obtaining such a 1D plot, only *inbetw* was varied across the whole range of values

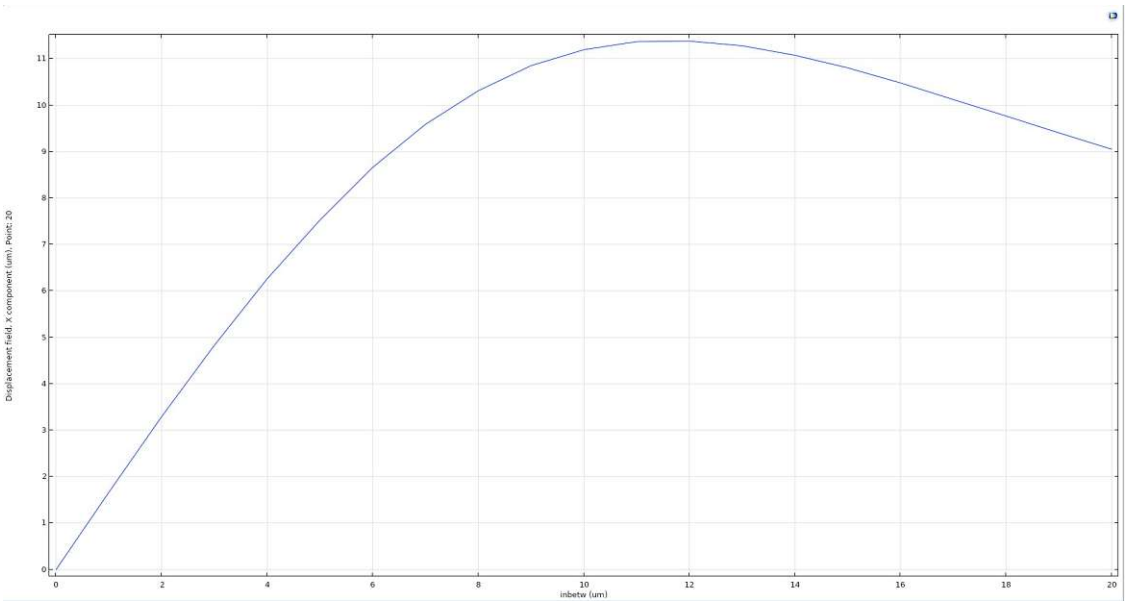

Figure 2.11: 1D plot for the third simulated rotating arm test structure ($L_f = L_r = 750$ μm): ideal value of *inbetw* (x-axis) for the highest x-displacement value registered at Point 20 (y-axis).

covered by the Parametric Sweep, as stated in Table 2.2. The blue line in Figure 2.11 and Figure 2.12 outlines the x-displacement values registered at Point 20 for each of the varied *inbetw* values. The optimal value for *inbetw* can be read on the x-axis and was assumed to be the one that corresponds to the highest registered x-displacement, according to the y-axis.

Similar to the analysis of the 2D plots, the 1D plots generated from Point Evaluation 28 were only used to verify the correctness of the Figures 2.11 and 2.12. Thus, they are not part of this diploma thesis.

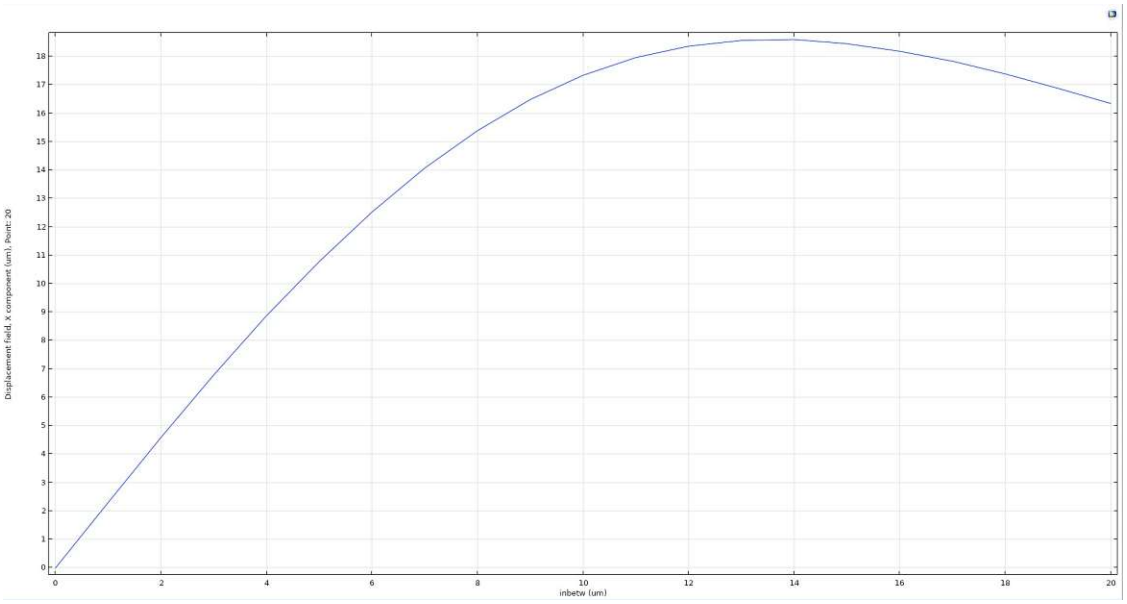

Figure 2.12: 1D plot for the fourth simulated rotating arm test structure ($L_f = L_r = 1000$ μm): ideal value of *inbetw* (x-axis) for the highest x-displacement value registered at Point 20 (y-axis).

With the *inbetw* values obtained through the analysis of the Figures 2.11 and 2.12, all the values of the parameters needed for fabricating the structures 3 and 4 (according to Table 2.1) are defined, as shown in Table 2.4.

Structure number	L_f	L_r	W_f	W_r	*inbetw*
3	750 μm	750 μm	6 μm	6 μm	12 μm
4	1000 μm	1000 μm	6 μm	6 μm	14 μm

Table 2.4: Overview of the optimal values for the third and the fourth simulated rotating arm test structure (according to Table 2.1).

2.3 Out-of-plane deflection

Besides the x-displacement, needed as an indicator for the rotation of the rotating indicator beam, the z-displacement was also registered at both Point Evaluation 20 and 28. The reason for this separate analysis was to identify potential out-of-plane deflection of the rotating indicator beams.
As for the x-displacements, the resulting z-displacement values were also evaluated in the form of COMSOL Tables. As all the values of the parameters needed for fabricating structures 3 and 4 (according to Table 2.1) were already determined (see Table 2.4) before starting the out-of-plane deflection analysis, only the z-displacement values corresponding to these already determined parameter values of the rotating arm test structures were of interest. Thus, no plots of the resulting z-displacements were generated.

Next, two further Point Evaluations were added to measure the z-displacement near the middle of the rotating arm test structure. While Point Evaluation 13 (see Point 13 highlighted in red in Figure 2.13) serves as a comparison for the z-displacement value from Point Evaluation 28, Point Evaluation 14 (see Point 14 highlighted in red in Figure 2.14) serves as a comparison for the z-displacement value from Point Evaluation 20. In this way, it could be analysed if a potential out-of-plane deflection affects only the lower (corresponding to Point Evaluation 20) and the upper end (corresponding to Point Evaluation 28) of the rotating indicator beam or the entire rotating arm test structure.

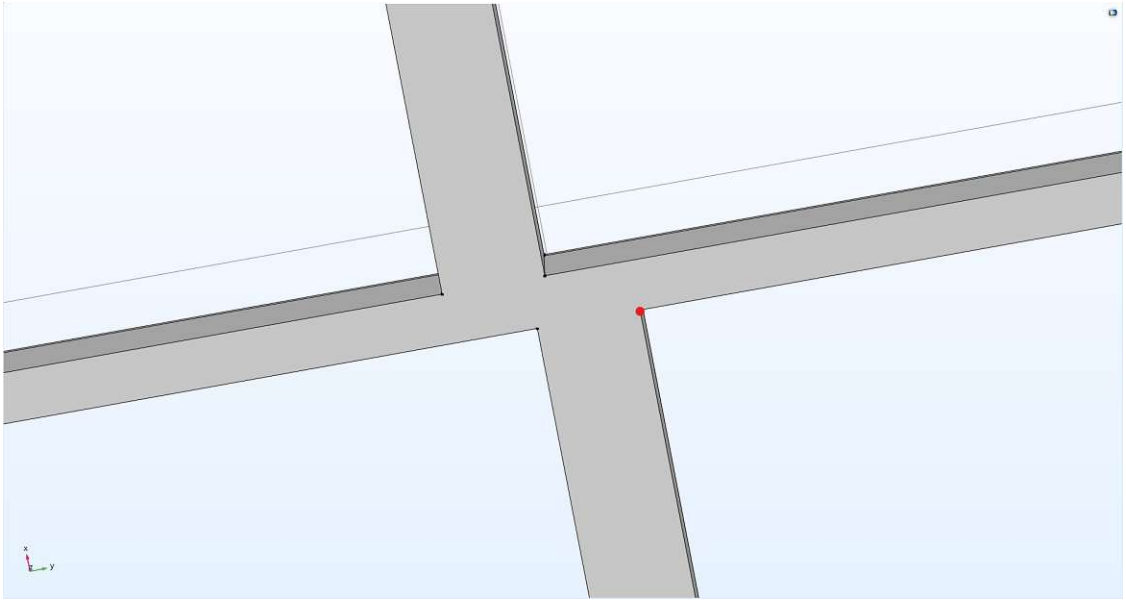

Figure 2.13: Position of Point 13 (highlighted red point).

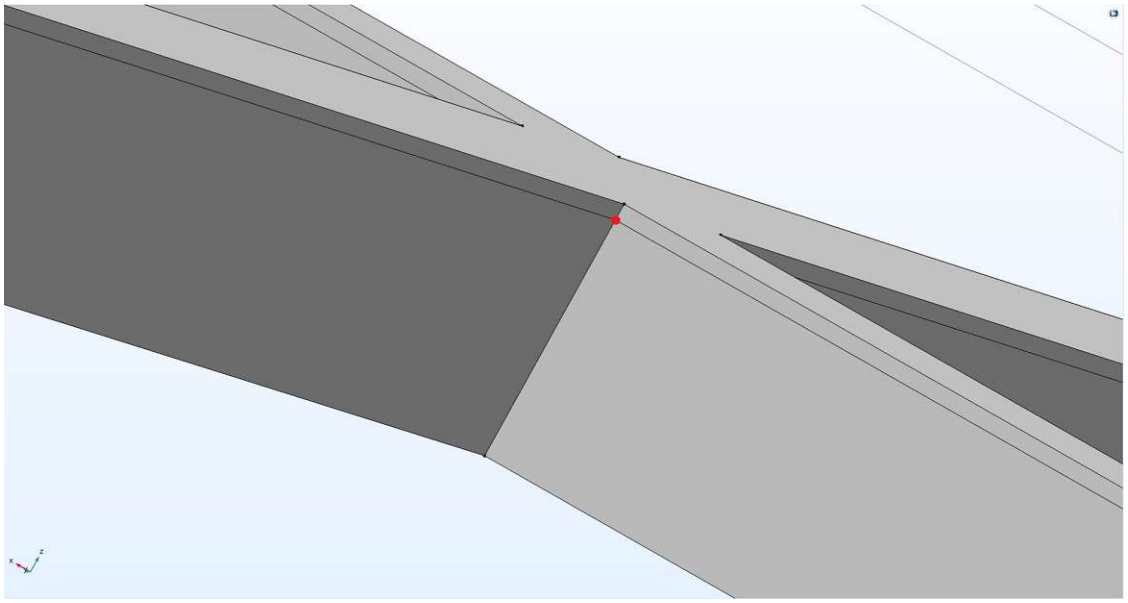

Figure 2.14: Position of Point 14 (highlighted red point).

Next, Table 2.5 contains the z-displacements registered at Point Evaluation 20, 14, 28, and 13, for both the rotating arm structure with $L_f = L_r = 750$ μm and the one with $L_f = L_r = 1000$ μm.

$L_f = L_r$	Pt. Ev. 20	Pt. Ev. 14	Pt. Ev. 28	Pt. Ev. 13
750 μm	8.981 μm	0.382 μm	8.99 μm	0.378 μm
1000 μm	16.24 μm	0.563 μm	15.43 μm	0.559 μm

Table 2.5: Overview of the z-displacement values registered at Point Evaluation 20, 14, 28, and 13 for the third and the fourth simulated rotating arm test structure (according to Table 2.1).

The z-displacements presented in Table 2.5 lead to a clear conclusion: the rotating indicator beam of both the rotating arm test structure with $L_f = L_r = 750$ μm and the one with $L_f = L_r = 1000$ μm shows out-of-plane deflection. The z-displacements registered at Point Evaluation 14 and Point Evaluation 13 show values smaller than 1 μm. Thus, these z-displacement values serve as evidence that the out-of-plane buckling phenomenon affects only the upper and lower ends of the rotating indicator beams, but not the entire rotating arm test structures. This described behavior is depicted in Figure 2.15 for the rotating arm test structure with $L_f = L_r = 750$ μm and in Figure 2.16 for the rotating arm test structure with $L_f = L_r = 1000$ μm.

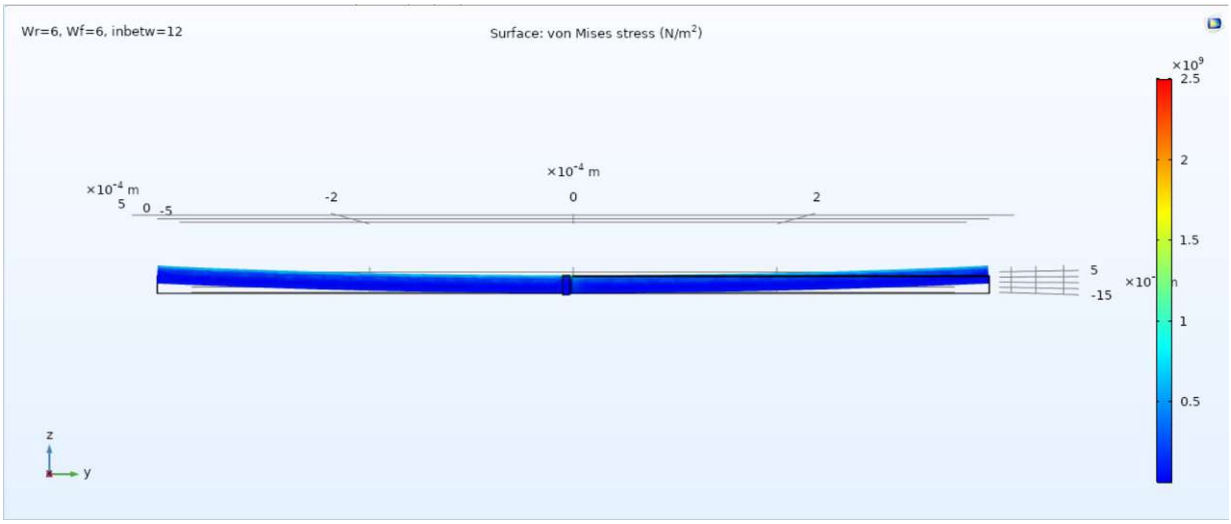

Figure 2.15: Depiction of the out-of-plane buckling phenomenon at the ends of the rotating indicator beam for the third simulated rotating arm test structure (according to Table 2.1).

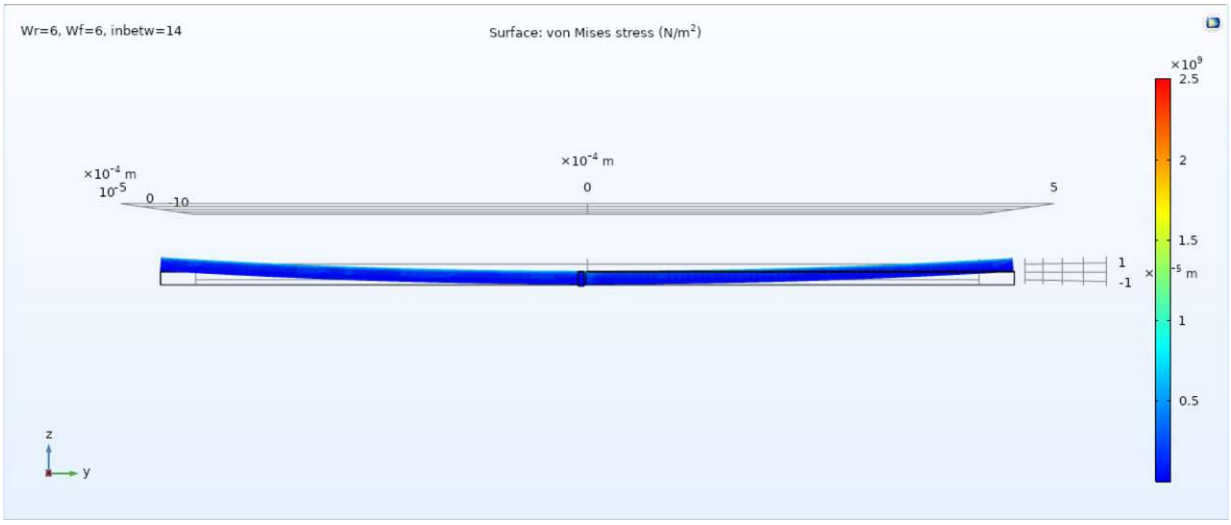

Figure 2.16: Depiction of the out-of-plane buckling phenomenon at the ends of the rotating indicator beam for the fourth simulated rotating arm test structure (according to Table 2.1).

The next step for turning the two chosen simulated rotating arm test structures, as parameterised in Table 2.4, into reality, was to export the COMSOL structures as an AUTOCAD-specific data type, needed for the realisation of the photolithography masks. Unfortunately, the bare export of the already existing COMSOL structures into the desired AUTOCAD-compatible files could not be achieved. This technical inconvenience

and the undesired discovery, that the ends of the rotating arm test structures were deflecting out-of-plane, led to two improved AUTOCAD designs of both the rotating arm test structure with $L_f = L_r = 750$ μm and the one with $L_f = L_r = 1000$ μm. These improved designs are still based on the third and the fourth simulated rotating arm test structure (according to Table 2.1) with the ideal parameter values from Table 2.4, but include changes aimed at reducing the out-of-plane deflection, on the one side, and ensuring a successful fabrication process of the rotating arm structures, on the other side. Further, these AUTOCAD designs incorporate considerations taken for ensuring smooth handling during the verification measurements of the rotating arm test structures and are described in the next chapter of this diploma thesis.

CHAPTER 3

Design and fabrication of the rotating arm test structure

3.1 Improved design of the rotating arm test structure

As announced at the end of the second chapter of this diploma thesis, the COMSOL simulations led to several findings, which were incorporated in the improved AUTOCAD design, as depicted for the smaller rotating arm test structure ($L_f = 757$ μm) in Figure 3.1. The characteristic parameters of this new design are defined by using this smaller rotating arm test structure as an example. The larger rotating arm test structure, as depicted in Figure 3.2, is defined by the same parameters as the smaller one, but with correspondingly larger values (see Table 3.2).
Similar to the test structure depicted in Figure 2.1, the design of the smaller rotating arm test structure consists of two fixed parallel beams, both L_f long and W_f wide, with the same offset *inbetw* between them. Different from the design of the rotating arm test structure simulated in COMSOL, the fixed beams maintain their optimal width, according to the COMSOL simulations (see Table 2.4), only at their joint with the rotating indicator beam, while the rest of the beam was widened for increasing the stability of the structure. Further, the rotating indicator beam is still freestanding and is made out of three parts: one central part, having the same width W_{rc} as the rotating indicator beam of the COMSOL simulated design of the rotating arm test structure, and two display beams, each of which is parallel to one fixed beam and wider than the central part due to the same purpose of increasing the stability, which end in an arrow shape. The x-displacement of the rotating indicator beam, as listed in Table 2.3, is the main indicator of device sensitivity in the case of the rotating arm test structure depicted in Figure 2.1. The improved AUTOCAD design of the rotating arm test structure (see Figure 3.1 and Figure 3.2) shifts this indicator role to the rotation of the display beams.

Next, the fixed beams and the rotating indicator beams were equally long for all the four simulated rotating arm test structures listed in Table 2.1. In contrast, the display beams of the rotating arm test structure depicted in Figure 3.1 are shorter than the fixed beams, while the fixed beams of this improved AUTOCAD design are minimally lengthened compared to the ones of the COMSOL simulated rotating arm test structure, as listed in Table 2.4, to ensure a smooth fabrication process.
Further, Figure 3.1 depicts only an improved design of the COMSOL simulated rotating arm test structure design, on which the stressed thin film will be deposited, as described elaborately in the fourth chapter of this diploma thesis. While the rotating arm test structure design depicted in Figure 2.1 was simulated as a COMSOL component consisting of one base layer, which contains the rotating arm test structure and has no stress applied, and one 1 μm thick, stressed top layer (see Figure 2.2), the components of the improved AUTOCAD rotating arm test structure design are distributed on several AUTOCAD layers, as depicted in Figure 3.1. The rotating arm test structure itself, outlined in neon green, is placed on the $SILICONTOPSIDE$ layer, while the scales used for measuring the rotation of the display beam are outlined in yellow and are placed on the $BOTTOMELECTRODE$ layer. Finally, the red frame of the whole rotating arm test structure is placed on the $SILICONBACKSIDE$ layer.

Figure 3.3 depicts only one half of the smaller rotating arm test structure (L_f = 757 μm), on which the length and width of both the fixed (L_f, W_f) and the display beam (L_d, W_d), together with the distance between the display and the fixed beam d_{df} and the length of the central part of the rotating indicator beam L_{rc}, are marked.
The length of the fixed beam L_f is defined as the distance between its joint with the central part of the rotating indicator beam and the frame of the structure. The width of the fixed beam W_f defines its maximum width, achieved only for the part of the fixed beam parallel to the display beam. Further, the length of the display beam L_d is defined as the distance between the central part of the rotating indicator beam and the arrow shape intended to show the rotation of the display beam on the scale. The width of the display beam W_d defines its maximum width, achieved for the whole beam except the aforementioned arrow shape.
Next, the distance between the display and the fixed beam d_{df} is measured between the parallel areas of the aforementioned beams. Its values were calculated with the help of a Python script, which had L_d, L_{rc}, and the rotation angle registered for the highest x-displacement value of the third and fourth COMSOL simulated rotating arm test structures, as listed in Table 2.3, as inputs. This Python script generated plots with the maximal positive and negative x and y-displacement of the display beams as outputs (see Figure 3.4 for the smaller and Figure 3.5 for the larger rotating arm test structure). The values of d_{df} listed in Table 3.2 were obtained by doubling the corresponding maximal x-displacement values from Table 3.1. Further, the same d_{df} distance was also maintained between the lateral parts of the frame of the rotating arm test structure and the display beams. In this way, the areas that needed to be removed through the etching process, as further described in the next subchapter, were as equal as possible in order to ensure a

successful etching.
Another use of the distance between the display and the fixed beam was as input for calculating the length of the central part of the rotating indicator beam L_{rc} by using the following formula:

$$L_{rc} = 2d_{df} + \Delta + 2W_d$$

where the Δ parameter is equal with 8 μm for the smaller and with 6 μm for the larger rotating arm test structure, respectively. Δ describes the part of L_{rc} not parameterised by the distance between the display and the fixed beam d_{df} or by the width of the display beam W_d, respectively.

L_f	maximal x-displacement	maximal y-displacement
757 μm	20 μm	4 μm
1013 μm	36 μm	7 μm

Table 3.1: Overview of the maximal x and y-displacement values registered for the smaller (see Figure 3.4) and for the larger rotating arm test structure (see Figure 3.5).

Different from the design of the rotating arm test structure simulated in COMSOL, the *inbetw* parameter, as marked in Figure 3.6, does not include half the width of both fixed parallel beams (W_f) anymore, as the fixed beams of the improved AUTOCAD design of the rotating arm test structure are ten times wider than the ones of the rotating arm test structure depicted in Figure 2.1. The updated *inbetw* parameter only includes half of the width of the fixed beams at their joint with the central part of the rotating indicator beam (W_{fc}), which is also marked in Figure 3.6. To ensure both the stability and the optimal performance of the rotating arm test structure, the fixed beams narrow under an angle of 45° up to their optimal width according to the COMSOL simulations, as listed in Table 2.4, while the width of the central part of the rotating indicator beam (W_{rc}), also marked in Figure 3.6, is designed equal to the optimal width.

Next, the y-displacement values of the display beam listed in Table 3.1 led to the inclined scale used for measuring its rotation, as depicted in Figure 3.7. This design input, together with the value chosen for the distance between the tip of the arrow shape designed at the end of the display beam and the frame surrounding the whole rotating arm test structure (d_{ak}), ensures that the rotation of the display beams can be easily read, without risking to collide with the remaining wall, located under the inclined scale (see Figures 3.11 - 3.12). Further, another design input occurred for maintaining d_{ak} was the lengthening of the fixed beams by 7 μm for the smaller and by 13 μm for the larger rotating arm test structure, respectively, when compared to the 750 μm or the 1000 μm long fixed beams of the COMSOL simulated rotating arm test structures.
Although designing the display beams with elongated tips at their end could have increased the readability of their rotation on the scale, the possible damage of such elongated

tips during the etching process led to the arrow shape design, as depicted in Figure 3.7. The dimensions of the arrow shape are designed as a compromise able to ensure both smooth fabrication and clear readability. Thus, the display beams narrow under an angle of 45°, while the height of the arrow h_a, defined as the distance between its tip and the imaginary horizontal line between the part of the display beam parallel to the fixed beam and its narrowed end part, is marked in Figure 3.7. Finally, the markers of the scale used for measuring the rotation of the display beam are displaced in 5 μm intervals.

The larger rotating arm test structure (L_f = 1013 μm), as depicted in Figure 3.2, is designed after the same design principles as the smaller one. The increased values of its parameters are listed together with the values of the smaller rotating arm test structure in Table 3.2.
The following step was to group one smaller together with one larger rotating arm test structure, either straight-oriented, as depicted in Figure 3.8, or rotated by 45°, as depicted in Figure 3.9. Next, 69 such straight-oriented pairs of rotating arm test structures and 67 pairs of rotating arm test structures rotated by 45° were placed on the mask template, along specific alignment marks. Thus, the mask design needed to fabricate the rotating arm test structures, as described elaborately in the next subchapter, was completed and ready to be ordered.

Parameter	Value structure L_f = 757 μm	Value structure L_f = 1013 μm
L_f	757 μm	1013 μm
W_f	60 μm	60 μm
L_d	735 μm	985 μm
W_d	20 μm	20 μm
d_{df}	40 μm	72 μm
L_{rc}	128 μm	190 μm
$inbetw$	12 μm	14 μm
W_{fc}	6 μm	6 μm
W_{rc}	6 μm	6 μm
h_a	10 μm	10 μm
d_{ak}	5 μm	5 μm

Table 3.2: Overview of the parameter values of the smaller (see Figure 3.1) and of the larger rotating arm test structure (see Figure 3.2).

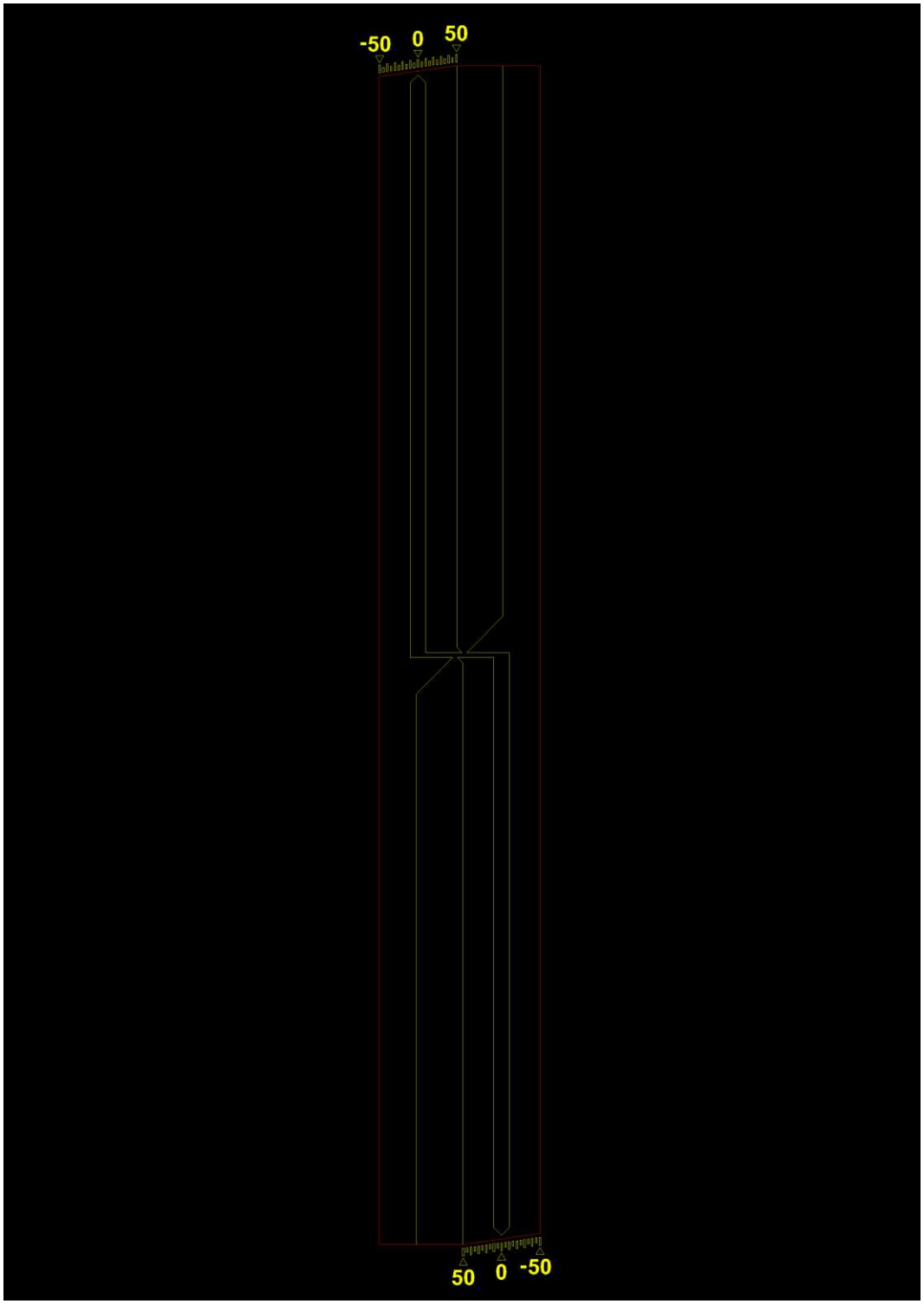

Figure 3.1: Schematic of the smaller rotating arm test structure ($L_f = 757$ μm) - top view.

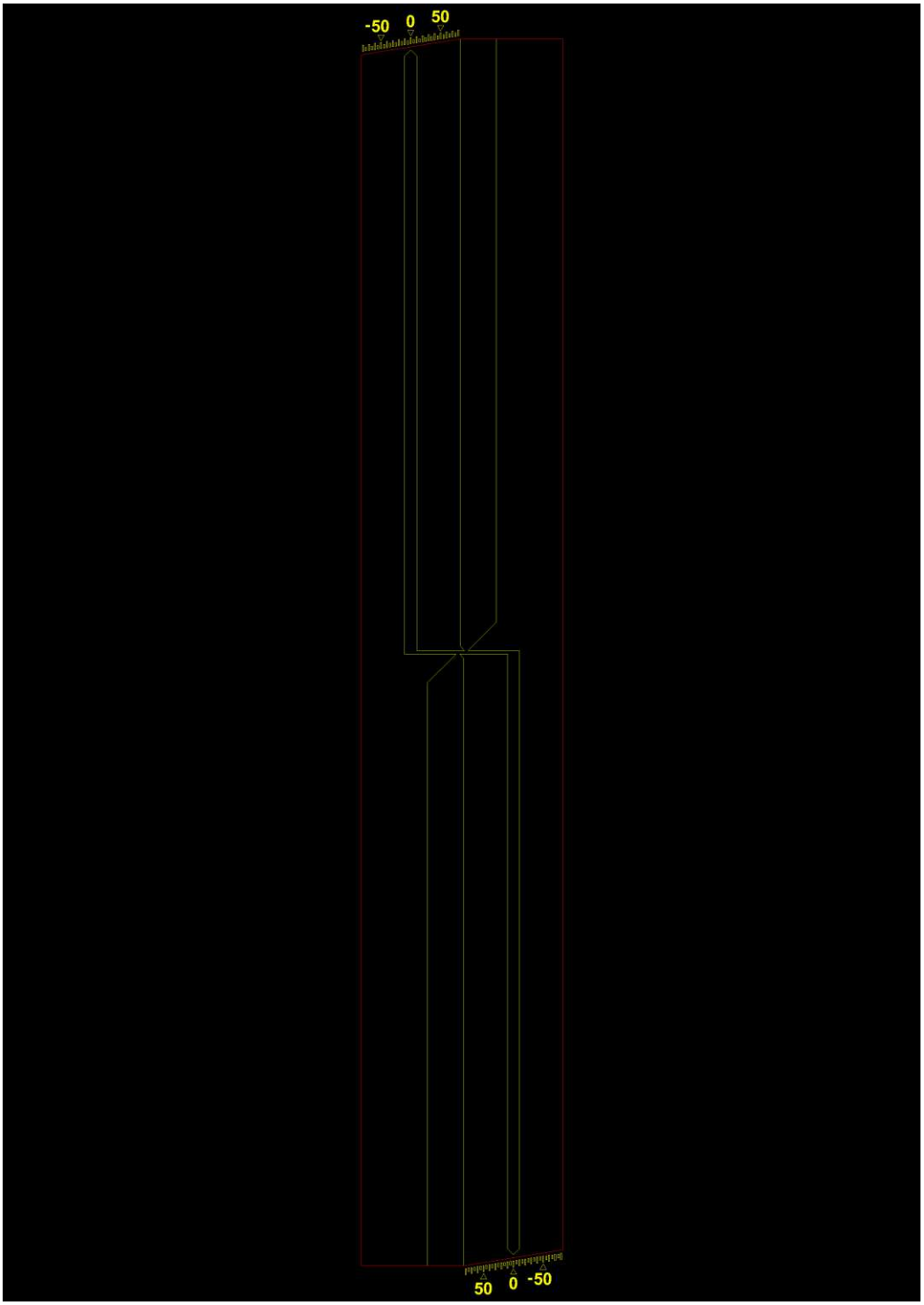

Figure 3.2: Schematic of the larger rotating arm test structure ($L_f = 1013$ μm) - top view.

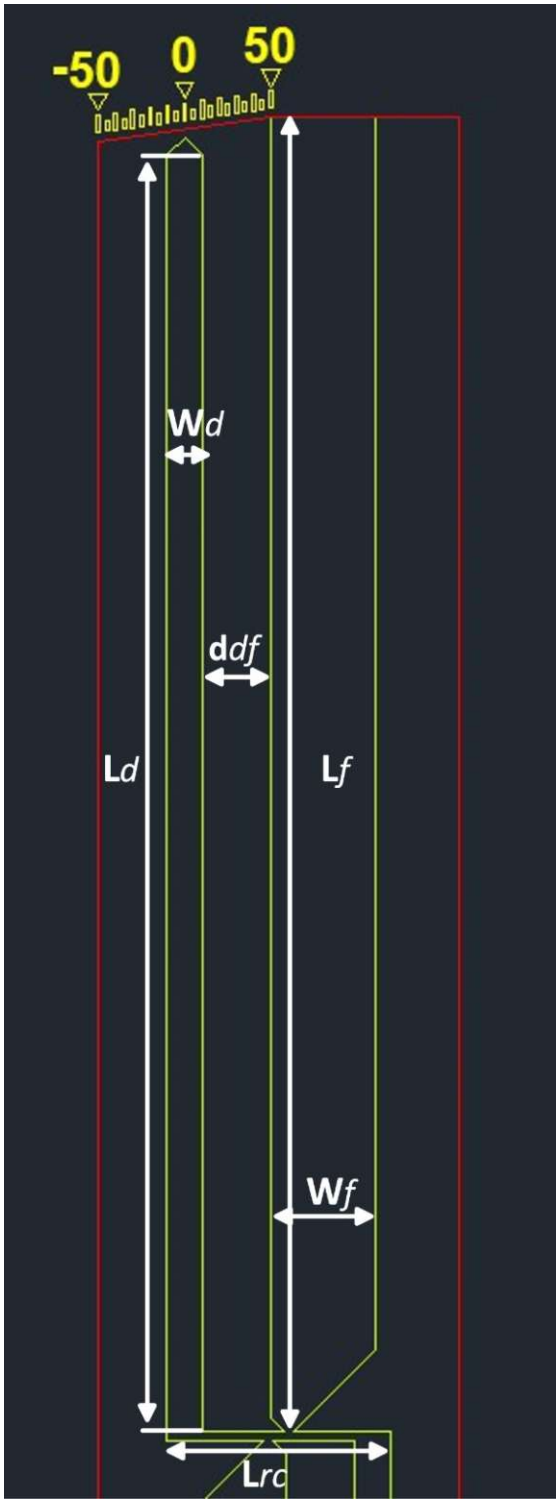

Figure 3.3: Schematic of one half of the smaller rotating arm test structure ($L_f = 757$ μm) - zoomed view.

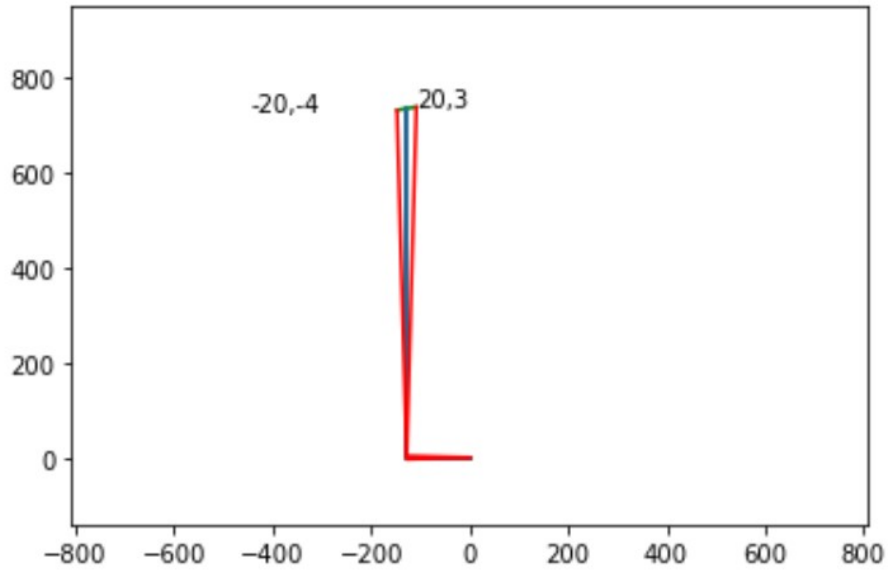

Figure 3.4: Maximal positive and negative x and y-displacements of a display beam of the smaller rotating arm test structure ($L_f = 757$ μm).

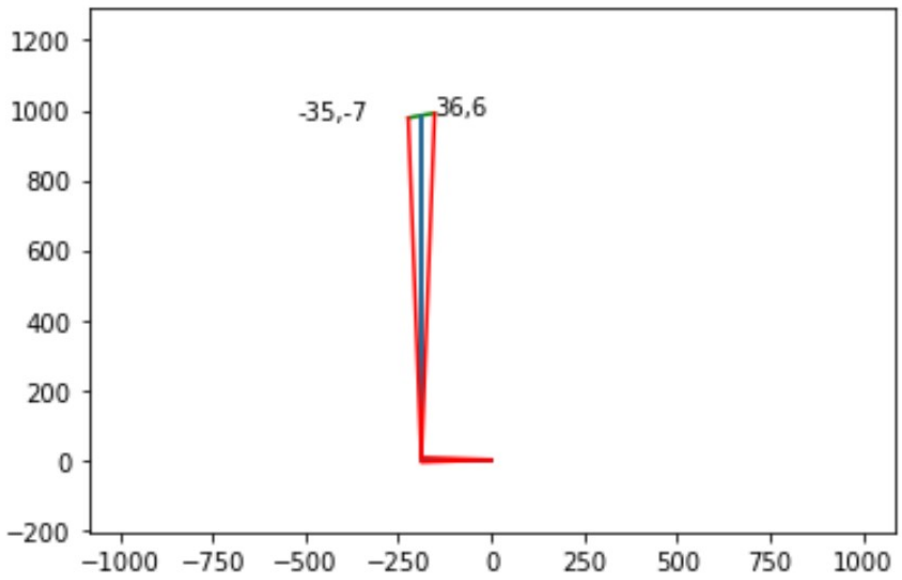

Figure 3.5: Maximal positive and negative x and y-displacements of a display beam of the larger rotating arm test structure ($L_f = 1013$ μm).

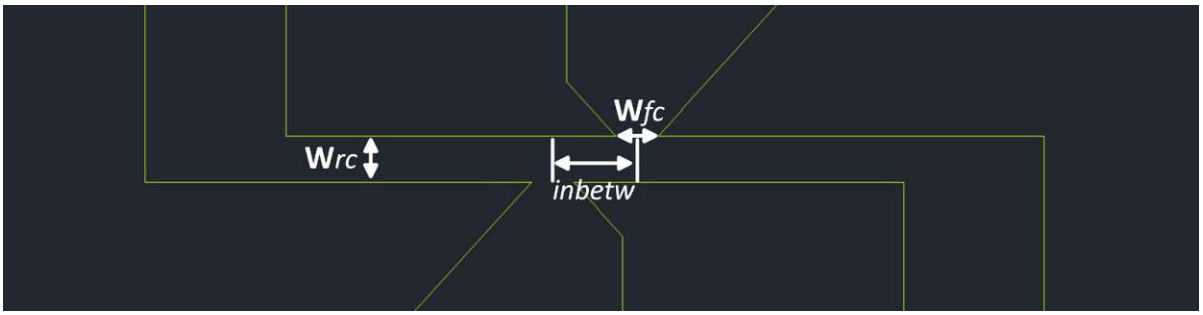

Figure 3.6: Central part of the smaller rotating arm test structure (L_f = 757 μm) - zoomed view.

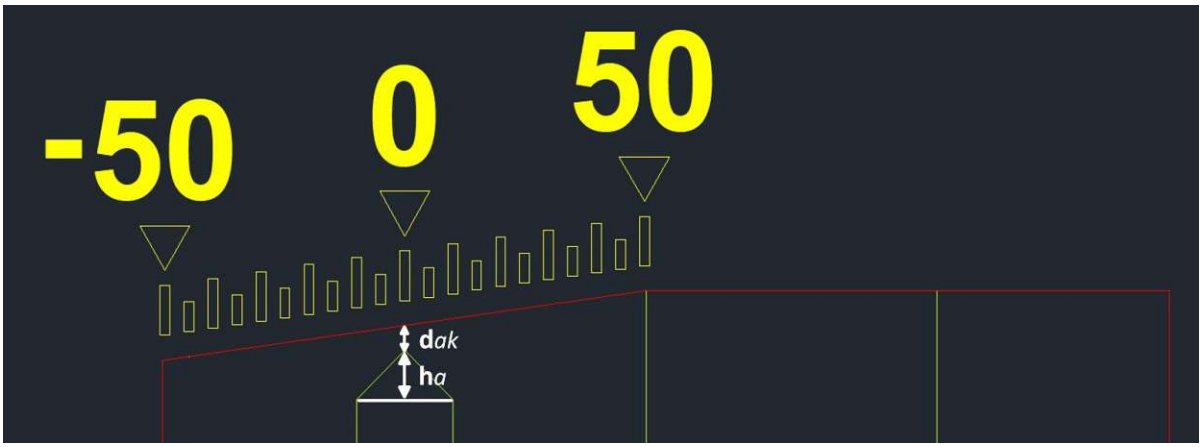

Figure 3.7: Scale used for measuring the rotation of one display beam of the smaller rotating arm test structure (L_f = 757 μm) - zoomed view.

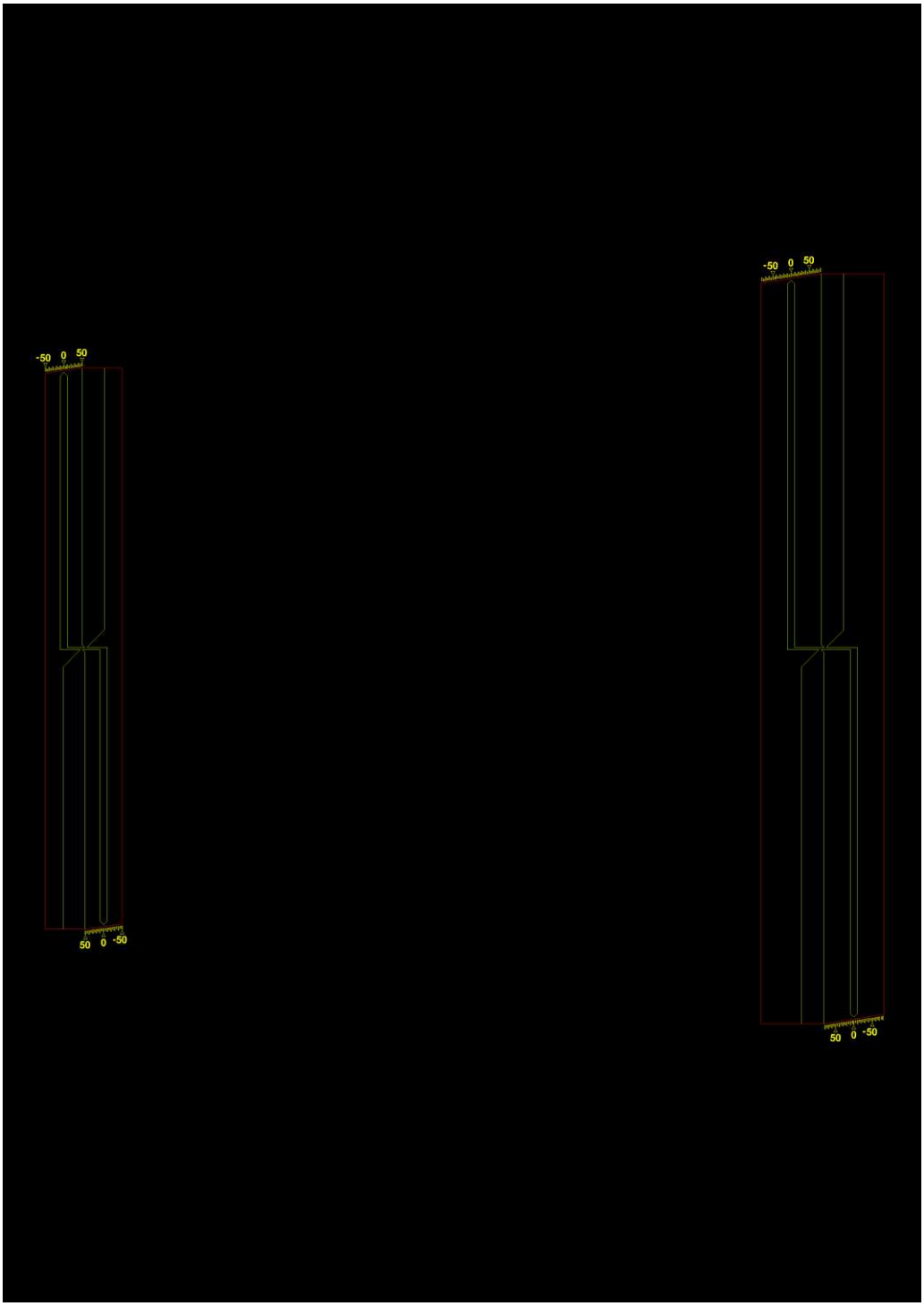

Figure 3.8: Pair of one smaller (see Figure 3.1) and one larger, straight-oriented rotating arm test structure (see Figure 3.2).

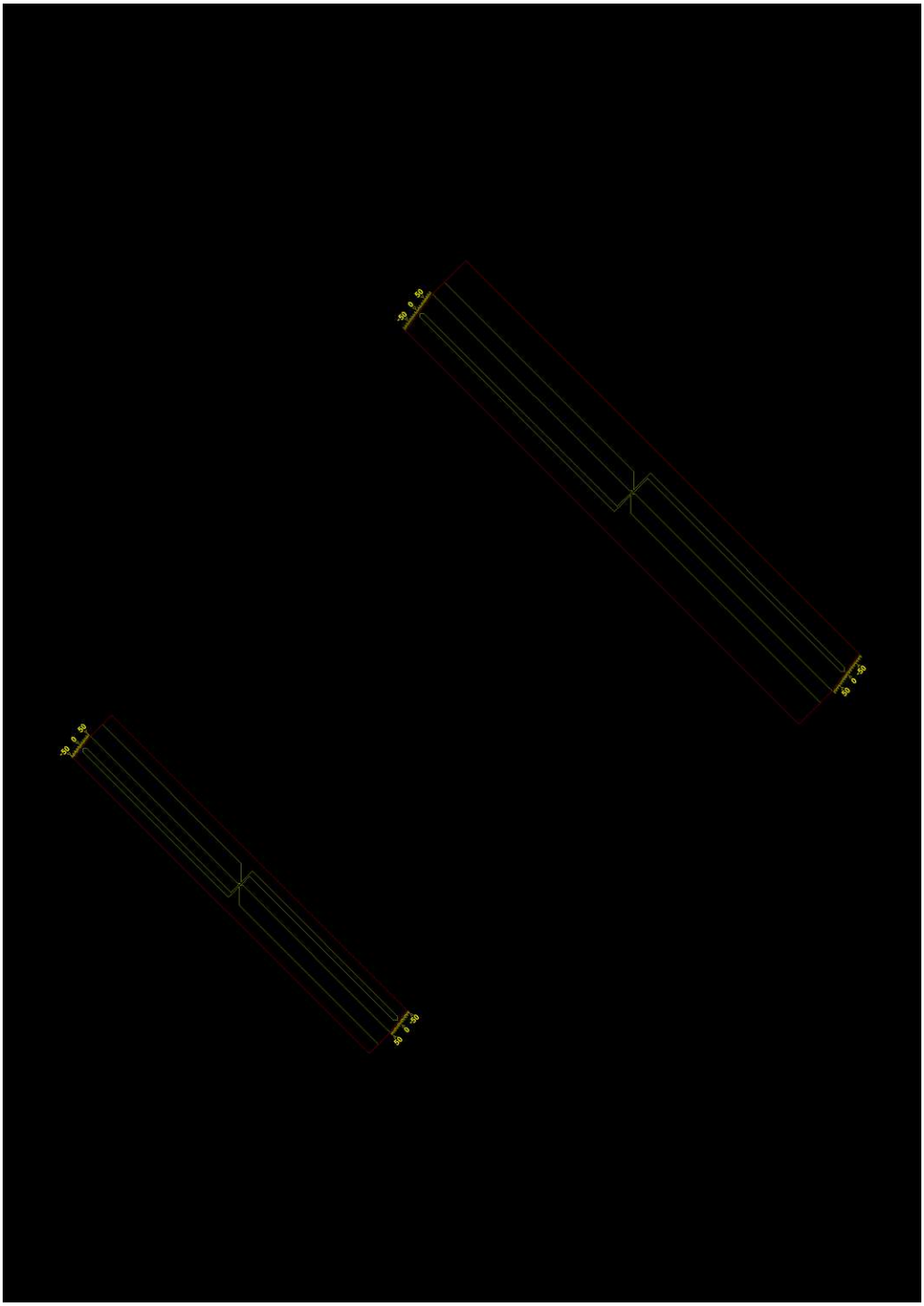

Figure 3.9: Pair of one smaller (see Figure 3.1) and one larger rotating arm test structure (see Figure 3.2) rotated by 45°.

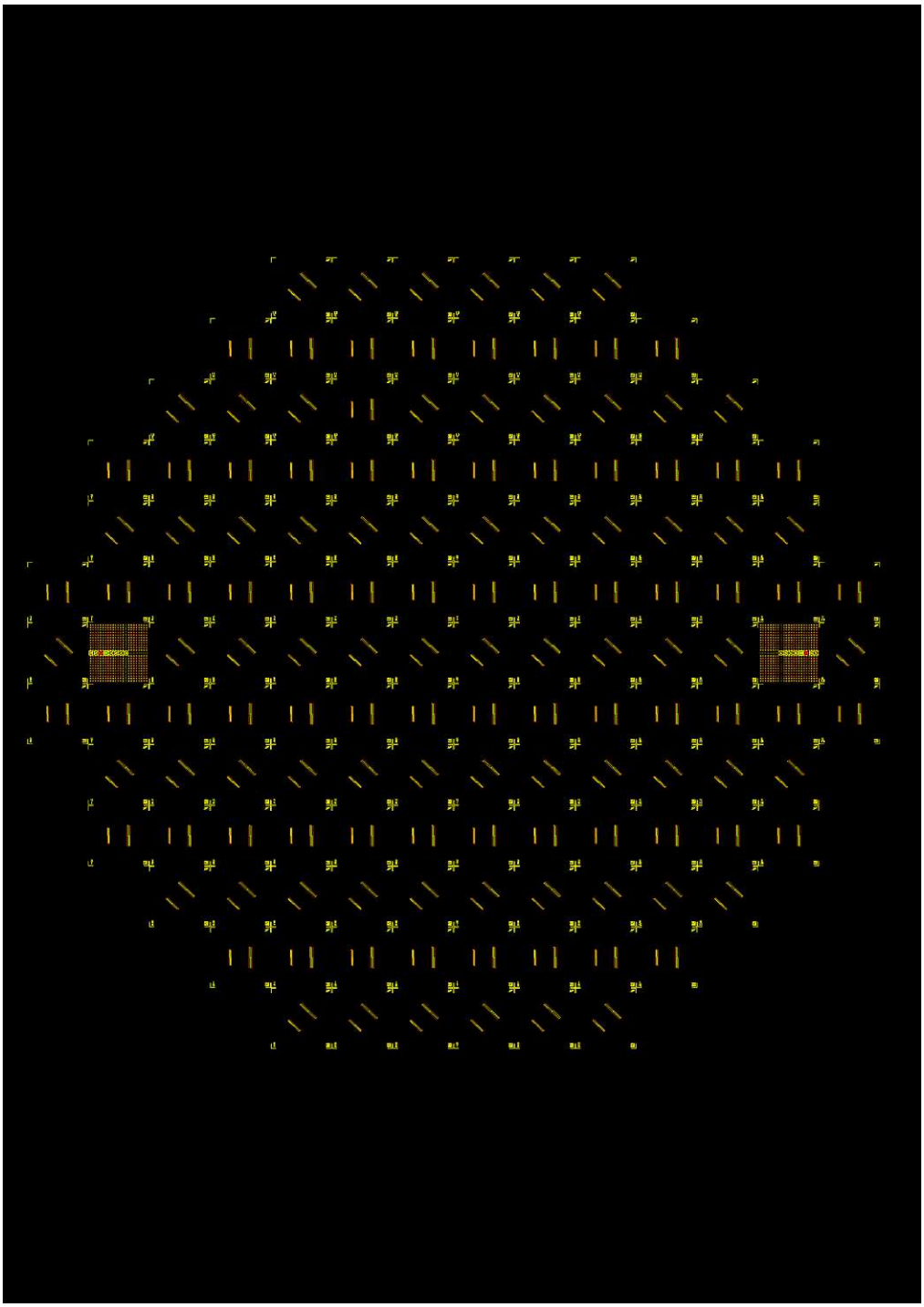

Figure 3.10: Overview of the mask design containing 69 pairs of straight-oriented rotating arm test structures (see Figure 3.8) and 67 pairs of rotating arm test structures rotated by 45° (see Figure 3.9).

3.2 Fabrication of the rotating arm test structure

The mask design containing 69 straight-oriented pairs of rotating arm test structures (see Figure 3.8) and 67 pairs of rotating arm test structures rotated by 45° (see Figure 3.9) was made out of three separate masks corresponding to the three different AUTOCAD layers: *BOTTOMELECTRODE*, *SILICONTOPSIDE*, and *SILICONBACKSIDE*.
The first mask used for fabricating the rotating arm test structure was the one designed for the *BOTTOMELECTRODE* layer. Besides the scales used for measuring the rotation of one display beam of a rotating arm test structure, as outlined in yellow in Figure 3.7, the design of this mask includes the markings, which serve as boundaries for the area reserved for the pairs of rotating arm test structures, the TU Wien and ISAS logos, the number of the pair of rotating arm test structures, as well as the two areas containing the alignment marks. For this reason, no alignment step was required before exposing the positive photoresist not covered by the mask. Next, the exposed regions of the photoresist were removed and a 20 nm thick Cr layer was evaporated. The reason for choosing evaporation instead of spin coating as a deposition method was the smoother elimination of the unexposed photoresist regions. Further, a 50 nm thick Au layer was deposited by using a Wolfram boat. Three acetone baths were used to remove the parts of the Au and Cr layers deposited on top of the photoresist and subsequently the unexposed photoresist beneath. Finally, the wafer was cleaned with isopropanol to remove any traces of acetone and baked.
The second mask used in the fabrication process of the rotating arm test structure was the one designed for the *SILICONTOPSIDE* layer. Thus, the design of this second mask includes the rotating arm test structure itself, outlined in neon green in Figure 3.1 - 3.2. Next, the alignment marks fabricated by using the first mask were used to ensure an exact alignment process of the mask on the wafer. As for the first mask, the positive photoresist areas not covered by the second mask were exposed and subsequently removed. Further, 90 cycles of Bosch etching followed by an oxygen plasma cleaning step were performed. Finally, the top side of the future rotating arm test structure was spray-coated to ensure better stability of the entire test structure.
The last used mask was the one designed for the *SILICONBACKSIDE* layer. This mask includes the frame, which surrounds the whole rotating arm test structure, outlined in red in Figure 3.1 - 3.2. The fabrication steps done while using this third mask are identical to the ones done while using the mask designed for the *SILICONTOPSIDE* layer up until the etching step. In this case, 1300 etching cycles were needed, followed by an oxygen plasma cleaning step and an HF release step. The top side of the rotating arm test structure was protected by the applied spray coat during the HF release step.

Next, the result of the described fabrication steps can be seen in Figure 3.11 for the smaller rotating arm test structure ($L_f = 757$ μm) and in Figure 3.12, which depicts the larger rotating arm test structure ($L_f = 1013$ μm). Both depicted rotating arm test structures had no thin film deposited on top of them.

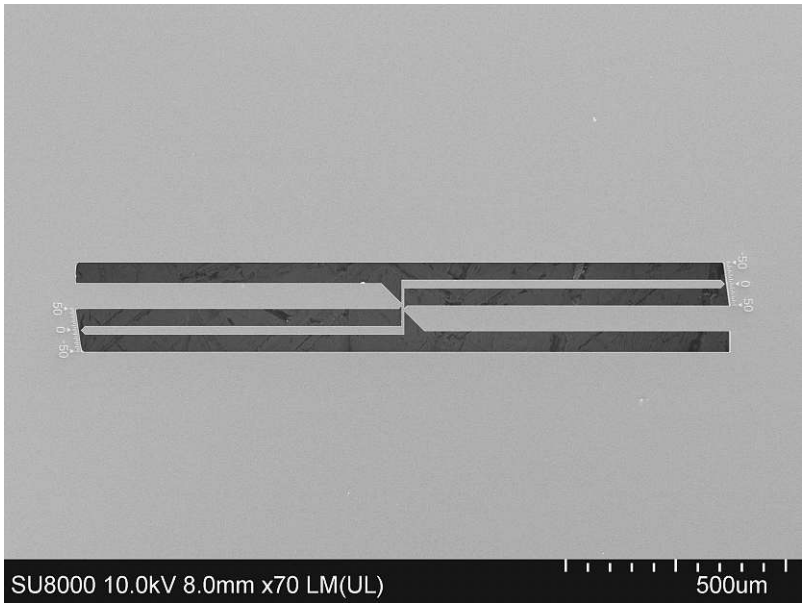

Figure 3.11: Overview of the smaller rotating arm test structure ($L_f = 757$ μm) with no mechanical stress applied (no thin film deposited on top of the rotating arm test structure). The values of the scale are expressed in μm.

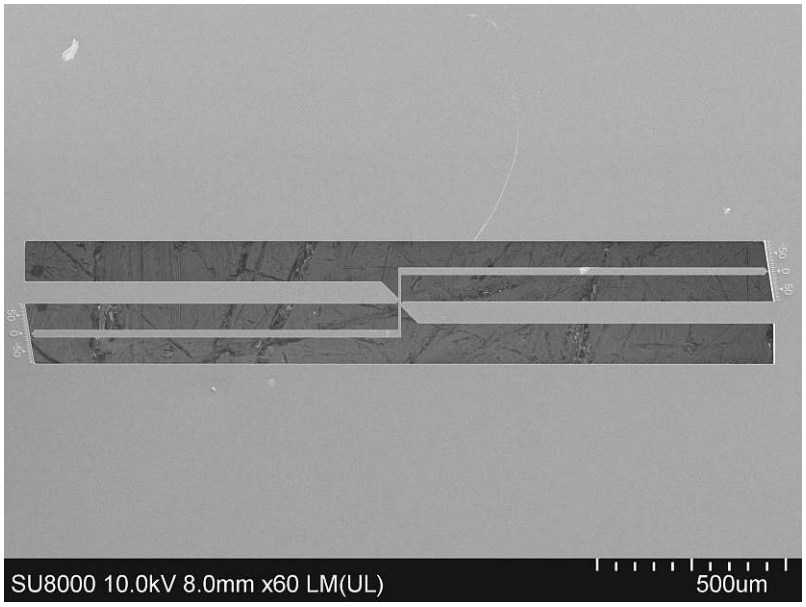

Figure 3.12: Overview of the larger rotating arm test structure ($L_f = 1013$ μm) with no mechanical stress applied (no thin film deposited on top of the rotating arm test structure). The values of the scale are expressed in μm.

The last two figures of this chapter depict imperfections of the rotating arm test structures, which occurred during the fabrication process. Figure 3.13 depicts how the angles of the central part of a rotating arm test structure are rounded and not sharp, as depicted in the corresponding AUTOCAD schematic (see Figure 3.6).

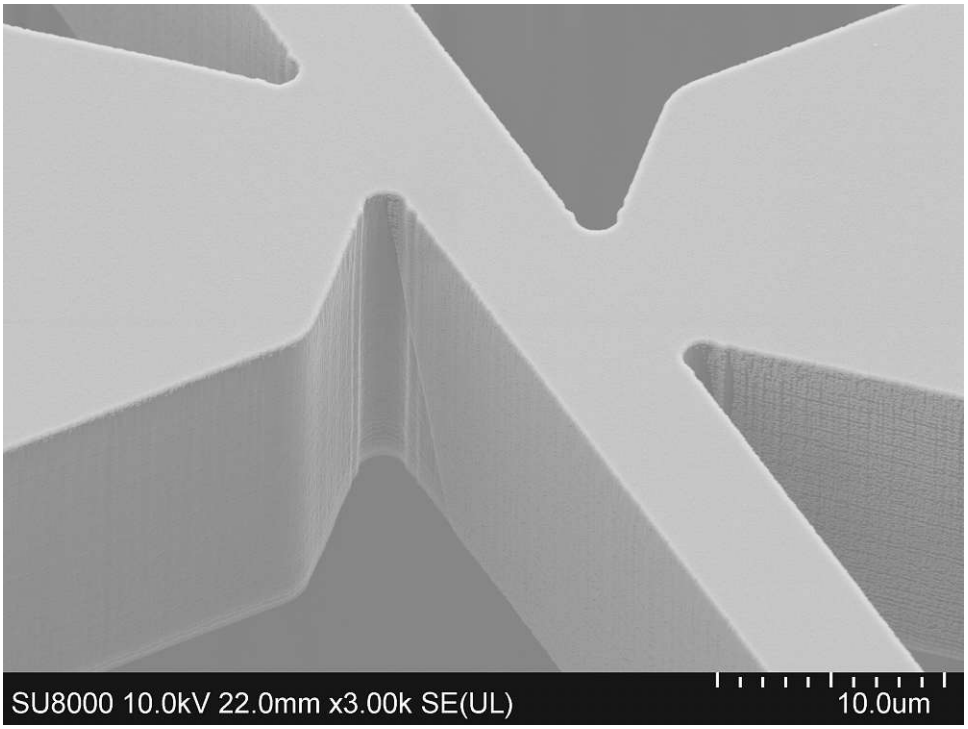

Figure 3.13: Zoomed view of the rounded angles of the central part of a rotating arm test structure with a 250 nm thick Cr thin film evaporated on top of it.

Next, Figure 3.14 shows how the right display beam of a smaller rotating arm test structure ($L_f = 757$ μm) shows a clockwise rotation directly after fabrication, without having any thin film deposited on top of it, which may indicate mechanical stress. The display beams of both the smaller and the larger rotating arm test structure show the same clockwise rotation offset of about 0.5 μm). The reason for this offset might be the existence of mechanical stress in the Si wafer itself.

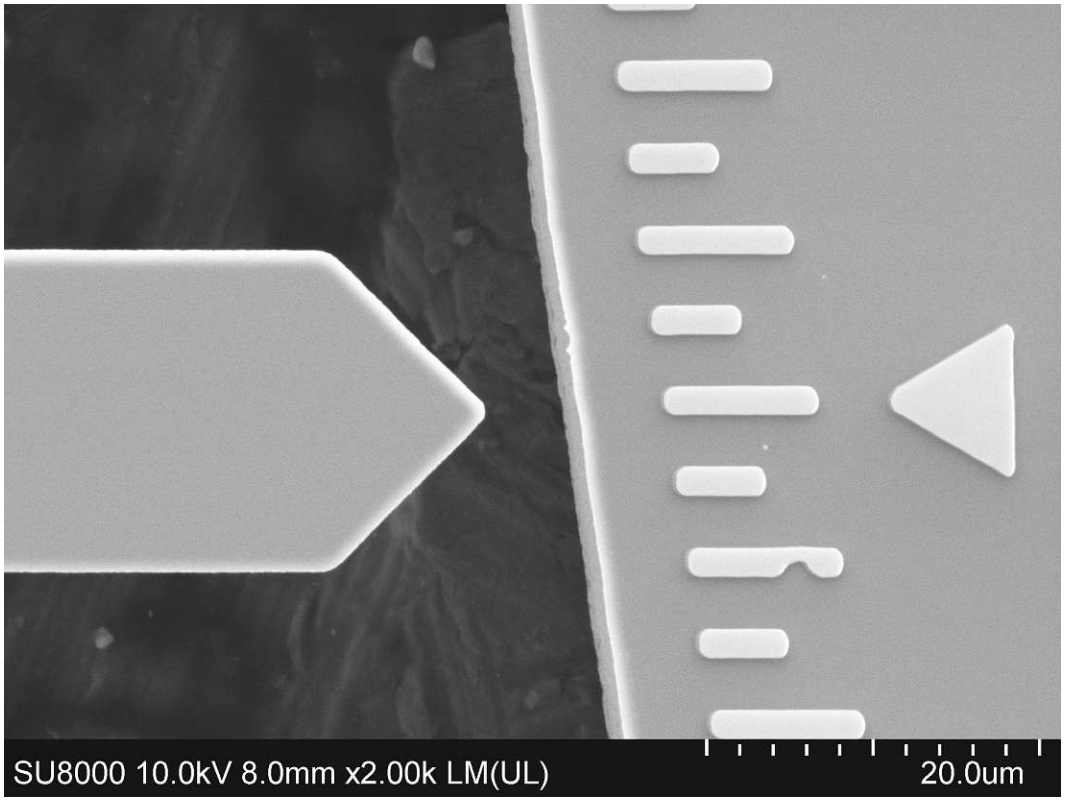

Figure 3.14: Zoomed view of the clockwise rotation of the right display beam of a smaller rotating arm test structure ($L_f = 757$ μm) with no mechanical stress applied (no thin film deposited on top of the rotating arm test structure). The distance between two markers of the scale used for measuring the rotation of the display beam is equal to 5 μm.

CHAPTER 4

Verification measurements of the rotating arm test structure

To check if the chosen rotating arm structure design fulfills its purpose successfully, several thin films with different mechanical stress levels were deposited on top of the rotating arm test structures. Further, the expected x-displacement values were compared with the ones registered during the verification measurements.
Three different deposition methods were used for the test films: plasma-enhanced chemical vapor deposition (PECVD), sputtering, and evaporation. While thin films deposited via PECVD and via evaporation exhibit homogeneously distributed mechanical stress with repeatable values, the reachable mechanical stress inside a sputtered thin film can reach values several times higher than the 600 - 700 MPa possible in the PECVD thin films. The disadvantage of the sputtered thin films is that, unlike the PECVD and the evaporated thin films, the mechanical stress differs along the thin film, and its registered values are rather unreproducible.

4.1 Measurements done on PECVD deposited thin films

First, a-SiC:H thin films were deposited by using the PECVD method. PECVD was preferred against sputtering due to its ability to deliver homogeneously stressed thin films. Although the x-displacement values from the COMSOL simulations were obtained for stress values of 1 GPa, it was expected that the films fabricated by using PECVD would be able to generate a rotation of the display beams, even for mechanical stress values of just 600 - 700 MPa.
To verify the mechanical stress value of a thin film deposited by using the PECVD method and a specific set of process parameters, such a thin film was first deposited on a blank wafer, without any rotating arm test structure on it. A mechanical stress value of

around 600 - 700 MPa was measured by using the wafer curvature stress measurement method for the PECVD-deposited, 500 nm thick a-SiC:H thin film. Next, 125 nm, 250 nm, and 375 nm thick a-SiC:H thin films were deposited on top of two straight-oriented rotating arm test structures and on top of two rotating arm test structures rotated by 45°. Both the straight-oriented and the rotating arm test structures rotated by 45° were always fabricated as a pair composed of a smaller structure, with $L_f = 757$ μm, and of a larger one, with $L_f = 1013$ μm (see Figure 3.8 - 3.9). At the same time, the remainder of the PECVD process parameters remained unchanged. As the mechanical stress in PECVD-deposited thin films is homogeneous, it was assured that the 125, 250, and 375 nm a-SiC:H thin films possess the same values of mechanical stress [20].
Figure 4.1, 4.2, 4.3, and 4.4 depict the rotation of the display beams part of straight-oriented rotating arm test structures as a response to the mechanically stressed 250 nm and 375 nm a-SiC:H thin films. While the rotation of the display beam with a 125 nm a-SiC:H thin film on top of it is too low to be considered a confirmation that the rotating arm test structure works as expected, the rotation of the display beams coated with 250 and 375 nm a-SiC:H thin films may be taken as evidence that the rotating arm test structure behaves as expected after the COMSOL simulations. A similar, but proportional to the increased thickness, rotational movement was expected to occur for the display beams covered with a 500 nm a-SiC:H thin film. For this reason, together with the stability problems encountered during the PECVD deposition, such a 500 nm a-SiC:H thin film was not deposited on top of any rotating arm test structure. As expected, the larger rotating arm test structure, with $L_f = 1013$ μm, registers a higher rotation of the display beam (see Figure 4.2 and Figure 4.4) than the smaller rotating arm test structure (see Figure 4.1 and Figure 4.3), with $L_f = 757$ μm. The x-displacements displayed in Figure 4.1 - 4.4, together with the approximate values of the expected x-displacements, for both dimensions of the rotating arm structures are summarised in Table 4.1 for both the 250 nm and the 375 nm a-SiC:H thin films.

Thin film	Test structure	right x-displ.	expected x-displ.
250 nm a-SiC:H	$L_f = 757$ μm	1 μm	1.625 μm
375 nm a-SiC:H	$L_f = 757$ μm	1.5 μm	2.4375 μm
250 nm a-SiC:H	$L_f = 1013$ μm	2.5 μm	2.925 μm
375 nm a-SiC:H	$L_f = 1013$ μm	2.5 μm	4.3875 μm

Table 4.1: Overview of the measured and expected x-displacements displayed by the rotation of the right display beams of both straight-oriented rotating arm structures, coated with 250 nm and the 375 nm a-SiC:H thin films (see Figure 4.1 - 4.4).

The expected x-displacements from Table 4.1 were calculated for both straight-oriented rotating arm test structures, coated with th 250 nm a-SiC:H thin film, by using the following formula:

expected x-displacement = 0.65 × 0.25 × highest x-displacement registered at Point 20

where the highest x-displacement registered at Point 20 (see Figure 2.4) was read from the colour scale of Figure 2.8, as 10 μm, for the rotating arm test structure with $L_f = 757$ μm and from the colour scale of Figure 2.9, as 18 μm, for the rotating arm test structure with $L_f = 1013$ μm. These highest x-displacements registered at Point 20 (see Figure 2.4) were obtained by simulating a stress of 1 GPa homogeneously distributed along a 1 μm thick Si layer, placed on top of the layer containing the rotating arm test structure. Thus, these simulated x-displacements were multiplied with 0.65, as the deposited a-SiC:H thin film has a stress of around 600 - 700 MPa compared to the simulated 1 GPa and with 0.25, as the deposited a-SiC:H layer is only 250 nm thick compared to the 1 μm used in the simulations, for obtaining an approximate value of the expected x-displacement. The type of mechanical stress is not considered in this formula, therefore the calculated x-displacements are to be considered as absolute values.

The algebraic signs of the right and left x-displacements listed in Table 4.1, Table 4.3, Table 4.4, Table 4.5, and Table 4.6 are chosen according to the scales fabricated near the right and left display beam and are defined in Table 4.2:

Direction of rotational movement of the display beam	Corresponding algebraic sign
clockwise rotation	+
counterclockwise rotation	-

Table 4.2: Overview of the algebraic signs of the right and left x-displacements.

The same formula used for calculating the expected x-displacements for both straight-oriented rotating arm test structures, coated with the 250 nm a-SiC:H thin film, was adapted for approximating the x-displacements expected to occur for both straight-oriented rotating arm test structures, coated with the 375 nm a-SiC:H thin film (see Table 4.1):

expected x-displacement = 0.65 $\times$ 0.375 $\times$ highest x-displacement registered at Point 20

The only difference is the factor 0.375 used instead of 0.25 as a consequence of the increased thickness (375 nm) of the second analysed a-SiC:H thin film.

After considering the human error introduced in the measurement chain when reading the rotation of the display beams from Figure 4.1 - 4.4, the following conclusion can be drawn: the measured x-displacements of the smaller, straight-oriented rotating arm test structures, covered with the 250 nm and the 375 nm a-SiC:H thin films, and of the larger, straight-oriented rotating arm test structure, covered with the 375 nm a-SiC:H thin film represent around 60 % of the expected x-displacement. Further, the straight-oriented rotating arm test structure with $L_f = 1013$ μm coated with the 250 nm a-SiC:H thin film appears to measure the stress better than the other three structures, as the ratio between the measured and the expected x-displacement is 85.5 %.

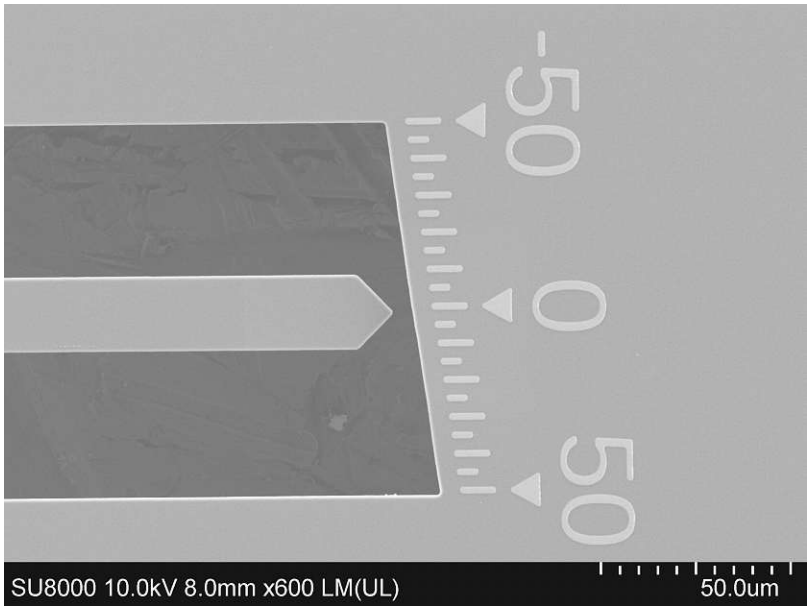

Figure 4.1: Rotation of the right display beam, part of the smaller, straight-oriented rotating arm test structure ($L_f = 757$ μm), in response to the 250 nm a-SiC:H thin film PECVD-deposited on top of it. The values of the scale are expressed in μm.

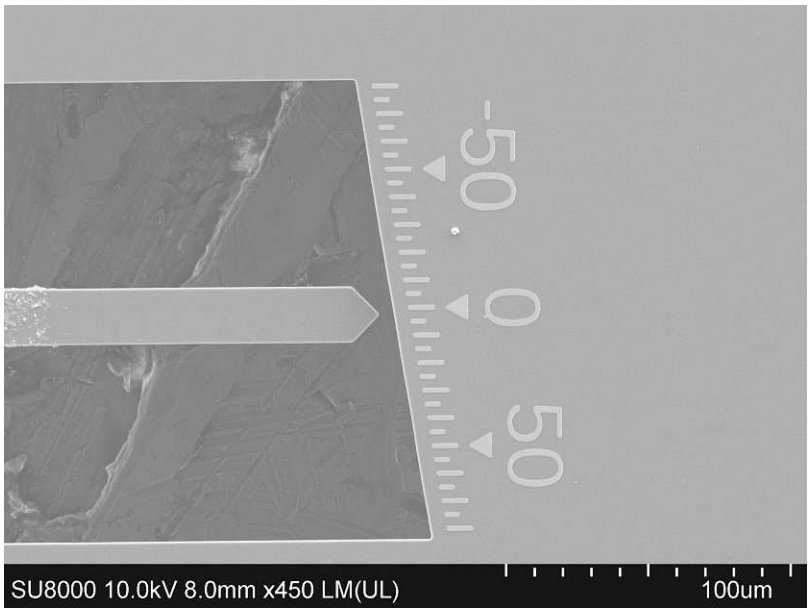

Figure 4.2: Rotation of the right display beam, part of the larger, straight-oriented rotating arm test structure ($L_f = 1013$ μm), in response to the 250 nm a-SiC:H thin film PECVD-deposited on top of it. The values of the scale are expressed in μm.

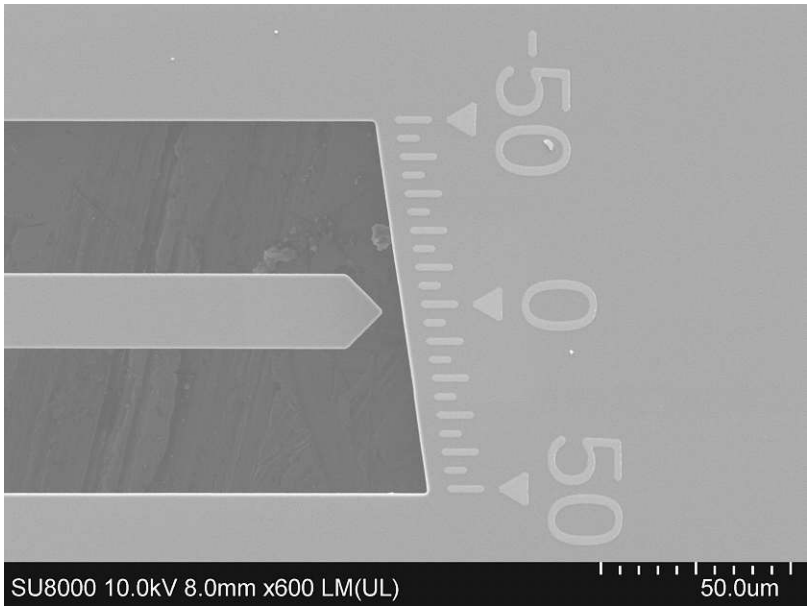

Figure 4.3: Rotation of the right display beam, part of the smaller, straight-oriented rotating arm test structure ($L_f = 757$ μm), in response to the 375 nm a-SiC:H thin film PECVD-deposited on top of it. The values of the scale are expressed in μm.

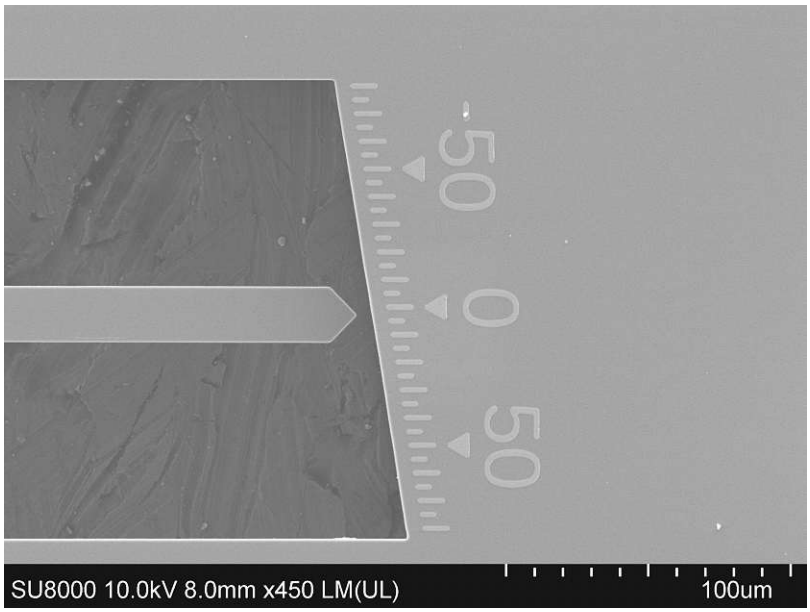

Figure 4.4: Rotation of the right display beam, part of the larger, straight-oriented rotating arm test structure ($L_f = 1013$ μm), in response to the 375 nm a-SiC:H thin film PECVD-deposited on top of it. The values of the scale are expressed in μm.

The direction of rotational movement of the display beams is the main criterion used to evaluate if the rotating arm test structure functions correctly or not. This direction is depicted in Figure 4.5 for the right display beam, part of the larger, straight-oriented rotating arm test structure coated with the 375nm a-SiC:H thin film, already depicted in Figure 4.4, and for the opposite, left display beam of the same test structure in Figure 4.6. Due to the design of the rotating arm test structure, the correct functioning of such a device implies the same clockwise or counterclockwise rotation of both display beams of each structure. This kind of behaviour was observed for the larger, straight-oriented rotating arm test structure covered with the 375nm a-SiC:H thin film: both display beams, as depicted in Figure 4.5 and Figure 4.6, rotate clockwise and with the same extent.

The rotation of the display beams of the larger, rotating arm test structure rotated by 45°, coated with the 375 nm a-SiC:H thin film, was also analysed. The same behaviour as for the larger, straight-oriented rotating arm test structure, coated with the same 375 nm a-SiC:H thin film, could be observed: both the right display beam, depicted in Figure 4.7, and the left display beam, depicted in Figure 4.8, rotate clockwise and with the same extent. Further, the x-displacement values of this structure rotated by 45° (see Figure 4.7 - 4.8) are equal to the ones read from Figure 4.5 - 4.6, which are the response of the same larger rotating arm test structure, covered with the same stressed a-SiC:H thin film, but straight-oriented. Thus, it can be concluded that the larger rotating arm test structure rotated by 45° behaves identically to the larger, straight-oriented rotating arm test structure.

Figure 4.9 - 4.10 depict a drawback of this rotating arm structure design: its out-of-plane deflection. This undesired effect can be observed at the ends of the display beams, which incline downwards, presumably in response to compressive mechanical stress, instead of staying in the same plane with the rest of the rotating arm test structure. Although out-of-plane deflection was also observed during the COMSOL simulations, as depicted in Figures 2.15 - 2.16, done for the simplified design (see Figure 2.1), the design updates, included in the improved AUTOCAD design of the rotating arm test structures (see Figure 3.1-3.2), were not able to eliminate this drawback.
Under these circumstances, the equality between the measured x-displacement value of the larger, straight-oriented rotating arm test structure, coated with the 250 nm a-SiC:H thin film and of the one of an identical device coated with the 375 nm a-SiC:H thin film, as listed in Table 4.1, is considered to be rather a consequence of a reading error caused by the downwards deflection of the display beams of the latter device, than a proof that a 375 nm a-SiC:H thin film induces the same x-displacement as a 250 nm a-SiC:H thin film.

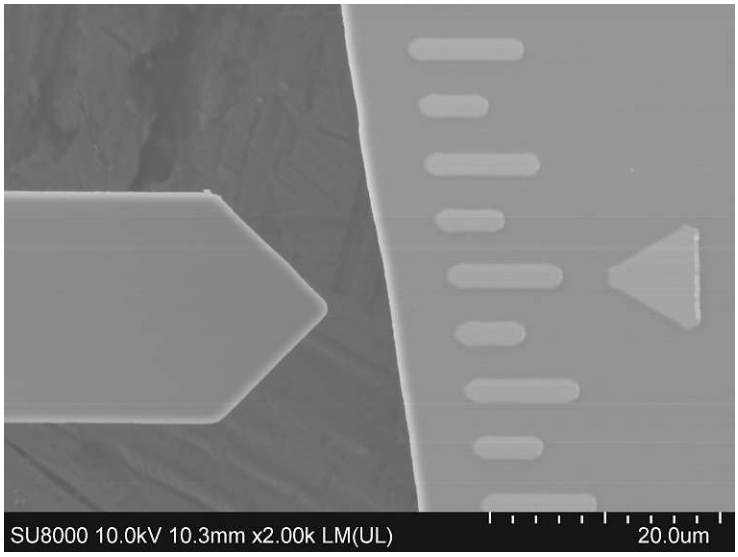

Figure 4.5: Rotation of the right display beam, part of the larger, straight-oriented rotating arm test structure ($L_f = 1013$ μm), in response to the 375 nm a-SiC:H thin film PECVD-deposited on top of it - zoomed view. The distance between two markers of the scale used for measuring the rotation of the display beam is equal to 5 μm.

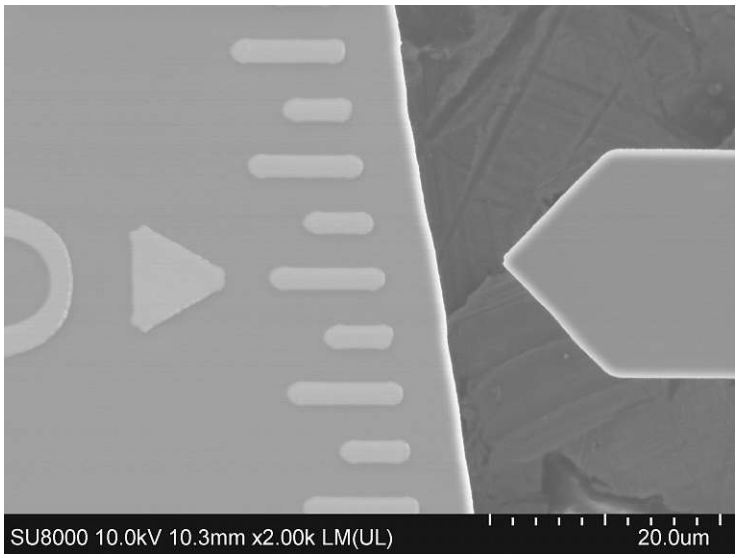

Figure 4.6: Rotation of the (opposite) left display beam, part of the larger, straight-oriented rotating arm test structure ($L_f = 1013$ μm), in response to the 375 nm a-SiC:H thin film PECVD-deposited on top of it - zoomed view. The distance between two markers of the scale used for measuring the rotation of the display beam is equal to 5 μm.

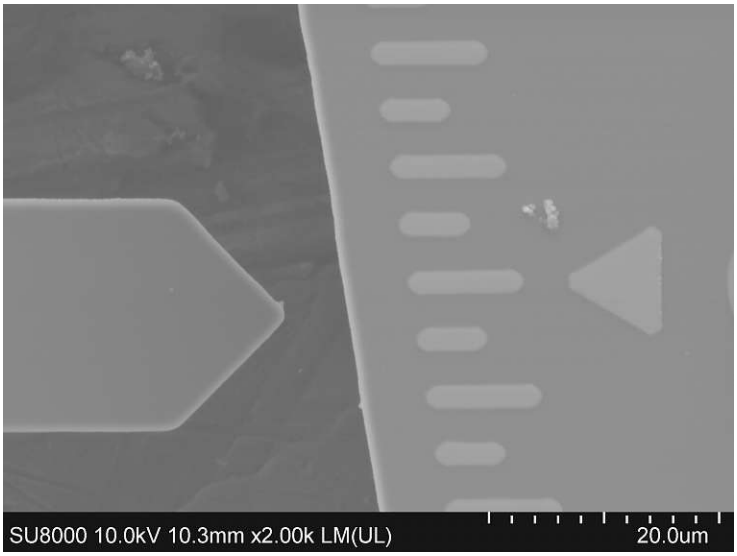

Figure 4.7: Rotation of the right display beam, part of the larger rotating arm test structure ($L_f = 1013$ μm) rotated by 45°, in response to the 375 nm a-SiC:H thin film PECVD-deposited on top of it - zoomed view. The distance between two markers of the scale used for measuring the rotation of the display beam is equal to 5 μm.

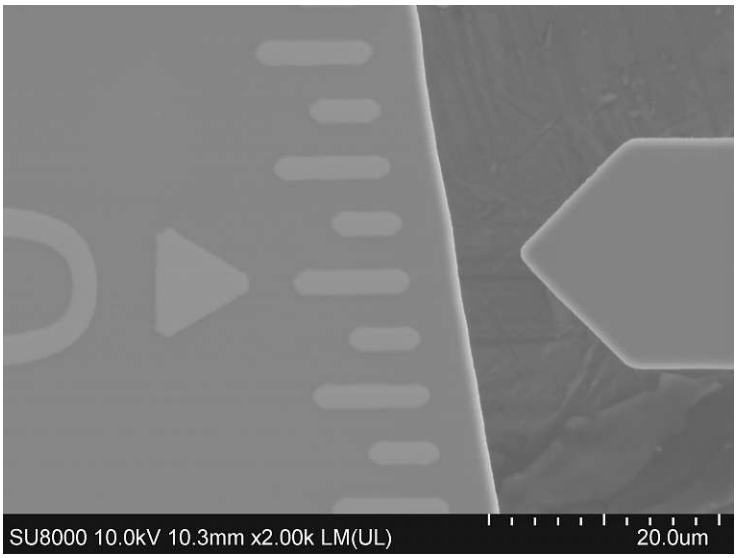

Figure 4.8: Rotation of the (opposite) left display beam, part of the larger rotating arm test structure ($L_f = 1013$ μm) rotated by 45°, in response to the 375 nm a-SiC:H thin film PECVD-deposited on top of it - zoomed view. The distance between two markers of the scale used for measuring the rotation of the display beam is equal to 5 μm.

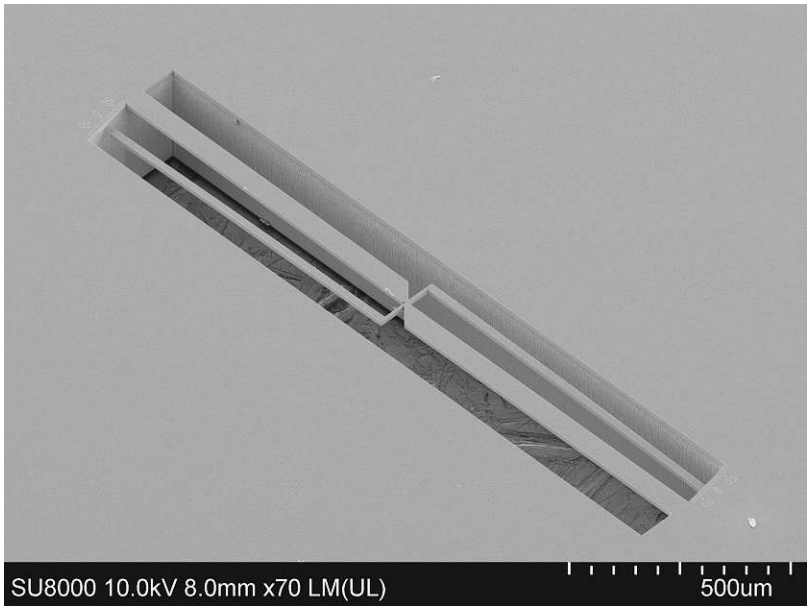

Figure 4.9: Out-of-plane deflection observable for both display beams, part of the larger rotating arm test structure ($L_f = 1013$ μm) rotated by 45°, in response to the 375 nm a-SiC:H thin film PECVD-deposited on top of it - top view

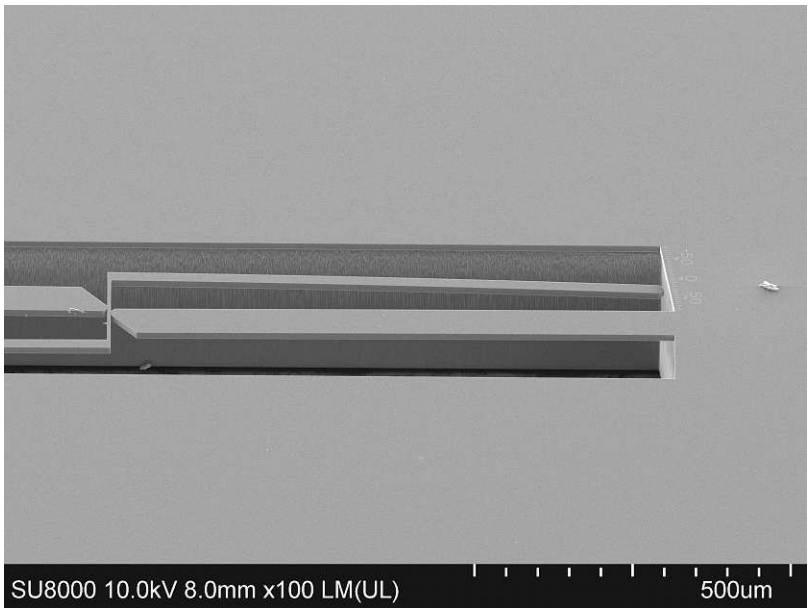

Figure 4.10: Out-of-plane deflection observable for the right display beam, part of the larger rotating arm test structure ($L_f = 1013$ μm) rotated by 45°, in response to the 375 nm a-SiC:H thin film PECVD-deposited on top of it - zoomed view

4.2 Measurements done on sputtered thin films

Aiming to generate an increased rotation of the display beams, several metallic thin films were sputtered on top of straight-oriented and by 45° rotated rotating arm test structures. It was expected to reach larger stress values than the 600 - 700 MPa, registered in the case of the PECVD-deposited a-SiC:H thin films, by using sputtering instead of PECVD as a deposition method.
As the mechanical stress differs along a sputtered thin film, three pairs of straight-oriented rotating arm test structures were placed at approximately equal distances from the middle to the edge of a wafer, which acted as a mount for the test structures. Another pair of rotating arm test structures rotated by 45° was placed centrally on the wafer, near the central pair of straight-oriented rotating arm test structures. Each pair of rotating arm structures (see Figure 3.8 - 3.9) was composed of a smaller structure, with $L_f = 757$ μm, and of a larger one, with $L_f = 1013$ μm. In this way, the broader range of stress values contained in the sputtered thin films could trigger an increased rotation of at least one pair of rotating arm test structures.
The average mechanical stress value of such a sputtered thin film was measured by applying the wafer curvature stress measurement method on the wafer, which acted as a mount for the pairs of rotating arm test structures. Five different thin films were sputtered on such a setup made out of the four pairs of rotating arm structures, mounted on a wafer: one 500 nm and one 1000 nm thick AlN thin films, another two 500 nm and 1000 nm thick Pt thin films, while only one 500 nm thick Ti thin film. While all four AlN and Pt thin films sputtered on the wafer serving as a mount exhibited average mechanical stress values similar to the one of mechanical stress homogeneously distributed along the PECVD-deposited a-SiC:H thin films, the 500 nm thick Ti thin film reached only an average mechanical stress value of 70 MPa. Doubling the thickness of such a thin film would have just presumably doubled the average mechanical stress up to a value still five times smaller than the ones reached by the other PECVD-deposited or sputtered thin films. Thus, no 1000 nm thick Ti thin film was sputtered on any rotating arm test structure.

Next, Table 4.3 gives an overview of the measured and expected x-displacements displayed by the rotation of both display beams of the straight-oriented rotating arm test structures, located at the edge of the wafer acting as a mount, beneath the 500 nm (shortened as: edge 500 nm Pt straight-oriented rotating arm test structures) and 1000 nm Pt thin films (shortened as: edge 1000 nm Pt straight-oriented rotating arm test structures).

Thin film	Test structure	right x-displ.	left x-displ.	expected x-displ.
500 nm Pt	$L_f = 1013$ μm	-3 μm	4.5 μm	5.85 μm
1000 nm Pt	$L_f = 1013$ μm	5 μm	-11 μm	11.7 μm
1000 nm Pt	$L_f = 757$ μm	2 μm	-5 μm	6.5 μm

Table 4.3: Overview of the measured and expected x-displacements displayed by the rotation of both display beams of the straight-oriented rotating arm test structures, located at the edge of the wafer acting as a mount, beneath the 500 nm and 1000 nm Pt thin films. The SEM pictures corresponding to the measured x-displacements can be found in the Supplementary material part of this diploma thesis.

The same formula used for calculating the expected x-displacements for all rotating arm test structures coated with a-SiC:H thin films (see Table 4.1) was adapted for approximating the x-displacement expected to occur for the larger, edge 500 nm Pt straight-oriented rotating arm test structure (see Table 4.3):

expected x-displacement = 0.65 $\times$ 0.5 $\times$ highest x-displacement registered at Point 20

The only difference is the factor 0.5 used instead of 0.25, as a consequence of the 500 nm thickness of the 500 nm Pt thin film. This formula used for calculating the expected x-displacements is less accurate when used for sputtered instead of PECVD-deposited thin films. Contrary to the homogeneously distributed mechanical stress in the case of PECVD-deposited thin films, the mechanical stress differs along sputtered thin films. Despite knowing about these stress heterogeneities, the location of the rotating arm test structures pairs on the wafer acting as a mount is not considered in the calculation of the expected x-displacement, because only the average mechanical stress on this whole wafer acting as a mount was measured.
The ratio between the measured and the expected x-displacement for both display beams of this particular rotating arm test structure brings no value and will be therefore not further analysed, because the right display beam shows a different rotational movement than the left display beam. Next, the different extent to which the display beams rotate, together with their opposite directions of rotational movement, lead to the conclusion that the larger, edge 500 nm Pt straight-oriented rotating arm structure does not show its simulated behaviour. A reason for this unexpected behaviour may be given by the partial coverage of the side walls of the rotating arm test structures, which represents an undesired consequence of the sputtering process. In comparison, when depositing thin films

by using PECVD, the side walls of the rotating arm test structures are completely covered.

The x-displacement values registered by the rotating arm structures in response to the sputtering of a 500 nm thick Pt thin film on top of them were higher than the ones of the rotating arm structures covered with PECVD-deposited a-SiC:H thin films. Therefore, a 1000 nm thick Pt thin film was sputtered onto another four pairs of rotating arm test structures, arranged identically on the wafer acting as a mount, as for the sputtering of the 500 nm Pt thin film.
The same formula used for calculating the expected x-displacements for the edge 500 nm Pt straight-oriented rotating arm test structures was adapted for approximating the x-displacements expected to occur for the edge 1000 nm Pt straight-oriented rotating arm test structures (see Table 4.3):

$$\text{expected x-displacement} = 0.65 \times 1 \times \text{highest x-displacement registered at Point 20}$$

The only difference is the factor 1 used instead of 0.5, as a consequence of the increased thickness (1000 nm) of the second analysed Pt thin film. Despite doubling the thickness, the average mechanical stress value, measured on the wafer acting as a mount during the sputtering of the 1000 nm Pt thin film, is equal to the mechanical stress value measured on the wafer acting as a mount during the sputtering of the 500 nm Pt thin film: around 600 - 700 MPa.

According to Table 4.3, both the smaller and the larger, edge 1000 nm Pt straight-oriented rotating arm test structures behave identically to the larger, edge 500 nm Pt straight-oriented rotating arm structure: they do not show their simulated behaviour, which implies that the ratios between the measured and the expected x-displacement of both display beams of these particular edge 1000 nm Pt rotating arm test structures bring no value and will be therefore not further analysed. However, something worth mentioning can be observed in Table 4.3: the measured x-displacements of the left display beams of both smaller and larger rotating arm structure are more than twice higher than the corresponding values of the right display beams, and show a 50 % better match with the expected x-displacements.

The drawback of the larger rotating arm test structure (L_f = 1013 μm) rotated by 45°, coated with the PECVD-deposited 375 nm a-SiC:H thin film (see Figure 4.9 - 4.10), is similarly present for the larger, edge 1000 nm Pt straight-oriented rotating arm test structure. In this case, Figure 4.11 depicts the upward inclination observable at the ends of the display beams. Such an out-of-plane deflection appears as a consequence of the tensile mechanical stress present in the 1000 nm thick Pt thin film, sputtered on top of the rotating arm test structure. Further, another consequence of such tensile mechanical stress is the counterclockwise rotation of the left display beams, interpreted as negative x-displacements (see Table 4.3). By following the same logic, the compressive mechanical stress present in the 375 nm thick a-SiC:H thin film leads to the downward inclination of

the ends of the display beams, as depicted in Figure 4.9 - 4.10. As the larger rotating arm test structure (L_f = 1013 μm) rotated by 45°, covered with the PECVD-deposited 375 nm a-SiC:H thin film (see Figure 4.9 - 4.10), shows its simulated behaviour and the x-displacements are interpreted as positive for both the right and the left display beam, a clockwise rotational movement of the display beams may be considered as a consequence of compressive mechanical stress.
The zoomed view of the out-of-plane deflection of the left display beam, part of the larger, edge 1000 nm Pt straight-oriented rotating arm test structure (L_f = 1013 μm), depicted in Figure 4.12, serves as an evidence of the proneness towards human error to be considered regarding the measured x-displacements. Although the rotational movement of the display beam depicted in Figure 4.12 was interpreted as an x-displacement equal to 94 % of the expected x-displacement (according to the values from Table 4.3), its upward inclination may alter the reading of the measured x-displacement.

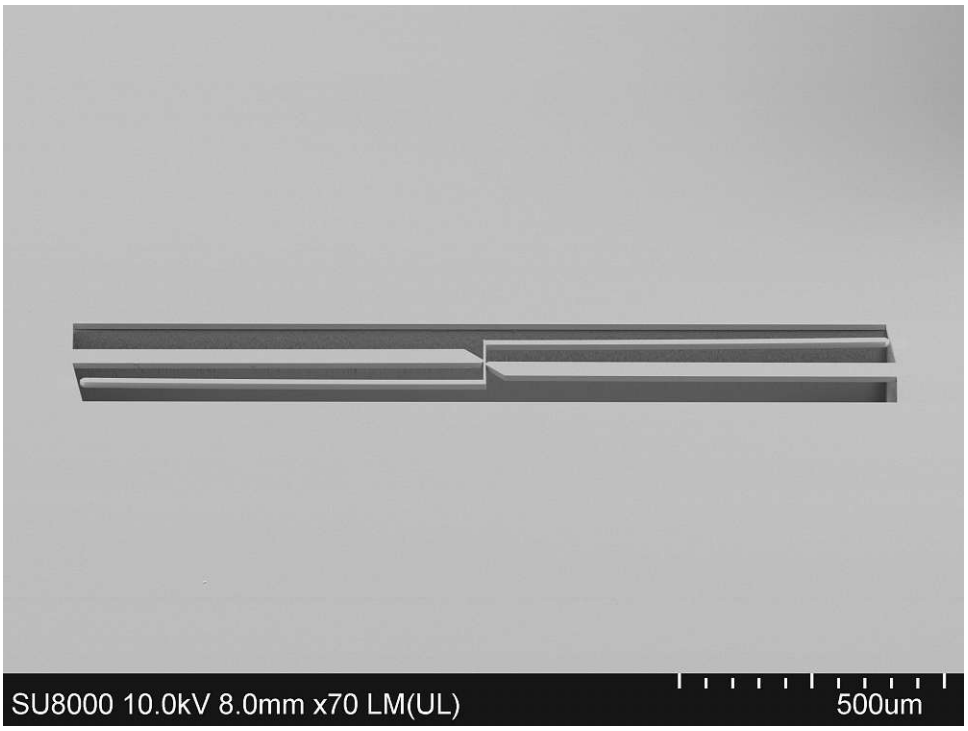

Figure 4.11: Out-of-plane deflection observable for both display beams, part of the larger, straight-oriented rotating arm test structure (L_f = 1013 μm), located at the edge of the wafer acting as a mount, in response to the 1000 nm Pt thin film sputtered on top of it - top view.

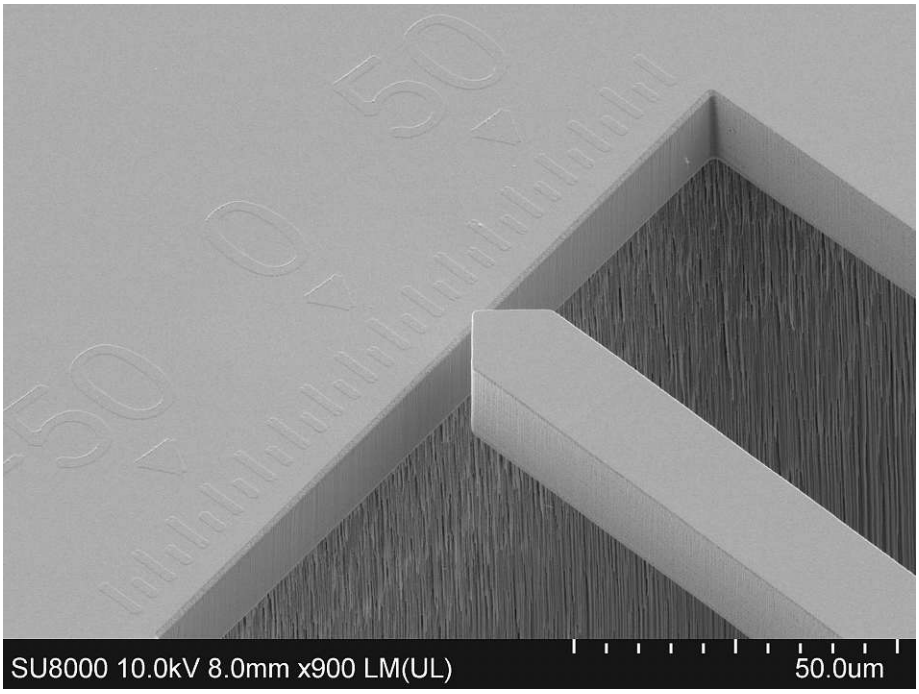

Figure 4.12: Out-of-plane deflection observable for the left display beam, part of the larger, straight-oriented rotating arm test structure (L_f = 1013 μm), located at the edge of the wafer acting as a mount, in response to the 1000 nm Pt thin film sputtered on top of it - zoomed view.

Next, Table 4.4 gives an overview of the measured and expected x-displacements displayed by the rotation of both display beams of the larger rotating arm test structures (L_f = 1013 μm) rotated by 45°, located centrally on the wafer acting as a mount, beneath the 1000 nm Pt (shortened as: central 1000 nm Pt rotating arm test structure rotated by 45°) and 500 nm AlN thin films (shortened as: central 500 nm AlN rotating arm test structure rotated by 45°).

Thin film	Test structure	right x-displ.	left x-displ.	expected x-displ.
1000 nm Pt	L_f = 1013 μm	0.5 μm	3 μm	11.7 μm
500 nm AlN	L_f = 1013 μm	4 μm	0.5 μm	5.85 μm

Table 4.4: Overview of the measured and expected x-displacements displayed by the rotation of both display beams, part of the larger, central 1000 nm Pt and 500 nm AlN rotating arm test structures rotated by 45°. The SEM pictures corresponding to the measured x-displacements can be found in the Supplementary material part of this diploma thesis.

For approximating the x-displacements expected to occur for the central 1000 nm Pt rotating arm test structure rotated by 45° (see Table 4.4), the same formula as for

the expected x-displacements of the edge 1000 nm Pt straight-oriented rotating arm test structures was used:

$$\text{expected x-displacement} = 0.65 \times 1 \times \text{highest x-displacement registered at Point 20}$$

As already mentioned, this formula does not consider the location of the pair of rotating arm structures on the wafer acting as a mount when calculating the expected x-displacement. After analysing the measured, right and left x-displacements of the rotating arm test structures, located at the edge of the wafer acting as a mount (see Table 4.3), and the ones of the rotating arm test structures, located centrally on the wafer acting as a mount (see Table 4.4), while assuming that a higher rotational movement occurs due to higher mechanical stress, it may be concluded that the mechanical stress of the Pt thin film region near the edge of the wafer serving as a mount is higher than the one of the central region of the same thin film.
As for the edge 1000 nm Pt straight-oriented rotating arm test structures (see Table 4.3), the right display beam of the larger, central 1000 nm Pt rotating arm test structure rotated by 45° shows a different rotational movement than its left display beam (see Table 4.4). Thus, this device behaves like the other ones covered by Pt thin films and does not show its simulated behaviour.
The following behaviour is rather unexpected and therefore worth to mention: while the left display beam of the larger, straight-oriented rotating arm test structures, located at the edge of the wafer acting as a mount (see Table 4.3) rotates counterclockwise, the left display beam of the larger rotating arm test structure rotated by 45°, located centrally on the wafer acting as a mount (see Table 4.4) rotates clockwise, even though both rotating arm structures are covered by the same 1000 nm thick Pt thin film.

To research the response triggered by a thin film sputtered from a different material, AlN was sputtered onto another four pairs of rotating arm test structures, arranged identically on the wafer acting as a mount, as for the sputtering of the 500 nm and 1000 nm Pt thin films.
The same formula used for calculating the expected x-displacements for the straight-oriented rotating arm test structures, coated with the 500 nm Pt thin film, was used for approximating the x-displacements expected to occur for the rotating arm test structures covered with the 500 nm AlN thin film (see Table 4.4):

$$\text{expected x-displacement} = 0.65 \times 0.5 \times \text{highest x-displacement registered at Point 20}$$

The same average mechanical stress of around 600 - 700 MPa was measured on both wafers acting as a mount, used for the sputtering of the 500 nm Pt thin film and the sputtering of the 500 nm AlN thin film, respectively. This similarity provides an advantage for analysing how the specific material used for sputtering the thin films impacts the behaviour of the rotating arm test structures.

According to Table 4.4, the display beams show a different rotational movement in both extent and direction. Thus, the larger, central 500 nm AlN rotating arm test structure rotated by 45° does not show its simulated behaviour, like the other rotating arm test structures, on top of which Pt thin films were sputtered. Thus, no possible malfunction of the rotating arm test structures due to sputtering Pt on top of them is to be concluded. Further, while the rotating arm test structures with PECVD-deposited a-SiC:H thin films on top of them showed their simulated behaviour, all the analysed rotating arm test structures, onto which thin films were sputtered, did not behave according to the COMSOL simulations.

Although the 500 nm AlN thin film induced similar x-displacements as the 500 nm Pt one, the 1000 nm AlN thin film, sputtered on top of another four pairs of rotating arm test structures, arranged identically on the wafer acting as a mount, as for the sputtering of the Pt and the 500 nm AlN thin film, produced a different and unexpected result: it destroyed the smaller, straight-oriented rotating arm test structure ($L_f = 757$ μm), located at the edge of the wafer acting as a mount, as shown in Figure 4.13. Even if the rotating arm test structures are designed with a fixed beam parallel to each of the right and left display beams, the test structure was not able to withstand the compressive mechanical stress inside the 1000 nm AlN thin film, as only a downward inclined part of a left display beam (see Figure 4.13) was still visible from the whole rotating arm structure after the sputtering of the 1000 nm AlN thin film.

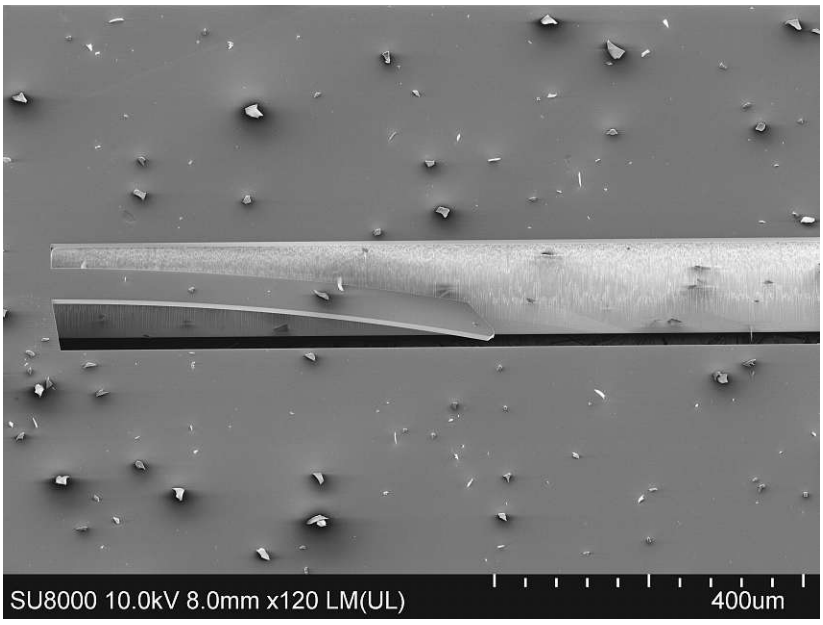

Figure 4.13: Destroyed smaller, straight-oriented rotating arm test structure ($L_f = 757$ μm), located at the edge of the wafer acting as a mount, in response to the 1000 nm AlN thin film sputtered on top of it - zoomed view.

4.3 Measurements done on evaporated thin films

In search of a thin film containing homogeneously distributed tensile stress, Cr was evaporated in the form of a 250 nm thin film on top of two straight-oriented rotating arm test structures, and on top of two rotating arm test structures rotated by 45°. Same as for the PECVD-deposited and the sputtered thin films, both the straight-oriented and the rotating arm test structures rotated by 45° were always fabricated as a pair composed of a smaller structure, with $L_f = 757$ μm, and of a larger one, with $L_f = 1013$ μm (see Figure 3.8 - 3.9). The evaporation of the 250 nm thick Cr thin film only on top of the two mentioned pairs of rotating arm test structures was expected to enable a comprehensive analysis of the response of the rotating arm test structure design. No additional pairs of rotating arm test structures, placed in different positions, were needed due to the homogeneously distributed mechanical stress. At the same time, the behaviour of the rotating arm test structures rotated by 45° could be compared to the one of the straight-oriented ones.

Next, Table 4.5 gives an overview of the measured and expected x-displacements displayed by the rotation of both display beams of the smaller and larger, straight-oriented rotating arm test structures in response to the mechanically stressed 250 nm Cr thin film.

Thin film	Test structure	right x-displ.	left x-displ.	expected x-displ.
250 nm Cr	$L_f = 757$ μm	-2.5 μm	-0.25 μm	2.6075 μm
250 nm Cr	$L_f = 1013$ μm	-4.5 μm	-0.5 μm	4.6935 μm

Table 4.5: Overview of the measured and expected x-displacements displayed by the rotation of both display beams, part of the smaller and the larger, straight-oriented rotating arm test structures, coated with the 250 nm Cr thin film. The SEM pictures corresponding to the measured x-displacements can be found in the Supplementary material part of this diploma thesis.

The same formula used for calculating the expected x-displacements for the rotating arm test structures covered with PECVD-deposited thin films (see Table 4.1) was adapted for approximating the x-displacement expected to occur for both straight-oriented rotating arm structures, coated with the 250 nm Cr thin film (see Table 4.5):

expected x-displacement = 1.043 × 0.25 × highest x-displacement registered at Point 20

Thus, these simulated x-displacements at Point 20 were multiplied with 1.043, as the evaporated Cr thin film has an average mechanical stress of 1043 MPa compared to the 600 - 700 MPa measured for the PECVD-deposited thin films, for obtaining an approximate value of the expected x-displacement. This formula used for calculating the expected x-displacements is for evaporated thin films as accurate as for the PECVD-deposited ones. Like PECVD, evaporation produces thin films with homogeneously distributed

mechanical stress, while the mechanical stress differs along sputtered thin films.
Next, a 250 nm thick Cr thin film was evaporated with the single purpose of measuring its mechanical stress on a wafer. Thus, the wafer curvature stress measurement method was applied on this wafer.

According to Table 4.5, both the smaller and the larger, straight-oriented rotating arm test structures behave identically: while both their right and left display beam rotates counterclockwise, the extent of their rotational movement is different. Thus, both the smaller and the larger, straight-oriented rotating arm test structures, covered with the 250 nm Cr thin film, do not show their simulated behaviour, like the rotating arm test structures, on top of which thin films were sputtered, and unlike the rotating arm test structures coated with PECVD-deposited thin films. Something worth mentioning is the ten times higher rotational movement of the right display beams of both rotating arm test structures from Table 4.5 when compared to the rotational movement of the left display beams of the same test structures.
Next, due to the different rotational movement of the right and left display beams of both the smaller and the larger rotating arm test structures (see Table 4.5), the ratio between the measured and the expected x-displacement of both display beams of these specific rotating arm test structures brings no value and will be therefore not further analysed. On the other side, a particularity worth mentioning is the value of around 95.9 % of the same ratio, when considering only the stress response of the right display beam of both the smaller and the larger rotating arm test structure.

Further, Table 4.6 gives an overview of the measured and expected x-displacements displayed by the rotation of both display beams of the smaller and the larger rotating arm test structures rotated by 45° in response to the mechanically stressed 250 nm Cr thin films.

Thin film	Test structure	right x-displ.	left x-displ.	expected x-displ.
250 nm Cr	$L_f = 757$ μm	-2 μm	-2 μm	2.6075 μm
250 nm Cr	$L_f = 1013$ μm	-4.5 μm	-4.5 μm	4.6935 μm

Table 4.6: Overview of the measured and expected x-displacements displayed by the rotation of both display beams, part of the smaller and the larger rotating arm test structures rotated by 45°, coated with the 250 nm Cr thin film. The SEM pictures corresponding to the measured x-displacements can be found in the Supplementary material part of this diploma thesis.

For approximating the x-displacement expected to occur for both rotating arm structures rotated by 45°, covered with the 250 nm Cr thin film (see Table 4.6), the same formula used for calculating the expected x-displacements for the straight-oriented rotating arm test structures, covered with the same 250 nm Cr thin film, was used:

expected x-displacement = 1.043 × 0.25 × highest x-displacement registered at Point 20

Unlike the pair of straight-oriented rotating arm test structures coated with the same 250 nm Cr thin film, both the smaller and the larger rotating arm test structures rotated by 45° show their simulated behaviour. According to Table 4.6, both their right and left display beam rotates counterclockwise, while the extent of their rotational movement is equal. Such a different behaviour between the rotating arm test structures rotated by 45° and the straight-oriented ones could not be detected for the rotating arm test structures covered with PECVD-deposited or sputtered thin films, where the orientation of the test structure did not trigger a different behaviour in terms of direction and extent of rotational movement of the display beams.

Next, the measured x-displacements of both display beams, part of the smaller rotating arm test structure rotated by 45°, coated with the 250 nm Cr thin film, represent around 76.7 % of the expected x-displacement. The larger rotating arm test structure rotated by 45° and coated with the same 250 nm Cr thin film appears to measure the stress better than the smaller structure, as the ratio between the measured and the expected x-displacement of both its display beams is around 95.9 %. This value represents the highest ratio registered by a rotating arm test structure defined in this diploma thesis.

Although the larger rotating arm test structure rotated by 45°, covered with the 250 nm Cr thin film, shows its simulated behaviour (according to Table 4.6), the ends of its display beams incline upwards, as depicted in Figure 4.14 - 4.15. Similar out-of-plane deflection can be observed in Figure 4.11 - 4.12 for the larger, edge 1000 nm Pt straight-oriented rotating arm test structure. As both the1000 nm thick Pt thin film and the 250 nm thick Cr thin film contain tensile mechanical stress, these observed out-of-plane deflections represent expected consequences.
The zoomed view of the out-of-plane deflection of the right display beam, part of the larger rotating arm test structure rotated by 45°, coated with the 250 nm Cr thin film (see Figure 4.15), highlights the magnitude of this structures drawback: the display beam inclines with more than its complete height upwards. While the layer of the rotating arm test structure is 15 μm thick, the Cr thin film evaporated on top of it adds an extra 0.25 μm to the height of the display beam. The result is an upwards out-of-plane deflection larger than 15.25 μm, which may further cause torsion of the display beam. Thus, an accurate reading of the x-displacements may be disturbed, as the distance between two markers of the scale used for measuring the rotation of the display beam is equal to 5 μm.

An advantage of the evaporated thin films, when compared to the PECVD-deposited ones, is given by the precision of evaporating thin films only on top of the rotating arm test structures without covering their side walls. As depicted in Figure 4.16 - 4.17, the marks of the Bosch etching are still visible on the side walls of the bottom Si layer, which hosts the rotating arm test structure, even after the evaporation of the Cr thin film on top of it.

Next, the following final chapter of this diploma thesis contains conclusions regarding the behaviour of the rotating arm test structure design, as described elaborately in the second and especially the third chapter, together with improvement inputs and further research questions.

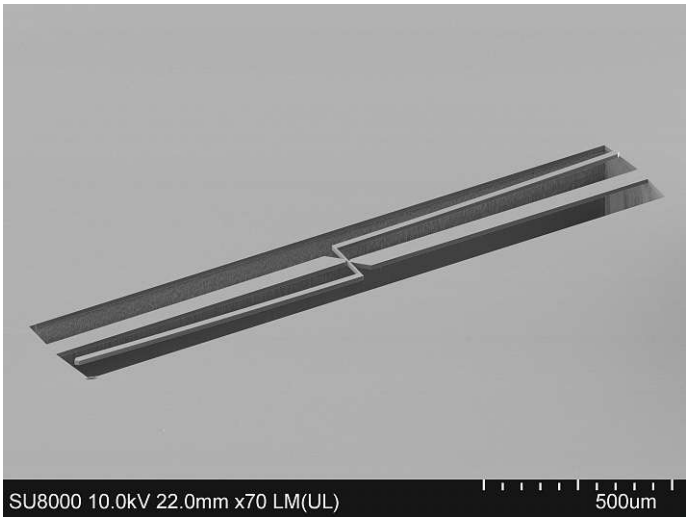

Figure 4.14: Out-of-plane deflection observable for both display beams, part of the larger rotating arm test structure ($L_f = 1013$ μm) rotated by 45°, in response to the 250 nm Cr thin film evaporated on top of it - top view.

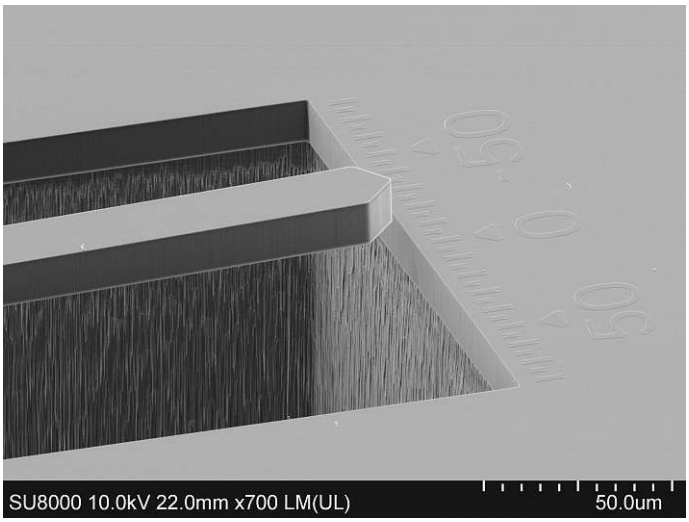

Figure 4.15: Out-of-plane deflection observable for the right display beam, part of the larger rotating arm test structure ($L_f = 1013$ μm) rotated by 45°, in response to the 250 nm Cr thin film evaporated on top of it - zoomed view.

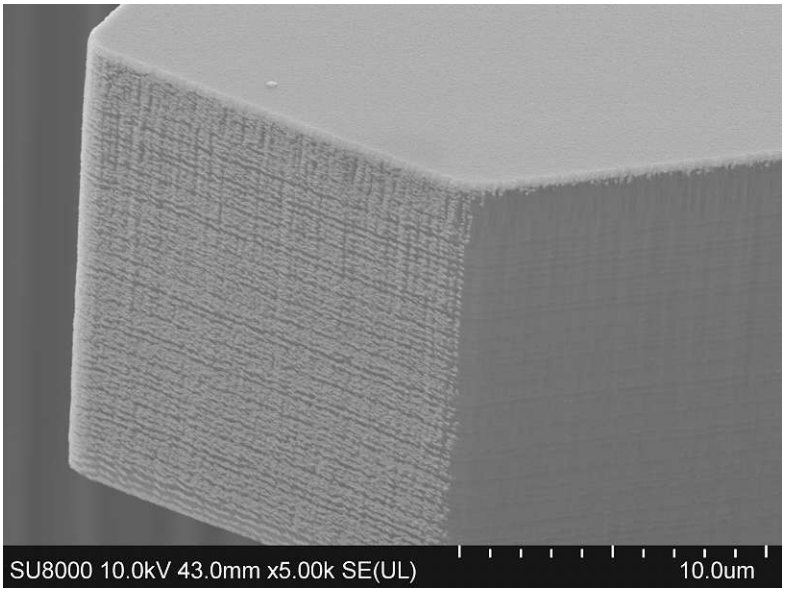

Figure 4.16: Overview of the surface of both Cr (top) and Si (bottom) layers, observable for the left display beam, part of the larger rotating arm test structure ($L_f = 1013$ μm) rotated by 45° - side view.

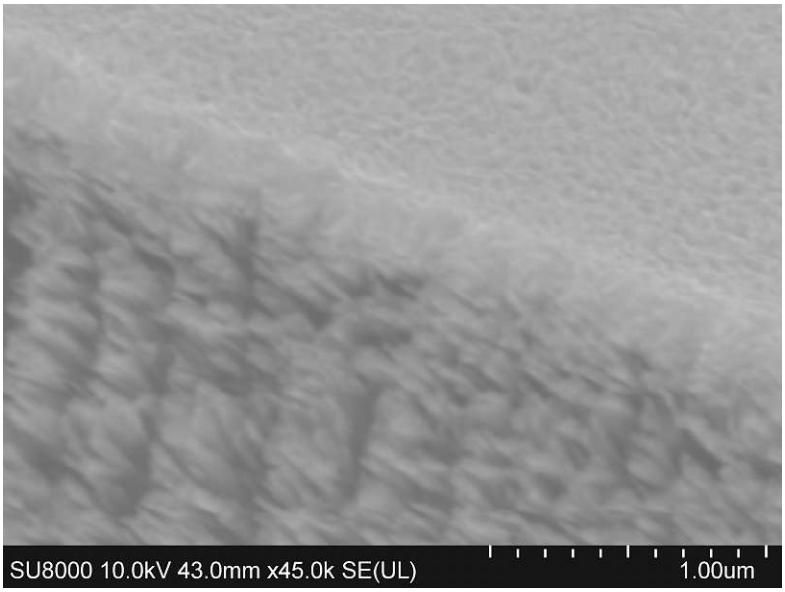

Figure 4.17: Overview of the surface of both Cr (top) and Si (bottom) layers, observable for the left display beam, part of the larger rotating arm test structure ($L_f = 1013$ μm) rotated by 45° - zoomed view.

CHAPTER 5

Conclusion and outlook

To give a clear overview of the effects produced by the thin films deposited on top of the rotating arm test structures, Table 5.1 introduces the ratio between the measured and the expected x-displacement of the display beams of each analysed rotating arm test structure as a performance criterion of the rotating arm test structures behaviour.

In the case of the rotating arm test structures coated with PECVD-deposited a-SiC:H thin films, both larger test structures, which had the rotational movement of both their left and right display beam analysed, proved that they function correctly. However, an around 40 % larger x-displacement was expected (see Table 4.1). Thus, their ratio between measured and expected x-displacement is lower than the one of other display beams part of other rotating arm test structures listed in Table 5.1. The orientation of the rotating arm test structures does not affect their functionality, as the ratios of the larger rotating arm test structures covered with the same 375 nm a-SiC:H thin film differ by only 3 %, even though one of the rotating arm test structures is straight-oriented, while the other one is rotated by 45°.
Next, none of the rotating arm test structures coated with sputtered Pt and AlN thin films can function correctly. Further, the larger rotating arm test structure covered with AlN implies that not the specific use of Pt, but rather the use of sputtering as the deposition process hinders a correct response of the rotating arm test structures.
The rotating arm test structures coated with evaporated Cr behave differently with respect to their orientation: while the straight-oriented rotating arm test structures do not show their expected behaviour, the ones rotated by 45° function correctly. Further, the larger rotating arm test structure rotated by 45° achieves the best performance along the rotating arm test structures presented in this diploma thesis due to its 95.9 % ratio between the measured and expected x-displacement. However, its upward out-of-plane deflection caused by the tensile stress in the Cr thin film is worth mentioning (see Figure 4.15). Similar upwards out-of-plane deflection is also caused by the tensile stressed Pt

thin films, as depicted in Figure 4.12, while the compressive stress present in a-SiC:H thin films (see Figure 4.10) and AlN thin films (see Figure 4.13) causes a downwards out-of-plane deflection.

Test struct.	Orientation	Thin film	Ev. d. b.	Ident. rot.	$\frac{measured}{expected}$
$L_f = 757\ \mu m$	straight	250 nm a-SiC:H	right	unknown	61.5 %
$L_f = 757\ \mu m$	straight	375 nm a-SiC:H	right	unknown	61.5 %
$L_f = 1013\ \mu m$	straight	250 nm a-SiC:H	right	unknown	85.5 %
$L_f = 1013\ \mu m$	straight	375 nm a-SiC:H	both	yes	57 %
$L_f = 1013\ \mu m$	rot. by 45°	375 nm a-SiC:H	both	yes	60 %
$L_f = 1013\ \mu m$	straight	500 nm Pt	both	no	76.9 % (left)
$L_f = 1013\ \mu m$	straight	1000 nm Pt	both	no	94 % (left)
$L_f = 757\ \mu m$	straight	1000 nm Pt	both	no	76.9 % (left)
$L_f = 1013\ \mu m$	rot. by 45°	1000 nm Pt	both	no	25.6 % (left)
$L_f = 1013\ \mu m$	rot. by 45°	500 nm AlN	both	no	68.4 % (right)
$L_f = 757\ \mu m$	straight	250 nm Cr	both	no	95.9 % (right)
$L_f = 1013\ \mu m$	straight	250 nm Cr	both	no	95.9 % (right)
$L_f = 757\ \mu m$	rot. by 45°	250 nm Cr	both	yes	76.7 %
$L_f = 1013\ \mu m$	rot. by 45°	250 nm Cr	both	yes	95.9 %

Table 5.1: Overview of the verification measurements results of the smaller (see Figure 3.11) and of the larger rotating arm test structure (see Figure 3.12). The column *Ev. d. b.* (shortened from Evaluated display beam) states which display beams of the evaluated rotating arm test structure were analysed with SEM. The column *Ident. rot.* (shortened from Identical rotational movement of the right and left display beams) informs if the extent and the direction of the rotational movement of both right and left display beam of the same rotating arm test structure is identical. The column *measured/expected* contains the ratio between the measured and the expected x-displacement of the analysed display beam. If the rotational movement of the display beams is identical in its extent and direction, then this ratio is the same for both display beams. Otherwise, only the larger value will be documented in this table, while the *(left)* or *(right)* comment after the percentage value states which of the display beams of the analysed rotating arm test structure registered this better result. The measured and expected x-displacement values used for calculating the ratio were taken from Table 4.1 for the rotating arm test structures coated with PECVD-deposited a-SiC:H thin films, from Table 4.3 - 4.4 for the rotating arm test structures coated with sputtered Pt and AlN thin films, and from Table 4.5 - 4.6 for the rotating arm test structures coated with evaporated Cr thin films. The straight-oriented rotating arm test structures coated with sputtered 500 nm and 1000 nm Pt thin films were located at the edge of the wafer acting as a mount.

The first improvement measure, which could be implemented without making any design changes on the fabricated rotating arm test structure, as presented in this diploma thesis and depicted in Figure 3.11 - 3.12, would be the deposition of the stressed thin films only on the two fixed parallel beams of the rotating arm test structures. In this way the out-of-plane deflection of the display beams could be avoided, and the chances of destroying the display beams during the deposition process of the thin films could be reduced. A drawback of this selective deposition of the stressed thin film is that an extra mask would be required for fabricating such a rotating arm test structure.
Another improvement measure, which could also be applied without making any design changes on the fabricated rotating arm test structure, would be to pattern the test structures only at the end of the fabrication process, after the deposition of the stressed thin film. In this way, the accidental thin film deposition on the side walls of the rotating arm test structure, which is considerable for PECVD and sputtering, could be avoided. A drawback caused by letting the patterning at the end of the fabrication process is the need for an extra etching step. Alternatively, the choice of the deposition method could be restricted to evaporation, which does not affect the surface of the side walls (see Figure 4.17).

The first change in the design of the fabricated rotating arm test structure (see Figure 3.6) would be to modify the narrow part of the fixed beams, which connects them with the central part of the rotating indicator beam. To implement changes of this narrow part as described in [4] may be subject to further research questions.
Another perspective for further research would be to increase the width of the central part of the rotating indicator beam W_{rc} (see Figure 3.6) to make it equal to the width of the fixed beams W_f (see Figure 3.3), while reducing the width of the fixed beams at their joint with the central part of the rotating indicator beam W_{fc} (see Figure 3.6). These changes could ensure higher robustness of the central part of the rotating arm test structure while making it more resistant to unwanted effects of mechanical stress, like torsion.
A final change possible subject to further research is the reduction of the base layer thickness (see Figure 2.3) in order to make the entire rotating arm test structure thinner. The result may be a higher x-displacement of the display beams, as they would become more responsive. However, a too-thin rotating arm test structure may become unstable and more prone to out-of-plane deflections than the design presented in this diploma thesis.

Supplementary material

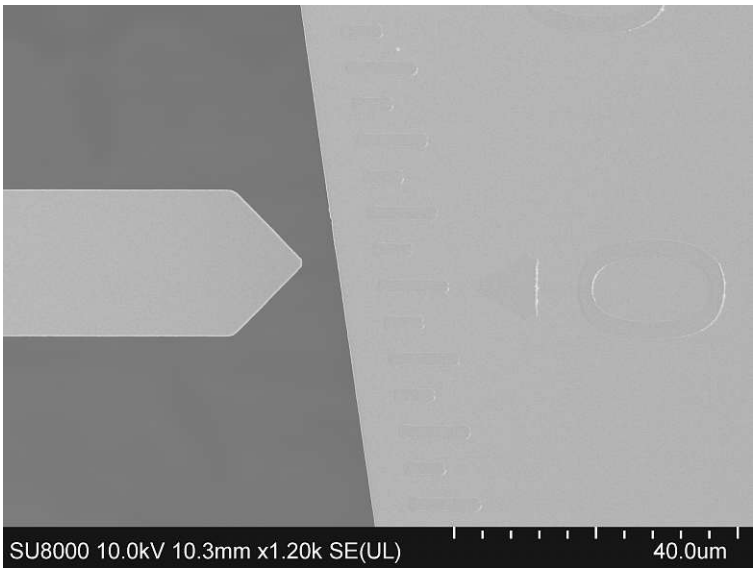

Figure 1: Rotation of the right display beam, part of the larger, straight-oriented rotating arm test structure ($L_f = 1013$ μm), located at the edge of the wafer acting as a mount, in response to the 500 nm Pt thin film sputtered on top of it - zoomed view. The distance between two markers of the scale used for measuring the rotation of the display beam is equal to 5 μm.

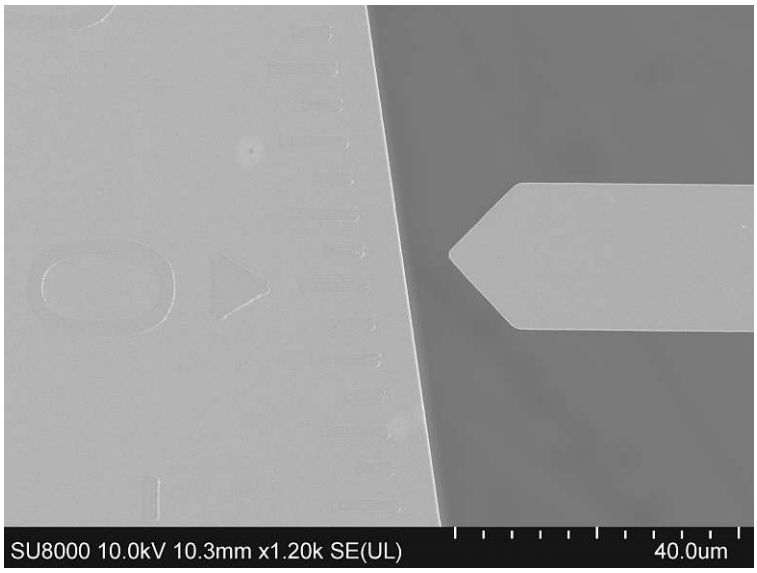

Figure 2: Rotation of the left (opposite) display beam, part of the larger, straight-oriented rotating arm test structure ($L_f = 1013$ μm), located at the edge of the wafer acting as a mount, in response to the 500 nm Pt thin film sputtered on top of it - zoomed view. The distance between two markers of the scale used for measuring the rotation of the display beam is equal to 5 μm.

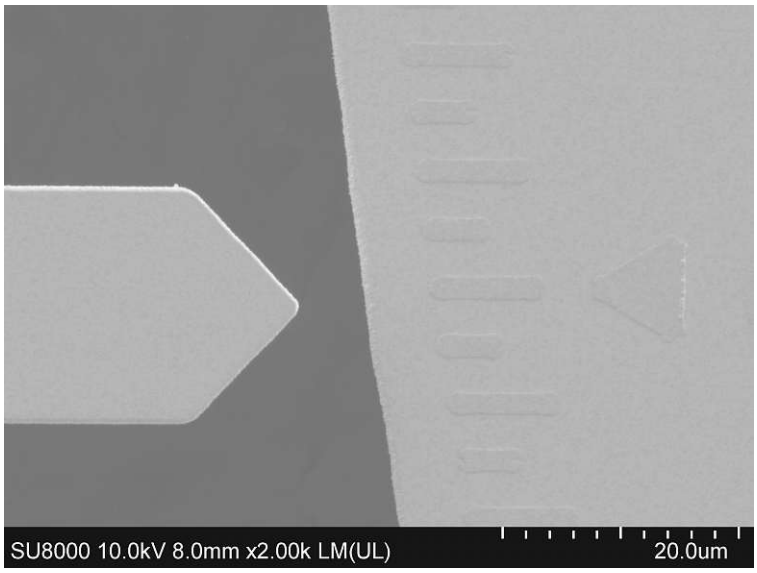

Figure 3: Rotation of the right display beam, part of the smaller, straight-oriented rotating arm test structure ($L_f = 757$ μm), located at the edge of the wafer acting as a mount, in response to the 1000 nm Pt thin film sputtered on top of it - zoomed view. The distance between two markers of the scale used for measuring the rotation of the display beam is equal to 5 μm.

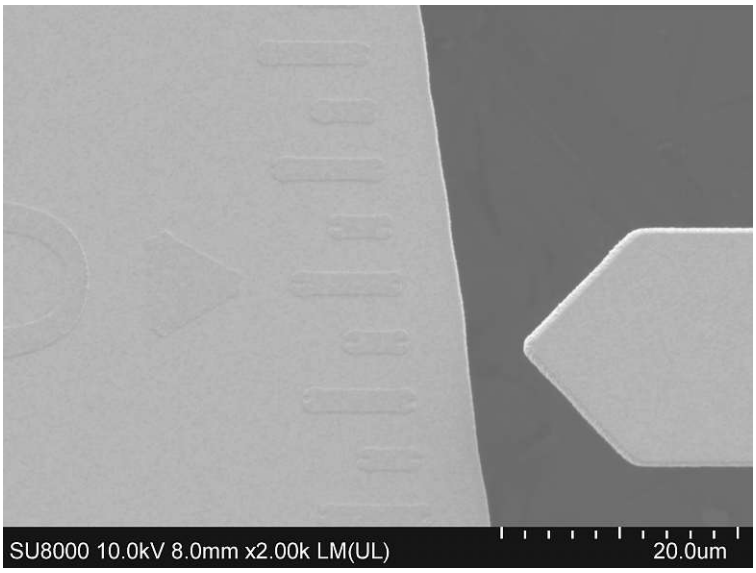

Figure 4: Rotation of the left (opposite) display beam, part of the smaller, straight-oriented rotating arm test structure ($L_f = 757$ μm), located at the edge of the wafer acting as a mount, in response to the 1000 nm Pt thin film sputtered on top of it - zoomed view. The distance between two markers of the scale used for measuring the rotation of the display beam is equal to 5 μm.

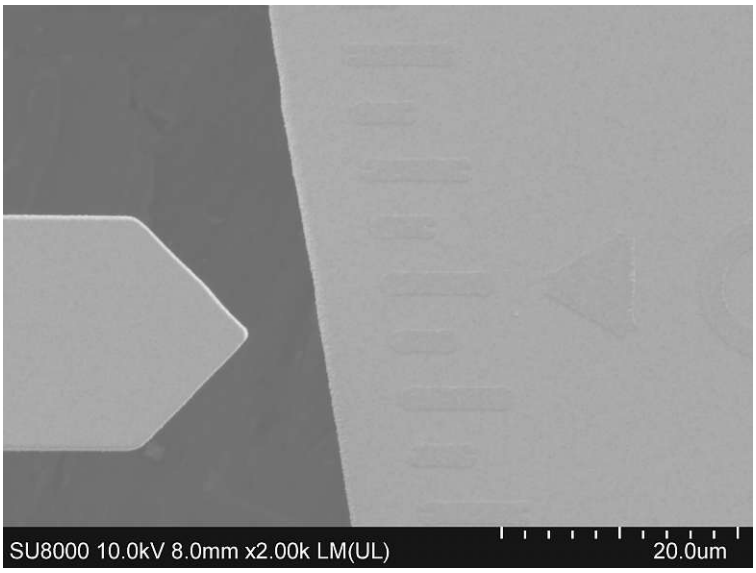

Figure 5: Rotation of the right display beam, part of the larger, straight-oriented rotating arm test structure ($L_f = 1013$ μm), located at the edge of the wafer acting as a mount, in response to the 1000 nm Pt thin film sputtered on top of it - zoomed view. The distance between two markers of the scale used for measuring the rotation of the display beam is equal to 5 μm.

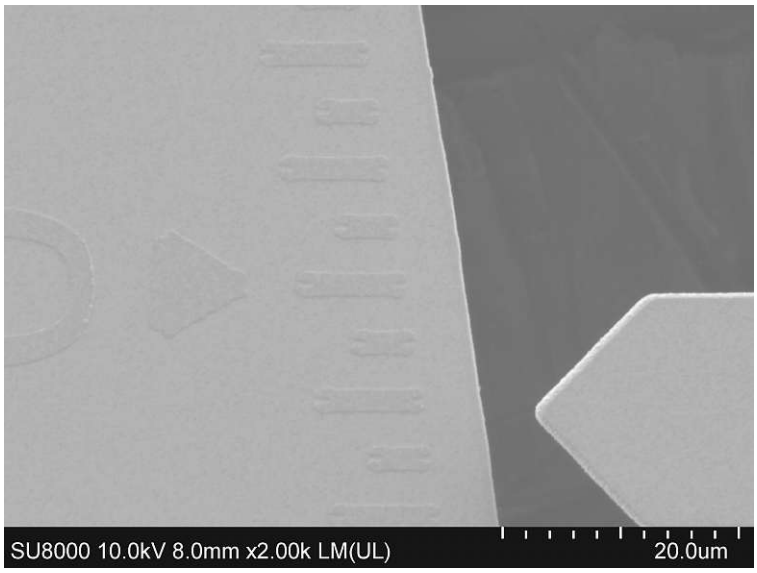

Figure 6: Rotation of the left (opposite) display beam, part of the larger, straight-oriented rotating arm test structure (L_f = 1013 μm), located at the edge of the wafer acting as a mount, in response to the 1000 nm Pt thin film sputtered on top of it - zoomed view. The distance between two markers of the scale used for measuring the rotation of the display beam is equal to 5 μm.

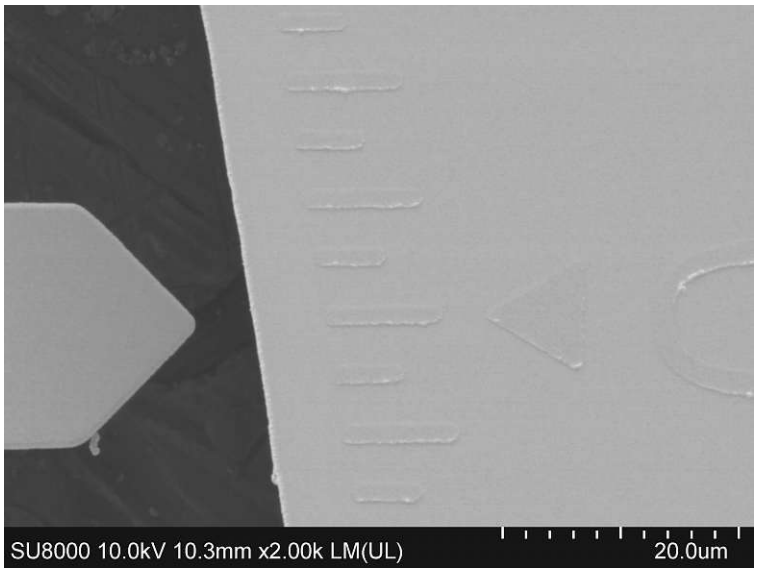

Figure 7: Rotation of the right display beam, part of the larger rotating arm test structure (L_f = 1013 μm) rotated by 45°, located centrally on the wafer acting as a mount, in response to the 1000 nm Pt thin film sputtered on top of it - zoomed view. The distance between two markers of the scale used for measuring the rotation of the display beam is equal to 5 μm.

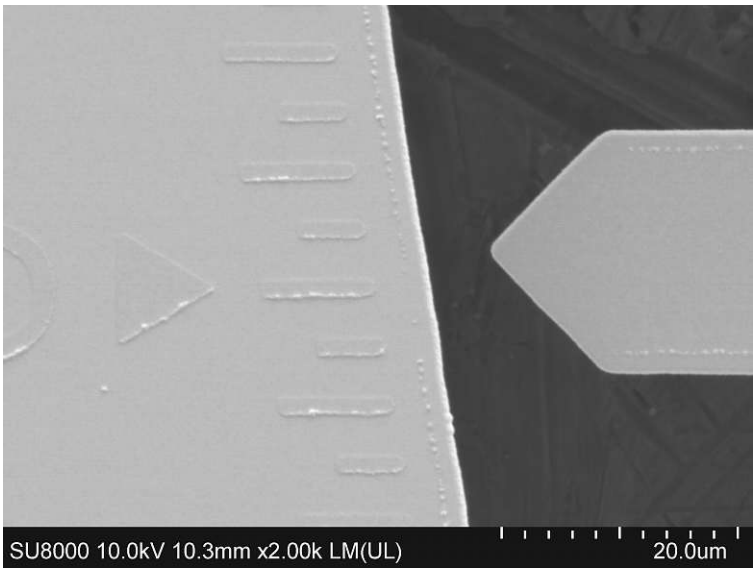

Figure 8: Rotation of the left (opposite) display beam, part of the larger rotating arm test structure (L_f = 1013 μm) rotated by 45°, located centrally on the wafer acting as a mount, in response to the 1000 nm Pt thin film sputtered on top of it - zoomed view. The distance between two markers of the scale used for measuring the rotation of the display beam is equal to 5 μm.

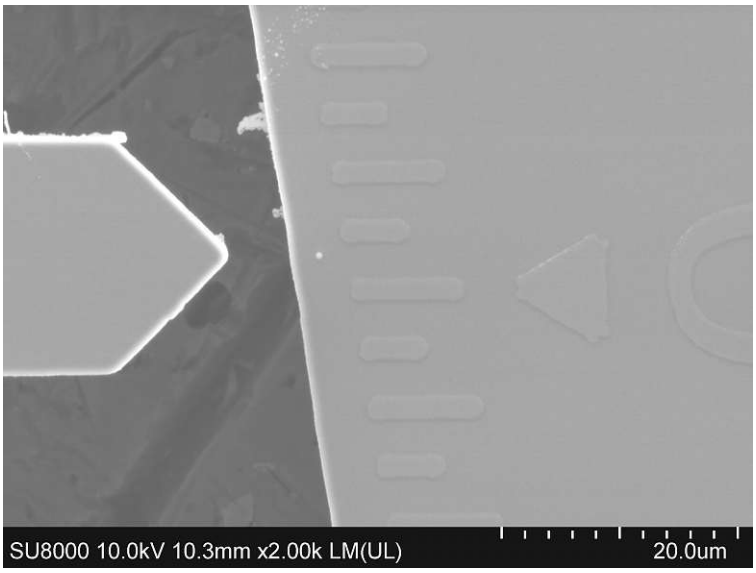

Figure 9: Rotation of the right display beam, part of the larger rotating arm test structure (L_f = 1013 μm) rotated by 45°, located centrally on the wafer acting as a mount, in response to the 500 nm AlN thin film sputtered on top of it - zoomed view. The distance between two markers of the scale used for measuring the rotation of the display beam is equal to 5 μm.

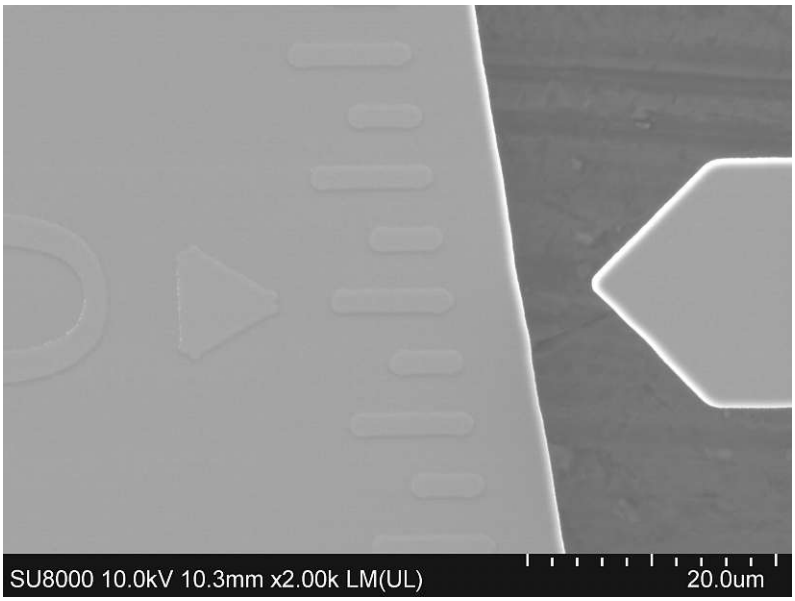

Figure 10: Rotation of the left (opposite) display beam, part of the larger rotating arm test structure ($L_f = 1013$ μm) rotated by 45°, located centrally on the wafer acting as a mount, in response to the 500 nm AlN thin film sputtered on top of it - zoomed view. The distance between two markers of the scale used for measuring the rotation of the display beam is equal to 5 μm.

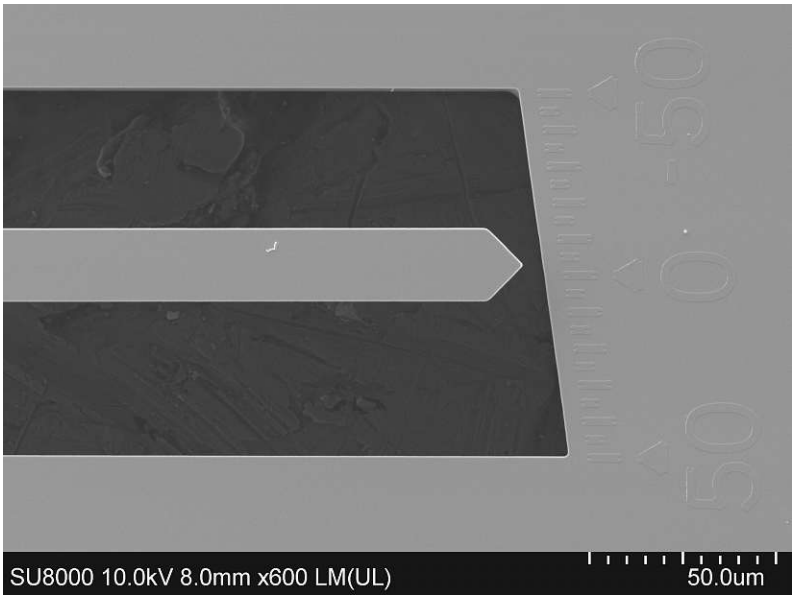

Figure 11: Rotation of the right display beam, part of the smaller, straight-oriented rotating arm test structure ($L_f = 757$ μm), in response to the 250 nm Cr thin film evaporated on top of it. The values of the scale are expressed in μm.

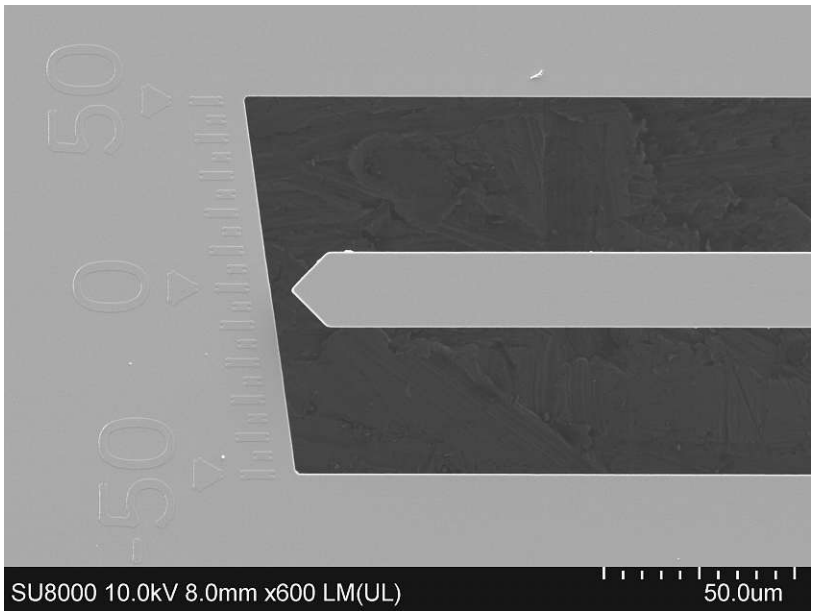

Figure 12: Rotation of the left (opposite) display beam, part of the smaller, straight-oriented rotating arm test structure ($L_f = 757$ μm), in response to the 250 nm Cr thin film evaporated on top of it. The values of the scale are expressed in μm.

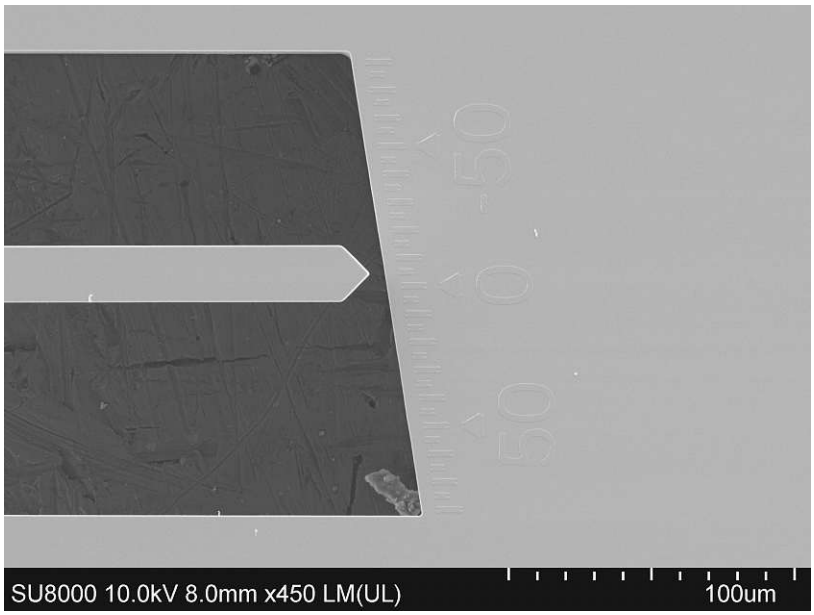

Figure 13: Rotation of the right display beam, part of the larger, straight-oriented rotating arm test structure ($L_f = 1013$ μm), in response to the 250 nm Cr thin film evaporated on top of it. The values of the scale are expressed in μm.

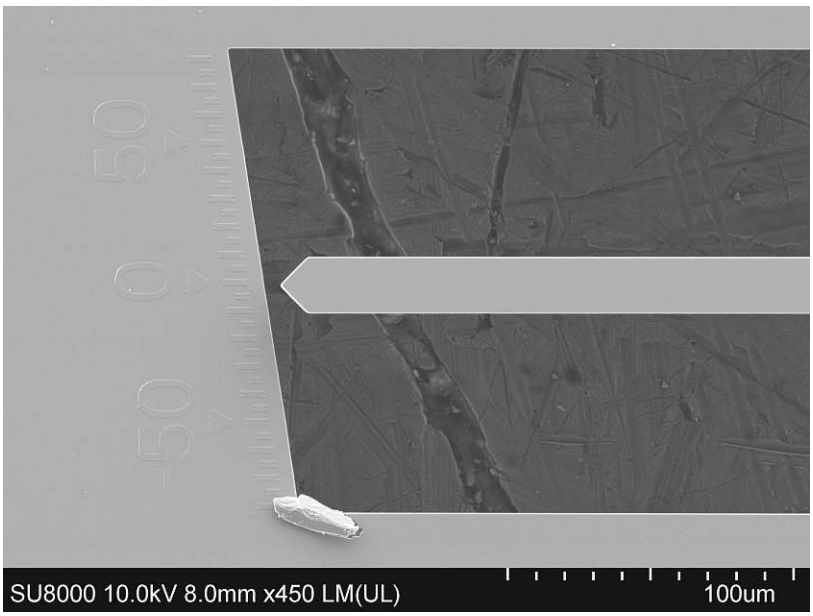

Figure 14: Rotation of the left (opposite) display beam, part of the larger, straight-oriented rotating arm test structure ($L_f = 1013$ μm), in response to the 250 nm Cr thin film evaporated on top of it. The values of the scale are expressed in μm.

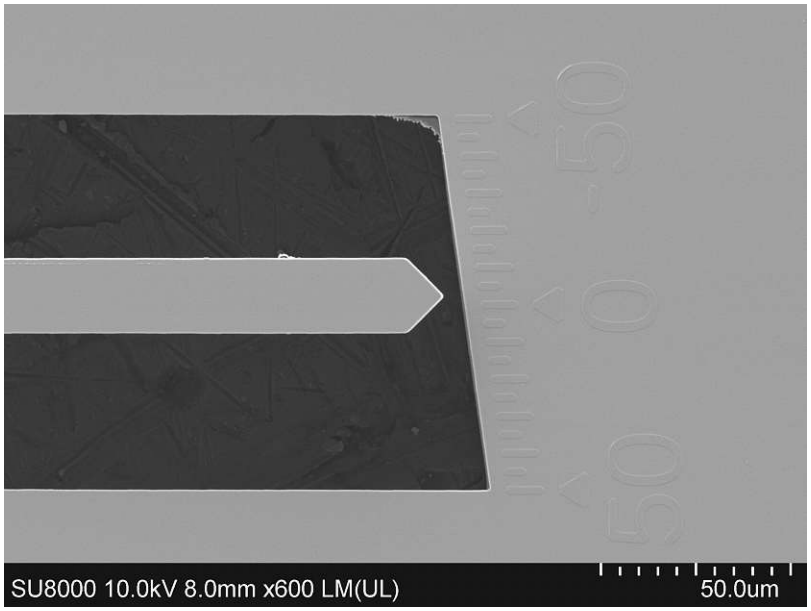

Figure 15: Rotation of the right display beam, part of the smaller rotating arm test structure ($L_f = 757$ μm) rotated by 45°, in response to the 250 nm Cr thin film evaporated on top of it. The values of the scale are expressed in μm.

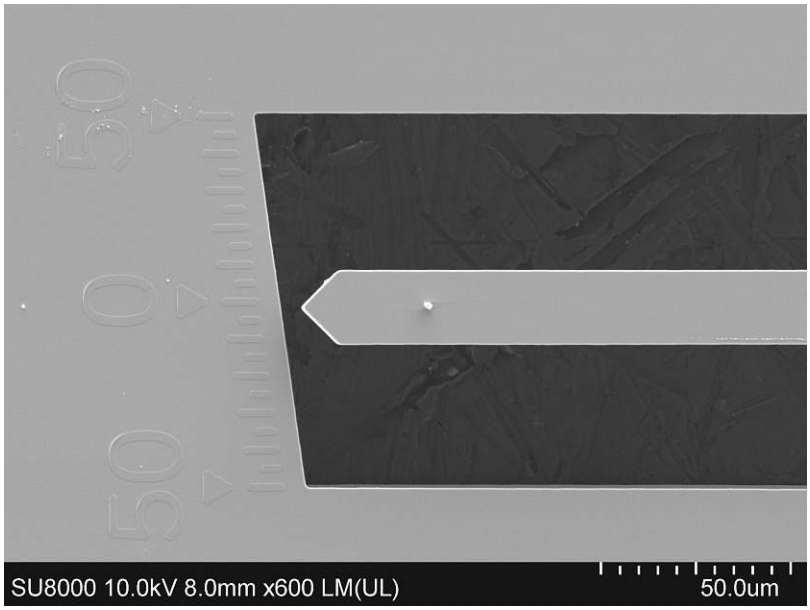

Figure 16: Rotation of the left (opposite) display beam, part of the smaller rotating arm test structure ($L_f = 757$ μm) rotated by 45°, in response to the 250 nm Cr thin film evaporated on top of it. The values of the scale are expressed in μm.

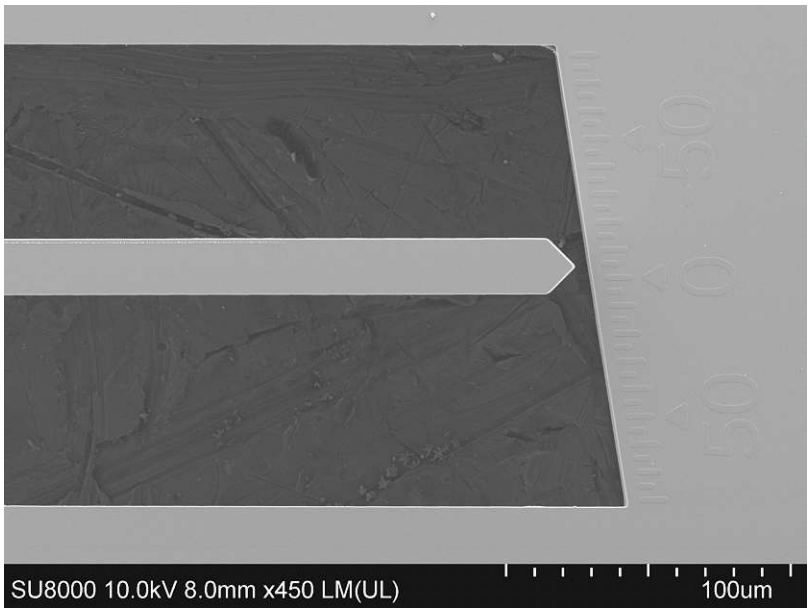

Figure 17: Rotation of the right display beam, part of the larger rotating arm test structure ($L_f = 1013$ μm) rotated by 45°, in response to the 250 nm Cr thin film evaporated on top of it. The values of the scale are expressed in μm.

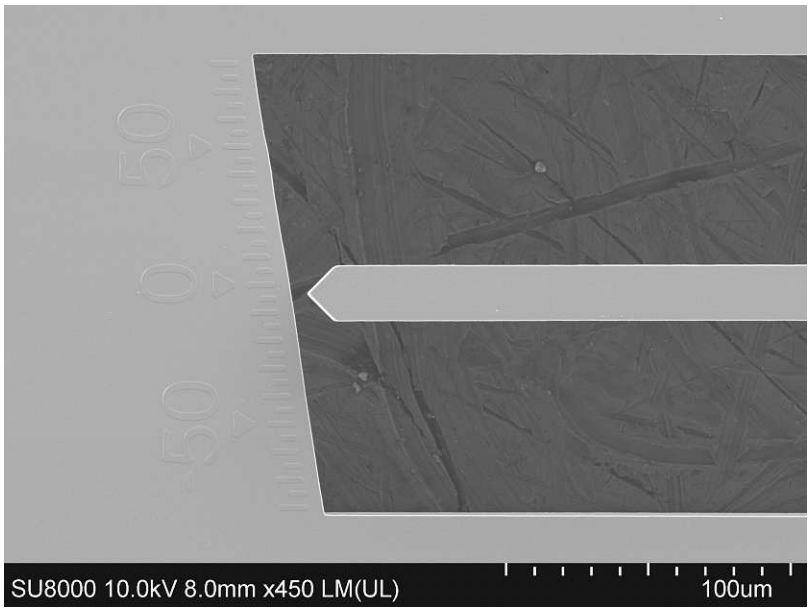

Figure 18: Rotation of the left (opposite) display beam, part of the larger rotating arm test structure ($L_f = 1013$ μm) rotated by 45°, in response to the 250 nm Cr thin film evaporated on top of it. The values of the scale are expressed in μm.

Bibliography

[1] K.-S. Chen and K.-S. Ou, "Mems residual stress characterization: Methodology and perspective," in *Handbook of Silicon Based MEMS Materials and Technologies*, pp. 787–801, Elsevier, 2020.

[2] S. Dutta and A. Pandey, "Overview of residual stress in mems structures: Its origin, measurement, and control," *Journal of Materials Science: Materials in Electronics*, vol. 32, no. 6, pp. 6705–6741, 2021.

[3] E. Chason and P. R. Guduru, "Tutorial: Understanding residual stress in polycrystalline thin films through real-time measurements and physical models," *Journal of Applied Physics*, vol. 119, no. 19, p. 191101, 2016.

[4] P. A. Sohi, I. Stateikina, and M. Kahrizi, "Thin films residual stress profile evaluation using test microstructures: Illustrated on an example of aln film," *Journal of Vacuum Science & Technology B, Nanotechnology and Microelectronics: Materials, Processing, Measurement, and Phenomena*, vol. 39, no. 3, p. 033001, 2021.

[5] R. Schöngrundner, R. Treml, T. Antretter, D. Kozic, W. Ecker, D. Kiener, and R. Brunner, "Critical assessment of the determination of residual stress profiles in thin films by means of the ion beam layer removal method," *Thin Solid Films*, vol. 564, pp. 321–330, 2014.

[6] H. Guckel, D. Burns, C. Rutigliano, E. Lovell, and B. Choi, "Diagnostic microstructures for the measurement of intrinsic strain in thin films," *Journal of Micromechanics and Microengineering*, vol. 2, no. 2, p. 86, 1992.

[7] J. R. Godin, S. H. P. Won, P. M. Nieva, L. N. Phong, and T. Pope, "Residual stress dependency on wafer location of thin film pecvd silicon nitride," in *Nanotechnology 2011: Advanced Materials, CNTs, Particles, Films and Composites-2011 NSTI Nanotechnology Conference and Expo, NSTI-Nanotech 2011*, pp. 108–111, 2011.

[8] G. Abadias, E. Chason, J. Keckes, M. Sebastiani, G. B. Thompson, E. Barthel, G. L. Doll, C. E. Murray, C. H. Stoessel, and L. Martinu, "Stress in thin films and coatings: Current status, challenges, and prospects," *Journal of Vacuum Science & Technology A: Vacuum, Surfaces, and Films*, vol. 36, no. 2, p. 020801, 2018.

[9] L. Elbrecht, U. Storm, R. Catanescu, and J. Binder, "Comparison of stress measurement techniques in surface micromachining," *Journal of Micromechanics and Microengineering*, vol. 7, no. 3, p. 151, 1997.

[10] A. Sharma, M. Kaur, D. Bansal, D. Kumar, and K. Rangra, "Review of mems test structures for mechanical parameter extraction," *Journal of Nano-and Electronic Physics*, vol. 3, no. 1, p. 243, 2011.

[11] Z. Zhao, J. Hershberger, S. Yalisove, and J. Bilello, "Determination of residual stress in thin films: a comparative study of x-ray topography versus laser curvature method," *Thin Solid Films*, vol. 415, no. 1-2, pp. 21–31, 2002.

[12] C.-H. Hsueh, S. Schmauder, C.-S. Chen, K. K. Chawla, N. Chawla, W. Chen, Y. Kagawa, *et al.*, *Handbook of mechanics of materials*. Springer, 2019.

[13] L. Koutsokeras and G. Abadias, "Intrinsic stress in zrn thin films: Evaluation of grain boundary contribution from in situ wafer curvature and ex situ x-ray diffraction techniques," *Journal of Applied Physics*, vol. 111, no. 9, p. 093509, 2012.

[14] G. Jiang, F. Haiyang, P. Bo, and K. Renke, "Recent progress of residual stress measurement methods: A review," *Chinese Journal of Aeronautics*, vol. 34, no. 2, pp. 54–78, 2021.

[15] G. Schiavone, J. Murray, S. Smith, M. P. Y. Desmulliez, A. R. Mount, and A. J. Walton, "A wafer mapping technique for residual stress in surface micromachined films," *Journal of Micromechanics and Microengineering*, vol. 26, no. 9, p. 095013, 2016.

[16] A. Sharma, D. Bansal, M. Kaur, P. Kumar, D. Kumar, R. Sharma, and K. Rangra, "Fabrication and analysis of mems test structures for residual stress measurement," *Sensors & Transducers*, vol. 13, pp. 21–30, 2011.

[17] C. S. Pan and W. Hsu, "A microstructure for in situ determination of residual strain," *Journal of microelectromechanical systems*, vol. 8, no. 2, pp. 200–207, 1999.

[18] L. Lin, A. P. Pisano, and R. T. Howe, "A micro strain gauge with mechanical amplifier," *Journal of Microelectromechanical Systems*, vol. 6, no. 4, pp. 313–321, 1997.

[19] X. Zhang, T.-Y. Zhang, and Y. Zohar, "Measurements of residual stresses in thin films using micro-rotating-structures," *Thin Solid Films*, vol. 335, no. 1-2, pp. 97–105, 1998.

[20] T. Frischmuth, M. Schneider, D. Maurer, T. Grille, and U. Schmid, "Inductively-coupled plasma-enhanced chemical vapour deposition of hydrogenated amorphous silicon carbide thin films for mems," *Sensors and Actuators A: Physical*, vol. 247, pp. 647–655, 2016.